DISSERTATIONES
CHIMICAE
UNIVERSITATIS
TARTUENSIS
245

RAEGAN DANIELLE CHAMBERS

Electrocatalysis of oxygen reduction on Pt nanoparticles deposited on novel support materials

DISSERTATIONES CHIMICAE UNIVERSITATIS TARTUENSIS
245

DISSERTATIONES CHIMICAE UNIVERSITATIS TARTUENSIS
245

RAEGAN DANIELLE CHAMBERS

Electrocatalysis of oxygen reduction on Pt nanoparticles deposited on novel support materials

UNIVERSITY OF TARTU
Press
1632

Institute of Chemistry, Faculty of Science and Technology, University of Tartu, Estonia

Dissertation is accepted for the commencement of the degree of *Doctor Philosophiae* in Chemistry on the of June 9th, 2026 by the Council of the Institute of Chemistry, Faculty of Science and Technology, University of Tartu.

Supervisors: Dr. Heiki Erikson
Institute of Chemistry, University of Tartu, Estonia

Prof. Kaido Tammeveski
Institute of Chemistry, University of Tartu, Estonia

Opponent: Prof. Rakel Wreland Lindström
Department of Chemical Engineering, KTH-Royal Institute of Technology, Sweden

Commencement: August 28th, 2026 at 10.15, Auditorium 1021, Ravila 14a (Chemicum), Tartu, Estonia.

ISSN 1406-0299 (print) ISSN 2806-2159 (pdf)
ISBN 978-9908-57-271-0 (print) ISBN 978-9908-57-272-7 (pdf)

University of Tartu Press
www.tyk.ee

“I cry a lot, but I am so productive, it’s an art”

Taylor Swift (2024) *I Can Do It With a Broken Heart*

TABLE OF CONTENTS

1. LIST OF ORIGINAL PUBLICATIONS

This dissertation is based on the following original publications, which will be referred to as the corresponding Roman numbers (I–IV) in the text.

I **Chambers, R.;** Hussain, S.; Kozlova, J.; Kukli, K.; Ritslaid, P.; Kikas, A.; Kisand, V.; Erikson, H.; Tammeveski, K. Pt Nanoparticles Electrochemically Deposited onto Heteroatom-Doped Graphene Supports as Electrocatalysts for ORR in Acid Media. J. Electrochem. Soc. 2024, 171 (9), 096506. https://doi.org/10.1149/1945-7111/ad7296.

II **Chambers, R**.; Piirsoo, H.-M.; Tamm, A.; Kozlova, J.; Kukli, K.; Ritslaid, P.; Treshchalov, A.; Erikson, H.; Tammeveski, K. Heteroatom-Doped Graphene-Supported Pt Nanoparticles as Electrocatalysts for Proton Exchange Membrane Fuel Cells. ACS Appl. Nano Mater. 2024, 7, 5943–5955. https://doi.org/10.1021/acsanm.3c05713.

III **Chambers, R.**; Kisand, K.; Lilloja-Lensment, J.: Tarre, A.; Kozlova, J.; Aruväli, J.; Käärik, M.; Leis, J.; Kukli, K.; Kikas, A.; Kisand, V.; Erikson, H.; Tammeveski, K. Platinum Nanoparticles Supported on Nitrogen-Doped Porous Carbon for Proton Exchange Membrane Fuel Cells, *Manuscript in preparation.*

IV **Chambers, R**.; Tarre, A.; Otsus, M.; Kozlova, J.; Kukli, K.; Kikas, A.; Kisand, V.; Erikson, H.; Tammeveski, K. Platinum Nanoparticles Supported on Atomic Layer Deposited SnO_2 Decorated Multiwalled Carbon Nanotubes as the Electrocatalyst for the Oxygen Reduction Reaction. Catalysts 2025, 15 (11), 1052. https://doi.org/10.3390/catal15111052.

Author's contribution

Paper I: The author performed all electrochemical measurements, analyzed and visualized the data, and is mainly responsible for writing the paper.

Paper II: The author performed all electrochemical measurements, analyzed and visualized the data, and is mainly responsible for writing the paper.

Paper III: The author synthesized the carbon, performed all electrochemical measurements, analyzed and visualized the data, and is primarily responsible for writing the paper.

Paper IV: The author performed all electrochemical measurements, analyzed and visualized the data, and is mainly responsible for writing the paper.

2. ABBREVIATIONS AND SYMBOLS

ADT	accelerated durability testing
ALD	atomic layer deposition
BET	Brunauer-Emmett-Teller
C^b_{O2}	O_2 concentration in the bulk solution
CNT	carbon nanotube
CV	cyclic voltammetry
D_{O2}	O_2 diffusion coefficient
E^o	standard potential
ECSA	electrochemically active surface area
EDLC	electrochemical double-layer capacitance
EDS	energy-dispersive X-ray spectroscopy
EG	ethylene glycol
F	Faraday's constant
GC	glassy carbon
GDL	gas diffusion layer
GPES	General Purpose Electrochemical System
I/C	ionomer to catalyst ratio
i_k	kinetic current at a specific potential
j	measured current density
j_d	diffusion-limited current density
j_k	kinetic current density
k	ORR rate constant
K-L	Koutecký–Levich
MA	mass activity
MEA	membrane-electrode assembly
(MeCp)$PtMe_3$	trimethyl(methylcyclopentadienyl)platinum(IV)
MWCNT	multiwalled carbon nanotube
n	electron transfer number
NC	nitrogen-doped carbon
OCV	open circuit voltage
ORR	oxygen reduction reaction
PEMFC	proton exchange membrane fuel cell
P_{max}	maximum power density
PtNP	platinum nanoparticle
Pt(acac)	platinum(II) acetylacetonate
QSDFT	quenched solid density functional theory
RDE	rotating disk electrode
RHE	reversible hydrogen electrode
S_{BET}	specific surface area
SA	specific activity
SCE	saturated calomel electrode
SEM	scanning electron microscope

SMSI	strong metal-support interaction
SSA	specific surface area
SSA_{meso}	mesoporous specific surface area
SSA_{μ}	microporous specific surface area
STEM	scanning transmission electron microscopy
TDMASn	tetrakis(dimethylamido)tin(IV)
THF	tetrahydrofuran
v	scan rate
V_{tot}	total pore volume
VC	Vulcan carbon
XPS	X-ray photoelectron spectroscopy
XRD	X-ray diffraction
XRF	X-ray fluorescence
ν	kinematic viscosity of the electrolyte solution
ω	electrode rotation rate

3. INTRODUCTION

The rise and continuous use of fossil fuels over the past century has led to an increase in the rate and intensity of climate change related natural disasters, as fossil fuels release greenhouse gases that harm the environment. One technology developed to combat this is proton exchange membrane fuel cells (PEMFCs). The only byproduct associated with PEMFCs is water. PEMFCs have been developed for use in a variety of applications. They are of particular interest in the transportation sector due to their use in both light- and heavy-duty vehicles. PEMFCs are currently on the market but remain expensive.

Pt is expensive due to its rarity and difficult extraction process. However, Pt is required to catalyze the oxygen reduction reaction (ORR) at the cathode, which has sluggish reaction rate. When platinum nanoparticles (PtNPs) are attached to carbon supports, the supports degrade due to the start-up and shutdown potentials that develop across the catalyst layer. These overpotentials lead to PtNP agglomeration and carbon corrosion, which, over time, will ruin the fuel cell. One way to reduce degradation and improve the catalyst's electrocatalytic activity is to functionalize the carbon support. This can be achieved by introducing heteroatom dopants into the system or by adding metal oxides to the support. Both of which have been proven to improve the lifetime and activity of the fuel cell.

The main objectives of this research were to examine the effects that the functionalization of the carbon support has on the overall electrocatalytic activity of PtNPs for ORR. In the first part of this work, different commercially available heteroatom-doped graphenes were used as catalyst support for electrochemically deposited PtNPs. The effects of the dopants on the PtNPs were then systematically examined [I]. In the second part, the effects of the commercially available supports were further examined when the PtNPs were chemically deposited onto them [II]. In the third part of this thesis, PtNPs were chemically deposited on nitrogen-doped porous carbon. Single-cell fuel cell tests were conducted [III]. In the final part of the work, PtNPs were chemically deposited onto SnO_2-coated multiwalled carbon nanotubes (MWCNTs), and the effect of this support was analyzed [IV].

4. LITERATURE OVERVIEW

4.1 Oxygen reduction reaction

In the field of polymer electrolyte membrane fuel cells, the oxygen reduction reaction has been thoroughly investigated. This multistep reaction takes place in both acidic and alkaline solutions, yielding water or hydroxide ions, respectively. The 4-electron pathway in an acidic environment (Eq. 1):

$$O_2 + 4H^+ + 4e^- \rightarrow 2H_2O \qquad E^0 = 1.229\ V_{NHE} \qquad (1)$$

The 2-electron reduction in an acidic environment (Eq. 2):

$$O_2 + 2H^+ + 2e^- \rightarrow H_2O_2 \qquad E^0 = 0.67\ V \qquad (2)$$

Followed by the further electrochemical reduction of hydrogen peroxide (Eq. 3):

$$H_2O_2 + 2H^+ + 2e^- \rightarrow 2H_2O \qquad E^0 = 1.77\ V \qquad (3)$$

The 4-electron pathway in an alkaline environment (Eq. 4):

$$O_2 + 2H_2O + 2e^- \rightarrow 4OH^- \qquad E^0 = 0.401\ V \qquad (4)$$

The 2-electron reduction in an alkaline environment (Eq. 5):

$$O_2 + H_2O + 2e^- \rightarrow HO_2^- + OH^- \qquad E^0 = -0.065\ V \qquad (5)$$

Followed by the further reduction of the hydroperoxide anions (Eq. 6):

$$HO_2^- + H_2O + 2e^- \rightarrow 3OH^- \qquad E^0 = 0.867\ V \qquad (6)$$

where E^o is the standard potential. Because ORR is a surface-sensitive reaction, the tendency for ORR to occur via different pathways depends on the electrolyte, catalyst, and electrode.[1,2]

4.2 ORR on bulk Pt

The Sabatier principle states that the ideal catalytic reaction occurs when the reactant is bound by intermediate strength.[3] When an intermediate binds too strongly to the catalyst, it has a too-low turnover rate; yet when it binds too weakly, the reaction fails to occur.[4] The ideal bond strength is represented by a Balandin volcano plot, in which the Pt is situated near the peak. This representation shows that Pt has the highest activity at the optimal binding energy for ORR.[4]

The ORR on Pt can occur through either a dissociative (Eqs. 7–9) or associative mechanism (Eqs. 10–14), where * is a site on the Pt surface.[1]
The dissociative mechanism:

$$\frac{1}{2}O_2 + * \rightarrow O^* \quad (7)$$

$$O^* + H^+ + e^- \rightarrow OH^* \quad (8)$$

$$OH^* + H^+ + e^- \rightarrow H_2O + * \quad (9)$$

The associative mechanism:

$$O_2 + * \rightarrow O_2^* \quad (10)$$

$$O_2^* + H^+ + e^- \rightarrow HO_2^* \quad (11)$$

$$HO_2^* + H^+ + e^- \rightarrow H_2O + O^* \quad (12)$$

$$O^* + H^+ + e^- \rightarrow OH^* \quad (13)$$

$$OH^* + H^+ + e^- \rightarrow H_2O + * \quad (14)$$

A single-crystal Pt electrode surface has three low-index crystallographic planes on which the ORR can occur: Pt(111), Pt(110), and Pt(100). The Gibbs free energy and dissociation barriers of the intermediate species vary among the different crystallographic planes.[5] Dong et al. found that the ORR activity in a 0.1 M $HClO_4$ solution is as follows: Pt(111) > Pt(110) > Pt(100).[5] They found that the HO_2^* is more strongly adsorbed on the Pt(111) surface, as the instability of the intermediate on the Pt(110) and Pt(100) leads to the formation of the OH^* and O^*. When an O_2 molecule is bound too close to sites blocked by intermediates the O-O bond is unable to be broken.[6] In H_2SO_4 the potential in which hydrogen is adsorbed onto the Pt molecule is more positive for Pt(111) and Pt(100).[6] Pt(100) have a valley formation in which the hydrogen can be adsorbed leaving the top for the O_2 molecule to bind.[7] Stamenkovic et al. also found that in H_2SO_4 solution, the Cl^- ion affects the ORR depending on the Pt present; Pt(100) is strongly affected, whereas for Pt(111), the Cl^- has little effect.[8] Thus showing how the ORR on Pt is a surface-sensitive reaction that heavily relies on the electrolyte solution.

The surface-sensitive ORR on single-crystal Pt electrodes is further evident when looking at the Tafel slopes. Mayrhofer et al. found that Pt(111) in H_2SO_4

solution had a slope of -120 mV during the entire potential window, while Pt(110) and Pt(100) had two distinct slopes at -60 and -120 mV.[9] They attributed the different Tafel slopes to the onset of OH_{ads} adsorption, which was further evidenced by the cyclic voltammograms.[9] Tafel slopes of bulk Pt are also reliant on the electrolyte solution – this is related to the difference in anions in the solution. In a $HClO_4$ solution, the anion blocking the ORR site is OH^-, whereas in H_2SO_4 solution, the blocking anion is the bisulfate anion.[10] In a $HClO_4$ solution, Wang et al. observed two distinct slopes for Pt(111), which they attributed to a change in adsorption intermediate coverage in the mixed kinetic-diffusion controlled region of the ORR.[10]

4.3 ORR of PtNPs

The introduction of PtNPs into the electrocatalytic system is used to maximize catalyst activity, while reducing the total Pt amount. The particle-size effect states that as the particle size of a PtNP decreases, the overall activity increases.[11,12] This is because, as the PtNP size decreases, the affinity towards oxygen increases.[13–16] The improvement in oxygen affinity could result from changing the Pt planes on which oxygen can bind, thereby altering the binding energy.[17] However, the improved electrocatalytic activity is thermodynamically limited to 2–3 nm.[18] This point was further emphasized by Wikander et al., who concluded that PtNPs below 3 nm would tend to grow towards a more energetically favorable size[19] and Perez-Alonso et al. who found that there was a maximum mass activity for PtNPs around 3 nm in size.[20] Inaba et al. demonstrated this experimentally by measuring the specific activity (SA) of different sized PtNPs and found that decreasing the particle size from 3.9 to 1.8 nm decreased SA by 190%.[21] This finding was contested by Nesselberger et al., who concluded that the difference of SA within PtNPs was due more to the capacitive current effects of the support rather than the intrinsic properties of the PtNPs at varying sizes.[22] Additionally, Yano et al. found that when PtNPs were both highly dispersed on carbon black and relatively uniform in size, PtNPs around 2 nm were highly durable and maintained a kinetically-controlled mass activity that was higher than that of PtNPs that were 4 nm.[23] In PEMFC testing, Xu et al. observed that increasing the PtNP size from 2.9 to 3.5 nm reduced the ECSA loss per cycle from 0.06% to 0.03%.[24] They reported that this is because smaller particle sizes tend to lower their energy through particle growth, owing to the higher surface energy associated with inactive defect regions.[24–26] Sandbeck et al. further confirmed that Ostwald ripening drives Pt particle growth.[27] The optimal size of NPs varies though when Pt is alloyed. Gan et al. found that $PtNi_3$ catalysts have an optimal size between 6 and 8 nm.[28]

Li et al. also studied the particle-size effect on PtNPs and found that smaller nanoparticles (2.8 nm) are less stable than larger ones (7.2 nm). They also reported that at these nanoparticle sizes, the NP shape does not drastically affect the electroactivity of PtNPs.[15] However, the shape effect of the nanoparticle has been contested in the literature. Sánchez-Sánchez et al. found that the shape of

PtNPs affected electroactivity, with the following order of activity in an $HClO_4$ solution: hexagonal > tetrahedral-octahedral ≈ spherical > cubic; with the hexagonal NPs having a preference for Pt(100) and Pt(111), the tetrahedral-octahedral NPs having a preference for Pt(111) and Pt(110), the cubic having a preference for Pt(100) and the spherical having no facet preference thus showing that difference in activity is due to the surface-sensitive ORR on Pt which was previously discussed in section 4.2.[29] This change in activity could be due to the number of terrace sites in the different PtNP shapes, which are intrinsically related to Pt's electrocatalytic activity.[30]

4.4 Deposition procedures of PtNPs onto supports

For the deposition of PtNPs onto the substrate, a variety of Pt precursors have been used in the literature, including platinum(II) acetylacetonate ($Pt(acac)_2$), trimethyl(methylcyclopentadienyl)platinum(IV) ($(MeCp)PtMe_3$), and H_2PtCl_6.[31–35] The Pt precursor used influences the growth of the PtNPs, as the cations and anions in solution vary across precursors.[34,36] Jackson et al. used $Pt(acac)_2$ as their Pt precursor and were able to synthesize PtNPs with a particle size of 2.7 nm; additionally, they tested the effect of loading and found that the average particle size of their synthesized catalyst was not affected by the loading, whereas this was not the case for the commercial Pt/C catalyst. They also tested the effect of loading on the mass activity (MA) and at 20 wt% Pt, their catalyst had a MA of 426 A g_{Pt}^{-1}, which was higher than that of the commercial Pt/C, which had a MA of 271 A g_{Pt}^{-1}.[31] Woitassek et al. also used $(MeCp)PtMe_3$ as the Pt precursor; their synthesized electrocatalyst also showed higher MA than the commercial Pt/C catalyst.[32] The use of a colloidal system to synthesize PtNPs is a well-established method. It involves using a platinum precursor, a reducing agent, and a stabilizing agent. Venkateswara Rao and Viswanathan synthesized a Pt-metal electrocatalyst using $Pt(acac)_2$ as the precursor, 1,2-hexadecanediol as the reducing agent, and nonylamine and nonanoic acid as the stabilizing agents; their synthesized Pt/C catalyst had a maximum power density (P_{max}) of 10 mW cm^{-2} in a direct ethanol fuel cell, compared to 7 mW cm^{-2} of the commercial Pt/C.[36] López-Cudero et al. used H_2PtCl_4 as the precursor, $NaBH_4$ as the reducing agent, and sodium citrate as the stabilizing agent, and found that particle size was consistently between 2.1 and 2.4 nm across different Pt loadings on Vulcan carbon.[37] Alexeyeva et al. looked at how the synthesis procedure affects the electrocatalytic activity of PtNPs and found that PtNPs supported on multiwalled carbon nanotubes (MWCNTs) synthesized through microemulsion had a SA of 1.28 mA cm^{-2} in a H_2SO_4 solution, whereas those synthesized in the presence of sodium citrate had a SA of 0.39 mA cm^{-2}.[38] The entire deposition reaction usually takes place in a solvent such as ethylene glycol (EG) or water. The dispersion liquid used affects the deposition efficiency, the particle size, and the uniformity of PtNPs.[39,40] Park et al. tested tetrahydrofuran (THF), ethanol, EG, and water and found that EG had the highest deposition efficiency at 85% and the smallest crystalline size of

2.85 nm while THF had the lowest deposition efficiency at 56% and the largest crystalline size of 4.97 nm; they attributed the high deposition efficiency of the EG to its ability to act as a secondary reducing agent.[39] Wang et al. found an optimal EG-to-water ratio that yielded the smallest particle size of 2.2 nm.[40] The pH of the reaction mixture is also important when depositing PtNPs. Li et al. found that weakly acidic solutions yield smaller NPs with narrower size distributions, whereas strongly acidic solutions hinder the interaction between the support and the NPs.[39]

Another potential route for attachment of PtNPs onto a support is electrochemical deposition. This technique uses potential to reduce the Pt precursor and facilitate nucleation of Pt on the support. In this technique, the deposition potential, pulse rate, and time influence the morphology of the PtNPs.[41,42] Cao et al. electrodeposited PtNPs using the chronoamperometric technique and found that the electrochemically active surface area (ECSA) of the PtNPs decreased, as the potential became more negative.[41] They attributed this to the high current density, which allows for faster nucleation rates.[41] The deposition time is another factor that can affect the PtNP morphology. When the deposition procedure is completed quickly, the Pt nanoclusters have just undergone nucleation, and as time increases, different structures, such as flower-like structures, can form.[42] Pulse deposition employs switching a potential on and off, which creates an overpotential. The longer the on/off time, the higher the overpotential and the smaller the NP.[43] Additionally, as the number of pulses increases, the SA for ORR decreases.[44] Pulse deposition can lead to the formation of Pt agglomerations.[45] However, adding organics to the solution can help reduce the agglomeration.[42,45] Hussain et al. looked at how cyclic voltammetry, chronoamperometry, and pulse deposition affect the electrocatalytic activity of PtNPs and found that where PtNPs were deposited in an argon environment using CV the SA was 0.34 mA cm^{-2}, for those deposited using chronoamperometry at -0.3 V the SA was 0.45 mA cm^{-2}, and for those deposited using pulse deposition in a potential window from -0.3 to 1.0 V the SA was 0.34 mA cm^{-2}.[46] Thus, confirming that the choice of the electrodeposition procedure is critical.

4.5 Support effects on PtNPs towards ORR

4.5.1 Different carbon types and their effects on PtNPs

The role of the support is to provide an anchor for the PtNPs. For good electrocatalytic activity of the PtNPs, the support needs to have good electrical conductivity, be mechanically strong, allow uniform dispersion of the PtNPs, and provide strong attachment of the PtNPs. Various substrates have been proposed as supports for PtNPs, including metal oxides, carbons materials, and ceramics. Metal oxides interact with the d-band center of the PtNPs and induce a support-metal interaction, which will be more thoroughly discussed in section 4.5.2 dealing with functionalization of carbon.

Carbon supports offer unique advantages over metal oxides, including a high specific surface area and good electrical conductivity.[47] Carbon nanotubes (CNTs), graphene, and porous carbons are a few that have been used in the literature and each offer distinct advantages. In PEMFCs, CNTs can enhance gas and fluid transport through the support network, thereby enabling faster reaction kinetics.[48,49] However, the long-term stability of CNT support is an issue. Carbon corrosion of CNTs occurs during potential cycling and results in structural damage. Potential cycling causes defects in the carbon, leading to a structural change from hexagonal to heptagonal and pentagonal rings, thereby promoting the migration of the PtNPs.[50] Del Carmen Gimenez-Lopez et al. found that carbon nanofibers can aid in the stability of Pt/C catalyst, as PtNPs deposited on highly graphitized carbon nanofibers had an increase in size from 5.3 to 6.2 nm compared to PtNPs supported on commercial carbon black, which had an increase of 3.4 to 9.6 nm after durability testing; they attributed the durability of the Pt/carbon nanofiber catalyst to the internal step-edges of the carbon support which helped to form a barrier and slowed down the PtNP coalescence mechanism.[51] Thus, showing how a change in carbon support can help maintain the catalyst's electrocatalytic activity. Graphene as a support can introduce oxygen containing functional groups into the electrocatalytic system.[52] The functional groups help stabilize the PtNPs and reduce their migration by altering π-π conjugation.[53] However, certain graphene supports, such as reduced graphene oxide, have a high defect concentration, hindering the uniform dispersion of PtNPs.[54] Porous carbons offer the advantage of having pores in which the PtNPs can be anchored; not only does this decrease the rate of PtNP detachment, but it can also block the PtNPs from the ionomer.[55–58] Sakthivel and Drillet found that after accelerated durability testing (ADT), PtNPs supported on ordered mesoporous carbon increased in size from 5.2 to 6 nm and then returned to 5.2 nm, whereas those supported on Vulcan increased from 4.7 to 30 nm.[59] Common commercial supports include Vulcan carbon, graphite, ordered mesoporous carbon and carbon nanotubes.[51,59,60] These supports offer a higher specific surface area, enabling uniform dispersion of the PtNPs.[61] One common drawback of all types of carbon supports is that carbon corrodes during the startup of PEMFCs.[1] Carbon corrosion was observed in aged Pt/C catalysts. Zhao et al. aged a Pt/Vulcan catalyst for 1.5, 2.5, and 3.5 years and observed a relatively unchanged Pt crystalline size and saw evidence for carbon corrosion in the aged supports.[60] In PEMFC testing, Li et al. observed membrane electrode assembly (MEA) degradation due to carbon corrosion, resulting in a 48% decrease in peak power density.[62] These effects can be minimized through the functionalization of the carbon supports by the addition of dopants and metals into the carbon system.

4.5.2 Functionalization of carbon

Doping the carbon support with single heteroatom dopants can enhance the electrocatalyst's overall ORR activity.[63,64] Heteroatom dopants are usually either n-type dopants, which are electron-donating, or p-type dopants, which are

electron-withdrawing. Nitrogen, sulfur, phosphorus, and boron are common heteroatom dopants reported in the literature. Pyridinic nitrogen is of particular interest because it has been shown to shift the Fermi level of PtNPs and enhance overall electrocatalytic activity.[65] Additionally, pyridinic nitrogen can interact with the Pt d5 orbital due to its lone pair electrons and form a Pt-N bond, resulting in a suppression of Pt migration.[66] Pyridinic nitrogen has also been found to interact with sulfonic groups in the ionomer, thereby improving ionomer dispersion.[67] Additionally, PtNPs tend to bind to carbon atoms rather than N atoms; the N atoms can act as a pseudo-barrier, enhancing the durability of the electrocatalyst.[68] Xie et al. attached PtNPs to single-walled carbon nanohorns via EG reduction; they obtained PtNPs around 3 nm, with slight variations depending on the nitrogen-doping level.[69] They found that there was a critical amount of 3% N at which the catalytic durability changed from highly durable to fragile, due to an increase in amorphous carbon in the system, leading to the detachment of PtNPs after the stability testing.[69] Müller et al. found that the number of micro and mesopores decreases with the introduction of N-doping into the carbon catalyst, yet found that the introduction of the dopant did not have an effect on the Pt crystalline size.[64] Adding sulfur to the carbon lattice has also been shown to improve the electrocatalyst's durability.[70,71] Haque et al. attached Pt nanoclusters to sulfur-doped CNTs and found that the addition of the sulfur dopant enhanced the anchoring of the PtNPs, which resulted in a loss of 12% ECSA after durability testing compared to commercial Pt/C, which lost 27% of ECSA.[70] Sulfur can also help reduce sintering by slowing Ostwald ripening.[71] Boron and phosphorus dopants have also been shown to enhance the catalyst's electrocatalytic activity. Boron has been shown to reduce the electrocatalyst's resistivity.[72] Liu et al. doped Vulcan carbon with boron via the pyrolysis of H_2PtCl_6 and H_3BO_3 and found that the boron helped to prevent chemically deposited PtNPs from agglomeration after ADT experiments, resulting in a drop in mass activity of 19.7%, which was less than the drop in MA of the commercial Pt/C catalyst, which was 58.7%.[73] A phosphorus dopant has been shown to increase the MA of the electrocatalyst; Shen et al. supported PtCoNPs on P-doped Ketjen black and saw a 4.5 times higher MA as compared to Pt/C.[74] However, the introduction of phosphorus into the electrocatalytic system has also been shown to enhance the catalyst's capacitance.[75]

When dopants are combined to form a dual heteroatom-doped electrocatalyst, the two dopants can exhibit a synergistic effect.[72,76,77] Liu et al. found that PtNPs deposited using an EG reduction method onto N,P dual-doped CNTs had a Pt particle size of 1.48 nm, which was smaller than their single-doped counterparts of 1.80 and 1.63 nm for phosphorus and nitrogen-doped CNTs, respectively.[78] Additionally, Ukai et al. tested the effects of N,P dual heteroatom-doped carbon shell on PtNPs electrocatalytic activity in a KOH solution and found that the dual heteroatom dopants enhanced the charge transfer kinetics while suppressing PtNP agglomeration, leading to a more stable catalyst.[77] Renugadevi et al. deposited PtNPs onto sulfur and nitrogen dual heteroatom-doped reduced graphene oxide;

their synthesized catalyst exhibited superior stability compared to commercial Pt/C, in that the synthesized catalyst had a 7.2% loss in ECSA compared to the 34.7% loss in Pt/C.[79] They suggested that the improved stability of the dual heteroatom-doped catalyst was due to heteroatoms stabilizing the PtNPs and acting as additional active sites for which the ORR could occur.[79] Fan et al. found that the addition of S dopant into the N,S dual-doped carbon support reduces the electron density around the Pt and promotes Pt-C coordination resulting in a catalyst that retained 78% of its MA after ADT.[80] In contrast, Perazzolo et al. found that N,S dual heteroatom-doped carbon had lower electrocatalytic activity than their single-doped counterparts; they attributed this to the weak Pt interaction with the multi-defect surface of the dual heteroatom-doped substrate.[58] Zhu et al. found that the introduction of N and B dopants into graphene can lead to higher dispersion of PtNPs when compared to commercial Pt/C, resulting in an electrocatalyst with an MA of 213.6 mA mg^{-1} as compared to the commercial Pt/C with an MA of 104.1 mA mg^{-1}.[76] It was also found that the addition of B and N into the carbon nanofibers results in better durability, with the synthesized electrocatalyst maintaining 90.4% of its MA after ADT as compared to the commercial Pt/C, which retained 50.6%; with the synthesized electrocatalyst maintaining its original initial morphology suggesting that the steric hindrance induced by the dopants can aid in mitigating the formation of PtNP agglomerations.[63]

Another functionalization technique to improve the activity and durability of Pt/carbon electrocatalyst is the addition of metal into the system. The improved durability of a metal-carbon support was demonstrated by Pan et al., who found that the adsorption energy of the OH intermediate was the weakest on an aluminum-nitrogen-carbon support, resulting in a PtNP catalyst with lower ECSA loss than commercial Pt/C after durability testing.[81] Jin et al. tested the effect that the addition of Fe into the nitrogen-doped carbon electrocatalytic system had and reported that a 1:1 Pt-to-Fe ratio resulted in an $E_{1/2}$ of 0.95 V, which was higher than that of Pt/C ($E_{1/2}$ = 0.88 V).[82] The addition of metal oxides such as TiO_2, Ta_2O_5, and SnO_2 has been shown to improve the durability of the electrocatalyst, anchoring of the PtNPs, and induce metal-support interactions.[83–85] Niu et al. found that when Pt was supported on TiO_2/carbon nanospheres durability increased, which they attributed to enhanced metal-support interactions induced by oxygen vacancies in their material.[83] Liu et al. deposited PtNPs onto a nitrogen-doped titania-carbon composite support and reported a strong metal-support interaction (SMSI) that allowed for preferred nucleation sites of the Pt onto TiO_2-N, culminating in a reduction of carbon corrosion.[86] PtNPs supported on highly crystalline Ta_2O_5/CNTs have a higher preference for Pt(111) and Pt(100) planes, which results in a higher electrocatalytic activity.[84] The addition of Ta_2O_5 to the support provides strong anchoring of the PtNP, thereby increasing durability during ADT.[84] Zhang et al. supported PtNPs on TaO_x-Ketjen Black carbon and found that TaO_x transferred electrons to Pt, resulting in an SMSI; in PEMFC testing, their synthesized electrocatalyst had a P_{max} of 2.29 W cm^{-2}, compared to Pt/KJ, which had a P_{max} of 1.8 W cm^{-2}.[87] SnO_2 is of particular interest due to its

stability in acidic environments.[85] SnO_2 induces an SMSI.[47,88] When PtNPs are supported on SnO_2/mesoporous carbon, the overall electrochemical activity is increased compared to commercial Pt/C.[89] Guan et al. synthesized a Pt-SnO_2 hybrid supported on carbon, which had a MA of 0.46 A mg_{Pt}^{-1}, which was 5.8-fold higher than that of Pt/C.[85] The addition of SnO_2 to the support has been shown by Elezovic et al. to improve durability compared to the commercial Pt/C catalyst.[90] Adding SnO_2 to the electrocatalytic system is also useful in PEMFCs, as it allows for drier conditions.[91] PtNPs supported on W-SnO_2-carbon have been used for PEMFC testing and had a 89% retention of peak power density after 50,000 cycles.[92] Thus, the functionalization of carbon support is a key component in improving the electrocatalytic activity and durability of the PtNPs.

4.6 PtNPs on carbon supports used in the PEMFC cathode

PEMFCs are one example of a device that employs ORR to provide energy. PEMFCs are important because they can be used in the transportation sector and help reduce global reliance on fossil fuels. This is essential, as EU Regulation 2019/1242 requires manufacturers to reduce CO_2 emissions by 90% by 2040 relative to 2019 levels.[93] The Pt/C catalyst is used on both the anode and the cathode of the PEMFC. In PEMFCs, the anodic reactions are fast and have thus been thoroughly optimized. However, significant effort is being made to improve the sluggish ORR kinetics at the cathode. This is done through optimization protocols that employ the synthesis methods discussed in the previous sections. It is important to note that the testing environment for RDE measurements differs from that in PEMFCs, and thus, the fuel cell optimization is also required. One such example is the ionomer used in MEA fabrication, which is a known contaminant of PtNPs. However, the ionomer must fully coat the PtNPs in order to maintain an active electrocatalyst as the ionomer acts as proton conductor.[94] Liu et al. found that PtNPs supported on nitrogen-doped high-surface-area carbon, improves the uniformity of the ionomer layer, as the pyridinic N in the carbon support enhances the adsorption of the ionomer side chains.[95] Additionally, an ionomer-to-catalyst (I/C) ratio that is too high can impede oxygen diffusion across the cathode.[94,96] Yet the optimal I/C ratio is highly dependent on the morphology of the carbon itself as it behaves differently when mixed with ionomer.[97] Yang et al. performed a single-fuel-cell test of Pt on boron-doped porous graphene, porous graphene, and carbon, yielding P_{max} of 2.01, 1.61, and 1.75 W cm^{-2}, respectively.[98] Illustrating that the carbon support has a significant role in the overall electrocatalytic activity of the PtNPs. This point was further illustrated by Arici et al. who used graphene nanoplates, carbon black, and composite of carbon black and graphene nanoplatelets, as supports for PtNPs in PEMFC testing and reported P_{max} of 247, 178, and 377 mW cm^{-2}, respectively.[99] Porous carbon is of particular interest in PEMFC as the structure of the pores express unique properties. The pores have been shown to protect the PtNPs from

ionomer poisoning as the solvent can prevent the ionomer from entering the pores and protect the PtNPs.[100] Li et al. tested PtNPs on porous carbon which had a P_{max} of 591 mW cm^{-2} and saw that there was no distinct ionomer layer boundaries.[101]Another factor to the fuel cell performance is the degradation of the PEMFC due to carbon corrosion and Pt degradation, as the difference in overpotential across the cathode can lead to varied degradation.[102] Thus, the overall optimization of the cathode layer is important. Further confirming how the introduction of heteroatom dopants into the electrocatalytic system can increase the electrocatalytic activity of the catalyst.

5. EXPERIMENTAL

5.1. Preparation of GC electrodes

Glassy carbon (GC) rods (GC20-SS, Tokai Carbon, Japan) with a diameter of 0.5 cm were cut into electrodes. Then the GC electrodes were pressed into Teflon holders. The GC electrodes were then polished to a mirror finish using aqueous slurries of 1.0 and 0.3 μm alumina (Buehler). The polishing residues were removed from the electrodes through sequential sonication for 5 min in Milli-Q water (Millipore Inc.), isopropanol (≥99.8%, Honeywell), and once again in Milli-Q water.

5.2 Modification of the electrode with heteroatom-doped graphene prior to electrochemical deposition of PtNPs

Commercially available nitrogen-doped graphene (NGr), sulfur-doped graphene (SGr), phosphorus-doped graphene (PGr), boron-doped graphene (BGr), nitrogen-phosphorus co-doped graphene (NPGr), nitrogen-boron co-doped graphene (NBGr) (Graphitene Ltd.), and Vulcan carbon XC-72R (VC) (Cabot Corp.) were used as carbon supports. A carbon support ink (1 mg mL^{-1}) was prepared such that for every mg of catalyst, there were 0.7 mL of Milli-Q water and 0.3 mL of isopropanol. The ink was homogenized via sonication. 20 μL of the ink was then drop-cast onto the GC electrode in 5 μL aliquots under rotation at 500 rpm, followed by drying under a steady stream of N_2 gas, resulting in a total catalyst loading of 20 μg cm^{-2}.

5.3 Electrodeposition of PtNPs onto heteroatom-doped graphene

PtNPs were electrochemically deposited onto a previously conditioned electrode in 0.1 M $HClO_4$ solution containing 1 mM H_2PtCl_6 using a conventional three-electrode cell. The cell contained a Pt wire as the counter electrode and a saturated calomel electrode (SCE) as the reference electrode. The electrodes were conditioned in an Ar-saturated solution by running five cyclic voltammograms (CVs) from 0.05 to 1.45 V_{RHE} at a sweep rate (ν) of 50 mV s^{-1} to ensure the electrode surface was clean. An Autolab PGSTAT30 potentiostat/galvanostat (Metrohm Autolab, The Netherlands) was employed for electrochemical experiments. The PtNPs were deposited by chronoamperometry according to the protocol described by Hussain et al.[46] Briefly, the electrode potential was set to -0.30 V vs SCE for 30 s under rotation at 500 rpm to ensure constant mass transfer. Immediately after electrodeposition, the working electrode was removed from the deposition bath and rinsed with water to ensure deposition was completely stopped. The synthesized catalysts are referred to as Pt/NGr_{ED}, Pt/SGr_{ED}, Pt/PGr_{ED}, Pt/BGr_{ED}, $Pt/NPGr_{ED}$, $Pt/NBGr_{ED}$, and Pt/VC_{ED}.

5.4 Chemical deposition of PtNPs onto heteroatom-doped graphene

PtNPs were synthesized onto commercially available NGr, SGr, PGr, NPGr, and nitrogen-sulfur co-doped graphene (NSGr) (Graphitene Ltd.) and Vulcan carbon, using the sodium citrate method in which 2.5×10^{-4} M of H_2PtCl_6 (99.9%, Aldrich), was reduced by 0.01 M of ice-cold sodium borohydride ($NaBH_4$) (99%, Sigma-Aldrich) in the presence of 2.5×10^{-4} M sodium citrate (99.0%, Fluka). After the solution rested for 15 min, the allocated support was added under magnetic stirring such that the final catalyst had a Pt loading of 20 wt%. The solution was then alternated between 10 min of magnetic stirring and 30 s of sonication for a total of 1.5 h. The pH of the solution was then altered and allowed to rest overnight. The solution was centrifuged, washed with Milli-Q water three times, and dried at 75 °C overnight. The synthesized catalysts are referred to as Pt/NGr_{CD}, Pt/SGr_{CD}, Pt/PGr_{CD}, $Pt/NPGr_{CD}$, $Pt/NSGr_{CD}$, and Pt/VC_{CD}.

An ink was prepared such that for every mg of catalyst, there was 0.7 mL of Milli-Q water, 0.2 mL of isopropanol, and 0.1 mL of 5 wt% Nafion ionomer solution (in lower alcohols and water, Ion Power). The ink was homogenized via sonication. 20 µL of the ink was drop-casted onto a GC electrode substrate in 5 µL aliquots, resulting in a nominal Pt loading of 20 μg_{Pt} cm^{-2}.

5.5 Synthesis of Pt/NC catalyst

5.5.1 Ionothermal synthesis of NC

A salt-assisted/ionothermal carbonization approach was used to prepare the carbon support.[103] A 1:2 mass ratio of β-cyclodextrin (97%, Aldrich) precursor and $Mg(NO_3)_2{\cdot}6H_2O$ (98%, Alfa Aesar) template was mixed together in a mortar and pestle. The powder was then pyrolyzed in a tube furnace (EST 1200, Carbolite) at 800 °C for 1 h, with a ramping rate of 10 °C min^{-1} in constant N_2 flow. The template was then removed via acid leaching treatment in 1.0 M HNO_3 (≥65%, Sigma-Aldrich) for 2 h at room temperature. The carbon material was washed with Milli-Q water, filtered, and dried overnight in an oven (Memmert) at 60 °C. The material underwent a second pyrolysis at 800 °C for 1 h, with a ramping rate of 50 °C min^{-1} under a constant N_2 flow.

5.5.2 Chemical deposition of PtNPs onto NC

PtNPs were deposited onto the NC support using the sodium citrate method with two different synthesis routes. In the one-pot method, the NC support was added before $NaBH_4$. In the two-pot method, the NC support was added to the solution after $NaBH_4$. The total substrate added was such that the final catalyst loading was 40 wt% Pt. Both solutions were homogenized by alternating 15 min of magnetic stirring and 30 s of sonication for a total of 1.5 h. The pH of the solution

was then adjusted with KOH (89.9%, Lach-Ner) and allowed to precipitate overnight. The solution was then filtered, washed with Milli-Q water, and dried overnight at 60 °C. The synthesized catalysts are referred to as Pt/NC-1pot and Pt/NC-2pot.

An ink was prepared such that for every mg of catalyst, there was 0.7 mL of Milli-Q water, 0.6 mL of isopropanol and 0.2 mL of 5 wt% Nafion ionomer solution (in lower alcohols and water, Ion Power). The ink was homogenized via sonication. 20 µL of the ink was drop-casted onto a GC electrode substrate rotating at 500 rpm in 5 µL aliquots under a steady stream of N_2 gas, resulting in a total catalyst loading of 76.5 μg_{Pt} cm^{-2}. Commercial 46% Pt/C (Tanaka) was used for comparison.

5.6 Synthesis of Pt/SnO_2CNT catalyst

5.6.1 Preparation of SnO_2 and MWCNT composite by ALD

A 4:1 v/w suspension of acid-washed MWCNTs (purity > 95%, NanoLab Inc.) in dimethylformamide (99.8%, Aldrich) was drop-cast onto silicon plates such that the MWCNT loading was 0.2 mg cm^2 in an oven set to 115 °C. Tin dioxide films were grown from tetrakis(dimethylamido)tin(IV) (TDMASn) and ozone (O_3) at 200 °C in a low-pressure, flow-type, hot-wall atomic layer deposition (ALD) reactor. TDMASn (99% (99.99%-Sn), Strem Chemicals, Inc.) was vaporized from a semi-open glass boat; the reactor interior was maintained at 28–30 °C. A BMT Messtechnik 802 N was used to produce O_3 from O_2 (99.999%, Linde). The O_3 was measured using a BMT Messtechnik 964 analyzer and found to be 210–230 g m^{-3}. The precursors were pulsed into the reactor separately and alternated by computer-controlled solenoid valves using dry and inert N_2 gas (99.999%, Linde) flow as the precursor carrier, switching and reactor purging media. During depositions, the total gas pressure in the reaction zone ranged from 210 to 240 Pa. Real-time quartz crystal microbalance studies were performed prior in order to optimize deposition parameters and enable reliable self-limited (ALD-type) film growth. ALD cycle times of 1-2-2-5 s for the metal precursor supply, first N_2 purge, the oxygen precursor supply, and a second N_2 purge, respectively, appeared to be sufficient for the film growth on planar substrates. To enhance the precursor infiltration into the porous CNT-loaded samples and the subsequent removal of reaction byproducts, the ALD cycle times were increased to 10-20-20-40 s.

5.6.2 Chemical deposition of PtNPs onto SnO_2/MWCNT

PtNPs were chemically deposited onto the SnO_2/MWCNT substrate using the sodium citrate method (see sections 5.4 and 5.5.2). The total substrate added was such that the final catalyst loading was 20 wt% Pt. The suspension was filtered, washed, and dried overnight. The synthesized catalyst is promptly referred to as Pt/SnO_2–CNT.

An ink (1 mg mL^{-1}) was prepared such that for every mg of catalyst, there was 0.7 mL of Milli-Q water, 0.2 mL of isopropanol, and 0.1 mL of 5 wt% Nafion ionomer solution (in lower alcohols and water, Ion Power). The ink was homogenized via sonication. 20 µL of the ink was drop-casted onto a GC electrode substrate rotating at 500 rpm in 5 µL aliquots under a steady stream of N_2 gas, resulting in a total catalyst loading of 20 μg_{Pt} cm^{-2}. Commercial 20% Pt/C (E-TEK, Inc.) was used for comparison.

5.7 Physicochemical characterization

N_2 adsorption/desorption isotherms of the NC supports were obtained using a NovaTouch LX2 analyzer (Qantachrome) at 77 K, the boiling point of N_2. The Brunauer-Emmett-Teller (BET) theory was used to determine the specific surface area (S_{BET}). The total pore volume (V_{tot}) was measured at $P/P_0 = 0.97$. Prior to the measurements, the carbon support was degassed in a vacuum for 12 h at 200 °C. The quenched solid density functional theory (QSDFT) equilibrium model for slit-syl type pores was used to calculate the pore size distribution. TouchWin 1.11 software (Quantachrome Instruments) was used for all BET calculations.

X-ray photoelectron spectroscopy (XPS) analysis was carried out on a SCIENTA SES-100 spectrometer equipped with a Mg Kα X-ray source (incident energy 1253.6 eV). X-ray diffraction (XRD) analysis was done with a Bruker D8 Advance diffractometer from 10–95° 2Θ, with a step of 0.015° 2Θ, with a total counting time of 576 s per step. Cu Kα radiation and an LNXEYE XE-T detector were used for the XRD measurements. XRD calculations were performed with Topas 6 software (Bruker).

The catalyst morphologies were characterized using a Helios Nanolab 600 (FEI) scanning electron microscope (SEM) with an INCA Energy 350 (Oxford Instruments, Abingdon, UK) system for energy-dispersive X-ray spectroscopy (EDS). Their morphology was further characterized by a Titan Themis 200 (FEI) scanning transmission electron microscope (STEM) with a Super-XTM X-ray detection system for EDS (FEI/Bruker). The STEM analysis was performed at 200 kV. For the STEM analysis, the catalyst suspension in isopropanol was drop-cast onto holey carbon film-coated copper TEM grids (Agar Scientific Ltd.). The particle size distribution was assessed using ImageJ software.

The Pt amount of the catalysts were confirmed using an X-ray fluorescence (XRF) spectrometer ZSX400 (Rigaku). Micro-Raman spectra were recorded in backscattering geometry on an inVia Renishaw spectrometer in conjunction with a confocal microscope (Leica Microsystems CMS GmbH, 50× objective) and an argon ion laser operated at 514.5 nm. Low incident laser power density at the sample prevented excessive sample heating and/or decomposition while allowing for averaged information over ~200 μm^2 area in a single exposure. A baseline correction was applied to compensate for low fluorescence background, and a multiple-peak fitting procedure was performed using the PeakAnalyzer software in OriginPro 9. The intensities of I_{D1} and I_{G+D2} (integrated areas under the bands)

as well as their half widths were extracted from the fitting of the curves using Voigt functions. In the curve-fitting procedure, all parameters (peak position, height, and width) were adjusted to attain the smallest value of the chi-square.

5.8 Electrochemical measurements

5.8.1 Rotating disk electrode experiments

The electrochemical measurements were conducted in a 0.1 M $HClO_4$ (70%, Sigma-Aldrich) solution using a conventional three-electrode cell paired with an Autolab PGSTAT30 potentiostat/galvanostat and controlled with General Purpose Electrochemical System (GPES) program. The counter electrode was a Pt wire and the reference electrode was a reversible hydrogen electrode (RHE). CO electro-oxidation was employed to ensure the electrode's cleanliness and to further investigate their electrocatalytic behavior. The electrochemical cell was held at a constant potential of 0.1 V, while CO (99.97%, Linde) was bubbled through the solution until the PtNPs were entirely covered. The solution was then purged with Ar (99.999%, Linde) and the adsorbed CO was stripped from the PtNPs electrochemically in a potential window of 0.05–1.0 V using a scan rate of (ν) of 20 mV s^{-1}. CVs were recorded from 0.05–1.45 V using a scan rate of 50 mV s^{-1}. The rotating disk electrode (RDE) technique was used to investigate the ORR using an EDI101 rotator and a CTV101 speed control unit (Radiometer). The potential was scanned between 0.05 and 1.1 V_{RHE} using a scan rate of 10 mV s^{-1} at the following rotation rates (ω): 360, 610, 960, 1900, 3100, and 4600 rpm; under an O_2 environment (99.999%, Linde). The long-term durability of the catalysts were examined by accelerated durability testing (ADT) which subjected the catalysts to repetitive potential cycling in Ar-saturated 0.1 M $HClO_4$ solution.

5.8.2 MEA construction and PEMFC tests

The Pt/NC-1pot PEMFC cathode was prepared by dispersing 13 mg of Pt/NC-1pot in a 1:5 water-to-isopropanol mixture, resulting in a total volume of 2.2 mL. The Pt/NC-2pot cathode was prepared by dispersing 14 mg of Pt/NC-2pot in a 1:4 water-to-isopropanol mixture, resulting in a total volume of 2.4 mL. The resulting catalyst inks were of different volumes to ensure similar Pt loadings. Both mixtures contained an I/C ratio of 8. The Pt/C anode ink was prepared by dispersing 12 mg of 46% Pt/C in a 1:14 water-to-isopropanol mixture of 1.9 mL with an I/C ratio of 0.7. The inks were then sonicated in an ice bath for 1 h and stirred overnight on a magnetic stirrer. The membrane-electrode assemblies were prepared by spray-coating the inks onto the gas diffusion layers (GDLs, Sigracet S22BB) using an airbrush (Harder & Steenbeck). Prior to spray coating, the inks were sonicated in an ice bath for 2 h. The cathode loadings were 0.25 and 0.24 mg_{Pt} cm^{-2} for Pt/NC-1pot and Pt/NC-2pot cathodes, respectively. The anode loading was 0.21 and 0.27 mg cm^{-2} for the Pt/NC-1pot and Pt/NC-2pot PEMFC, respectively. The gas diffusion electrodes were then pressed together with a

Nafion 211 proton exchange membrane (Fuel Cell Store) and Teflon gaskets at 135 °C with 1.7 MPa, resulting in a gas diffusion electrode compression of around 30%. The MEA was then assembled in a test cell (Fuel Cell Technologies Inc.) between 5 cm^2 serpentine graphite bipolar flow field plates with a torque of 7 N m. The polarization curves were measured with a Greenlight Fuel Cell Test Station (G40 Fuel Cell System, Hydrogenics) at 80 °C and a backpressure of 170 kPa. H_2 and O_2 gases were flowed into the system at a constant rate of 0.5 NLPM. The dewpoints of both the anode and cathode were set at 78 °C. Prior to measuring the polarization curves, the cell underwent an activation stage in which the system was held at open circuit voltage (OCV) for 5 min, 0.85 V for 10 min, and 0.60 V for 45 min, twice.

6. RESULTS AND DISCUSSION

6.1 The ORR on electrochemically deposited PtNPs supported on heteroatom-doped graphene

6.1.1 Surface morphology of electrochemically deposited PtNPs on heteroatom-doped graphene

The surface elemental composition of Pt/NGr_{ED}, Pt/PGr_{ED}, and Pt/$NBGr_{ED}$ materials was confirmed through XPS (Figure 1). All three catalysts showed a strong C 1s peak at 284 eV.[104] The Pt/NGr_{ED} and Pt/$NBGr_{ED}$ electrocatalysts had a N 1s peak at 389.3 eV.[105] The Pt/PGr_{ED} electrocatalyst had a P 2p peak at 133 eV.[75] The Pt/$NBGr_{ED}$ electrocatalyst had a B 1s peak at 191 eV.[106] All electrocatalysts had Pt 4f peaks at 71.1 and 74.3 eV.[107,108] Thus confirming the elemental composition of the commercially available graphene and the deposition of PtNPs.

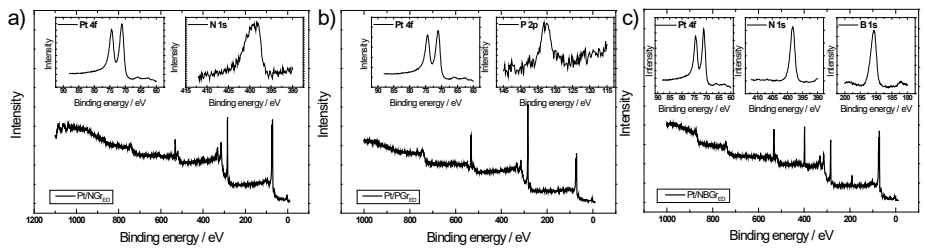

Figure 1. XPS survey spectra for a) Pt/NGr_{ED}, b) Pt/PGr_{ED} and c) Pt/$NBGr_{ED}$ samples. Insets: detailed XPS spectra in different regions.

SEM images (Figure 2) show uniformly deposited PtNPs among the different electrocatalysts. Additionally, the SEM images show that the Pt particle density is dependent on the heteroatom dopant. This is exemplified by Pt/$NBGr_{ED}$ and Pt/SGr_{ED}, in which the particle densities are 821 and 528 particles μm^{-2}, respectively. However, the particle sizes are consistent across the different electrocatalysts, ranging from 16.2 to 17 nm, except for Pt/PGr_{ED}, which had a particle size of 12.8 nm. The Pt loading was also varied amongst the different supports: Pt/SGr_{ED} (18%), Pt/PGr_{ED} (17%), Pt/NGr_{ED} (16%), Pt/$NBGr_{ED}$ (14%), Pt/$NPGr_{ED}$ (12%), and Pt/BGr_{ED} (12%). Based on the XRF results, the dual-heteroatom electrocatalysts tend to have lower Pt loading than those on single-heteroatom-doped graphene. It has been shown that the number density of functional groups correlates with PtNP nucleation.[109] This is because PtNP nucleation over defects is energetically more favorable. Nucleation of PtNPs near electropositive atoms produces a strong bond, and thus PtNPs will bond with dopants such as B, whereas more electronegative dopants tend to repel the Pt.[110] Thus, it can be concluded that the support material onto which the Pt is deposited affects the amount of Pt nucleation.

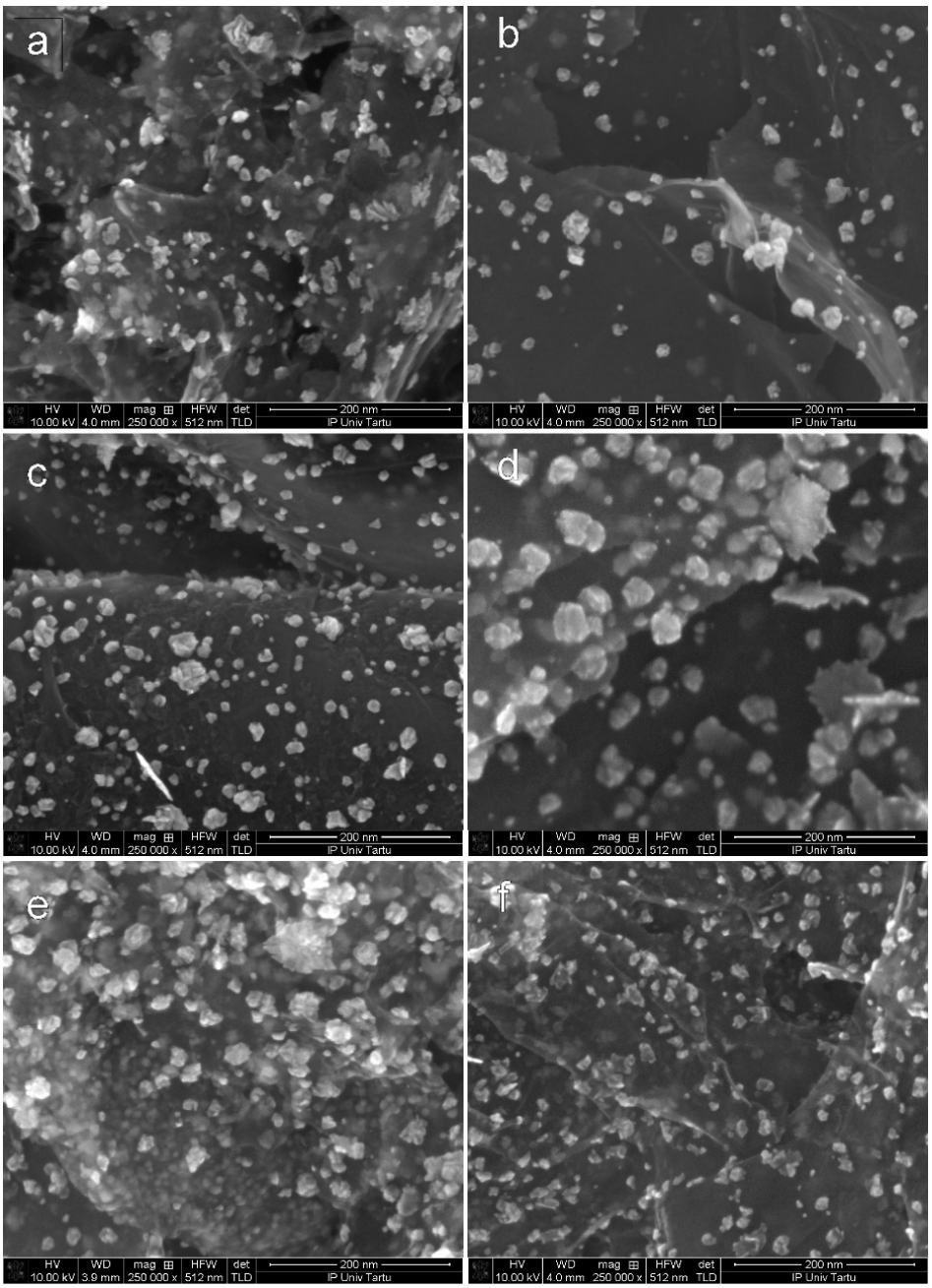

Figure 2. SEM images of a) Pt/NGr$_{ED}$, b) Pt/SGr$_{ED}$, c) Pt/PGr$_{ED}$, d) Pt/BGr$_{ED}$, e) Pt/NBGr$_{ED}$, and f) Pt/NPGr$_{ED}$ samples.

6.1.2 Electrochemical characterization of electrochemically deposited PtNPs on heteroatom-doped graphene

The CVs of the PtNPs deposited on single heteroatom-doped graphenes are presented in Figure 3a and the PtNPs deposited on dual heteroatom-doped graphenes are presented in Figure 3b. All of the electrocatalysts show similarities in the hydrogen adsorption/desorption region. The differences occur at the Pt oxide reduction peak and the quinone and hydroquinone peaks. Pt/BGr_{ED} and Pt/$NBGr_{ED}$ show more electrochemical double-layer capacitance (EDLC) characteristics than the other electrocatalysts. This suggests that the change in CV profiles is due to the boron dopant. The differences in EDLC behavior amongst the different electrocatalysts could also be due to the different oxides formed on the carbon support, which vary with the heteroatom dopants.[111] The ECSA of the electrocatalysts were calculated by integrating the area under the hydrogen desorption peak with the assumption that the charge density required for the desorption of a monolayer of adsorbed hydrogen from the Pt surface is 210 μC cm^{-2},[9] the ECSA of the catalysts are presented in Table 1. Interestingly, the only synthesized carbon with a higher ECSA than the commercial catalyst (0.46 cm^{-2}) was the Pt/$NBGr_{ED}$ (0.54 cm^{-2}). The ECSA of the catalysts are as follows: Pt/$NBGr_{ED}$ > Pt/VC > Pt/$NPGr_{ED}$ > Pt/PGr_{ED} > PtSGr_{ED} > Pt/NGr_{ED} > Pt/BGr_{ED}. The trend shows that the PtNPs supported on dual heteroatom-doped supports have a higher ECSA than the single heteroatom supports.

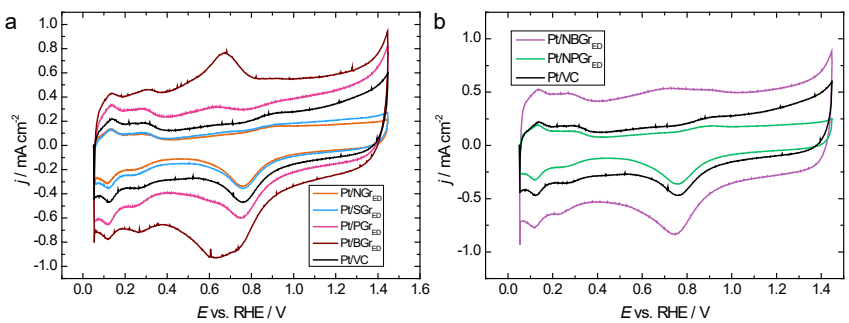

Figure 3. Comparison of CV curves of a) electrochemically deposited PtNPs supported on single heteroatom-doped graphenes and b) electrochemically deposited PtNPs supported on dual heteroatom-doped graphenes in Ar-saturated 0.1 M $HClO_4$ solution (ν = 50 mV s^{-1}). The current densities are normalized to the geometric surface area of GC.

6.1.3 ORR studies on electrochemically deposited PtNPs on heteroatom-doped graphene

The ORR results of the PtNPs deposited on single heteroatom-doped graphenes are presented in Figure 4a and the PtNPs deposited on dual heteroatom-doped graphenes are presented in Figure 4b. At potentials lower than 0.2 V, there is a decrease in current density. This can be attributed to the blockage of the ORR-active site by hydrogen adsorbed on the Pt surface.[112] Figure 5a shows the RDE polarization curves for oxygen reduction on Pt/PGr$_{ED}$ at different rotation rates and confirms that diffusion-limited current densities are consistently achieved across rotation rates.[113] All other catalysts showed similar results.

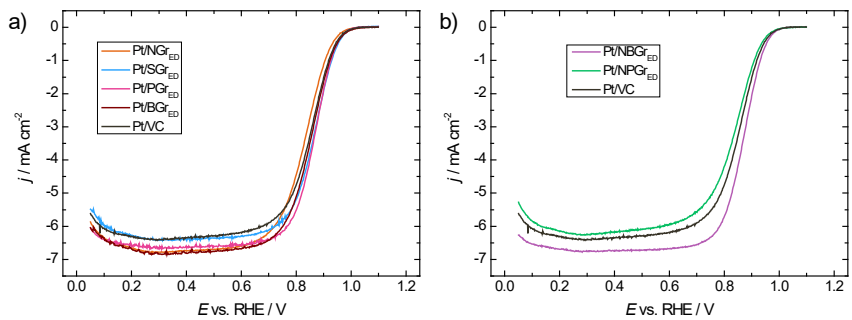

Figure 4. Comparison of ORR polarization curves for a) electrochemically deposited PtNPs supported on single heteroatom-doped graphenes and b) electrochemically deposited PtNPs supported on dual heteroatom-doped graphenes in O_2-saturated 0.1 M $HClO_4$ solution at 1900 rpm (v = 10 mV s^{-1}).

From the RDE polarization curves of ORR on PtNPs supported on doped graphenes, the half-wave potentials ($E_{1/2}$) were determined and compared in Table 1. The PtNPs supported on N,B co-doped graphene had the highest $E_{1/2}$ of 0.87 V. Pt/SGr$_{ED}$ (0.86 V) and Pt/PGr$_{ED}$ (0.86 V), showed higher $E_{1/2}$ values than Pt/VC (0.85 V), while Pt/BGr$_{ED}$ (0.85 V) was the same as Pt/VC. There were only two heteroatom-doped supports of which the PtNPs exhibited lower $E_{1/2}$ than that of Pt/VC; Pt/NGr$_{ED}$ (0.84 V) and Pt/NPGr$_{ED}$ (0.84 V). As the $E_{1/2}$ values differ across catalysts, this confirms that the heteroatom used for graphene doping plays an important role in the overall electrocatalytic activity of the PtNPs and thus warrants further exploration. The difference could be due to differences in the electron density of the PtNPs resulting from the dopant used, thereby affecting the bonding strength of the O_2 molecule to the Pt.[58,68] This effect was explained by Zhu et al., who showed that the N,B dual heteroatom-doped graphene transferred electrons to the unfilled Pt orbitals, thereby lowering the O_2 adsorption barrier and increasing overall electrocatalytic activity.[76]

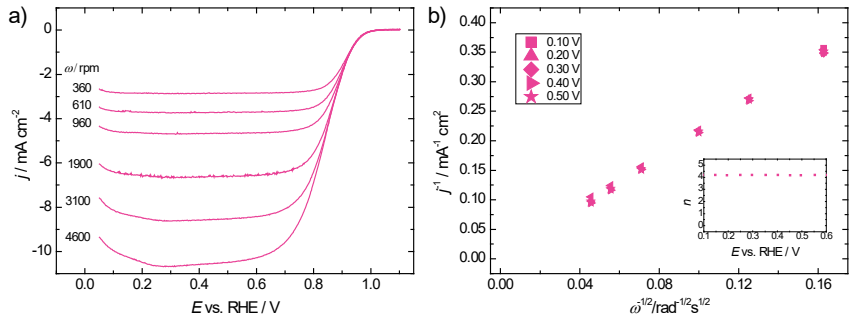

Figure 5. a) RDE polarization curves for ORR on Pt/PGr$_{ED}$ in O_2-saturated 0.1 M $HClO_4$ (v = 10 mV s^{-1}). b) K-L plots derived from a). Inset shows the potential dependence of n.

The electrochemical data was analyzed via the Koutecký–Levich (K-L) equation (Eq. 15):[113]

$$\frac{1}{j} = \frac{1}{j_k} + \frac{1}{j_d} = -\frac{1}{nFkC_{O2}^b} - \frac{1}{0.62nFD_{O2}^{2/3}v^{-1/6}C_{O2}^b\omega^{1/2}} \tag{15}$$

where j is the measured current density, j_k and j_d are the kinetic and diffusion-limited current densities, respectively, n is the electron transfer number, k is the ORR rate constant, F is Faraday's constant (96,485 C mol^{-1}), ω is the electrode rotation rate, C^b_{O2} is the O_2 concentration in the bulk solution (1.22×10^{-6} mol cm^{-3}),[114] D_{O2} is the O_2 diffusion coefficient (1.93×10^{-5} cm^2 s^{-1}),[114] and ν is the kinematic viscosity of the electrolyte solution (0.01 cm^2 s^{-1}).[114] Figure 5b shows the K-L plot for Pt/PGr$_{ED}$ with an inset of n *vs.* E. The number of electrons transferred during ORR was determined to be approximately 4 for all synthesized catalysts. This confirms that the final product is H_2O, not H_2O_2. The generation of hydrogen peroxide severely degrades cathodes by producing radicals in the fuel cells.[115,116] Bai et al. found that PtNPs on phosphorus and nitrogen co-doped carbon black had 2.32% H_2O_2 production, while the traditional Pt/C catalyst showed an H_2O_2 yield of 4.58%.[117] Thus, the incorporation of heteroatoms into the carbon can help extend the overall lifetime of PEMFCs.

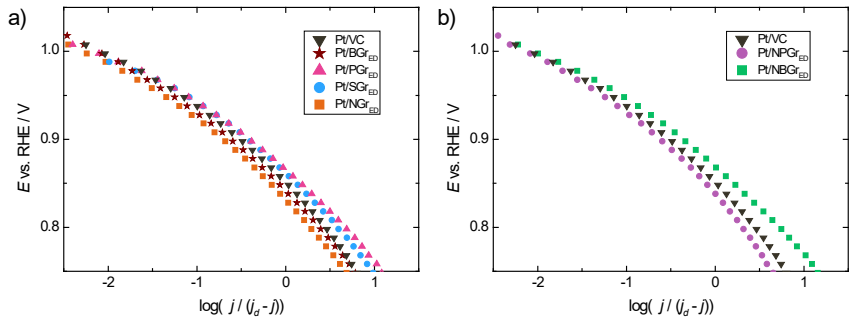

Figure 6. Tafel plots for O_2 reduction on a) electrochemically deposited PtNPs supported on single heteroatom-doped graphene and b) electrochemically deposited PtNPs supported on dual heteroatom-doped graphene in O_2-saturated 0.1 M $HClO_4$ solution at 1900 rpm. Data derived from Figure 4.

The Tafel plots for the synthesized catalysts are shown in Figure 6. The Tafel slopes (Table 1) for all synthesized catalysts were found to be close to -60 mV. Thus, the transfer of the first electron to the O_2 molecule was found to be the rate-determining step for all catalysts, confirming that the catalyst material behaves as expected.[111,118,119] The Tafel slope depends on the transfer coefficient and the coverage of oxygen-containing species on the electrode surface. The difference in surface coverage at different potentials causes a change in the Tafel slope from -60 to -120 mV.[120] These values are not cardinal numbers, and some deviations due to experimental conditions are expected. Tafel slope values derived from K-L plots can also depend on the electrode used in the experiment, as they assume complete subtraction of the mass-transfer-limited currents; rough electrode surfaces can cause deviations from this assumption.[120]

The SA of the ORR of the catalyst materials was determined at 0.9 V using Eq. 16:

$$SA = \frac{i_k}{ECSA} \tag{16}$$

where i_k represents the kinetic current at a specific potential; the ECSA of Pt was calculated by the charge integration of the hydrogen desorption peak (Table 1). The Pt deposited on boron-doped graphene had the highest SA of 1.26 mA cm^{-2}, followed by Pt/PGr_{ED} (1.21 mA cm^{-2}), Pt/SGr_{ED} (1.06 mA cm^{-2}), Pt/$NBGr_{ED}$ (0.99 mA cm^{-2}), Pt/NGr_{ED} (0.88 mA cm^{-2}), Pt/VC (0.87 mA cm^{-2}), and Pt/$NPGr_{ED}$ (0.79 mA cm^{-2}). The changes in the SA can be attributed to the effects of the heteroatom dopants in the carbon support had on the Pt. The heteroatom dopants all affect the binding energy of the PtNPs, which in turn affects the adsorption strength of the O_2 to the Pt and the overall electrocatalytic activity of the PtNPs.[68,121] The effect that the dopant has on the overall electrocatalytic activity of the PtNPs is dependent on whether it is electron-withdrawing, such as B, or electron-donating, such as N. When B is used as a dopant, the number of coordination

electrons increases, and the bond is primarily with the Pt.[96,97] This is in contrast to when N is used as the dopant and the number of coordination electrons is reduced and the bonding is primarily resulting from lone pair electrons.[122] The difference in donations of the electrons in the electrocatalytic system shifts the d-band center of the PtNPs, changes the electroneutrality of the carbon atoms, and thereby affects the chemical bonding of the PtNPs onto the substrate.[123,124] This could help to explain why Pt/BGr_{ED} exhibited the highest SA and Pt/NGr_{ED} had one of the lowest. When the support is doped with dual heteroatoms, the dopants exhibit a synergistic effect that affects the PtNP electron density.[125]

Table 1. Pt particle size, ECSA, and kinetic parameters for ORR on Pt/NGr_{ED}, Pt/SGr_{ED}, Pt/PGr_{ED}, Pt/BGr_{ED}, Pt/$NBGr_{ED}$, Pt/$NPGr_{ED}$, and Pt/VC catalysts in 0.1 M $HClO_4$ solution.

Catalyst	Particle size (nm)	ECSA (cm^2)	$E_{1/2}$ (V)	Tafel slope ($mV\ dec^{-1}$)	SA @ 0.9 V ($mA\ cm^{-2}$)
Pt/NGr_{ED}	16.4 ± 5.8	0.36 ± 0.01	0.84 ± 0.01	-59 ± 1	0.88 ± 0.19
Pt/SGr_{ED}	17.0 ± 7.9	0.38 ± 0.01	0.86 ± 0.01	-60 ± 1	1.06 ± 0.05
Pt/PGr_{ED}	12.8 ± 4.2	0.40 ± 0.04	0.86 ± 0.01	-59 ± 1	1.21 ± 0.12
Pt/BGr_{ED}	16.2 ± 5.5	0.28 ± 0.02	0.85 ± 0.01	-62 ± 1	1.26 ± 0.08
Pt/$NBGr_{ED}$	16.9 ± 6.8	0.54 ± 0.06	0.87 ± 0.01	-60 ± 1	0.99 ± 0.06
Pt/$NPGr_{ED}$	16.6 ± 6.1	0.43 ± 0.01	0.84± 0.01	-62 ± 1	0.79 ± 0.13
Pt/VC	-	0.46 ± 0.01	0.85 ± 0.01	-58 ± 1	0.87 ± 0.08

6.1.4 ADT of electrochemically deposited PtNPs on heteroatom-doped graphene

Accelerated durability testing (ADT) was carried out on Pt/NGr_{ED}, Pt/BGr_{ED}, Pt/$NBGr_{ED}$, and Pt/VC and shown in Figure 7. These were selected on the premise of Pt/$NBGr_{ED}$ being the most active electrocatalyst. As NBGr is a dual-hetero-atom-doped support, the single-heteroatom-doped support was also tested. Pt/$NBGr_{ED}$ showed the lowest ECSA loss of 8.7% followed by Pt/BGr_{ED} at 26%, Pt/VC at 27%, and Pt/NGr_{ED} at 53%. However, the loss in $E_{1/2}$ follows a different trend: Pt/VC and Pt/$NBGr_{ED}$ showed the least loss at a 50 mV drop in activity, followed by Pt/NGr_{ED} with a 60 mV loss, and then Pt/BGr_{ED} with an 80 mV loss. From the ADT results, it is clear that the synergetic effect of the dual heteroatom dopants plays a significant role in the durability of the electrocatalyst. This could suggest that the decrease of the adsorption intermediates from the B dopant and the pseudo barrier afforded from the N dopant work together.[68,126]

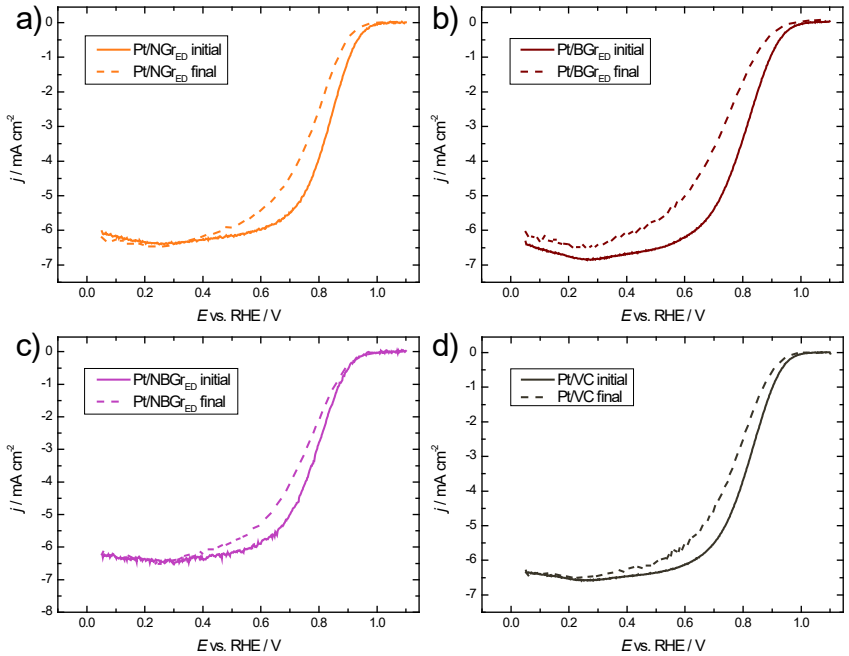

Figure 7. RDE polarization curves for ORR recorded before and after ADT on a) Pt/NGr$_{ED}$, b) Pt/BGr$_{ED}$, c) Pt/NBGr$_{ED}$, and d) Pt/VC catalysts at 1900 rpm in O_2-saturated 0.1 M $HClO_4$ solution.

6.2 The ORR on chemically deposited PtNPs supported on heteroatom-doped graphene

6.2.1 Surface morphology of chemically deposited PtNPs on heteroatom-doped graphene

The elemental composition of NGr, SGr, PGr, NSGr, and NPGr was confirmed through XPS (Figure 8). All five commercially available doped graphenes showed a strong C 1s peak at 284 eV. The NGr, NSGr, and NPGr materials had a N 1s peak at 389.3 eV.[105] The SGr and NSGr samples had a S 2p peak at 163 eV. The PGr and NPGr samples had a P 2p peak at 133 eV. All electro-catalysts had Pt 4f peaks at 71.1 and 74.3 eV. Thus confirming the elemental composition of the commercially available graphene and the deposition of PtNPs.[75,104–108]

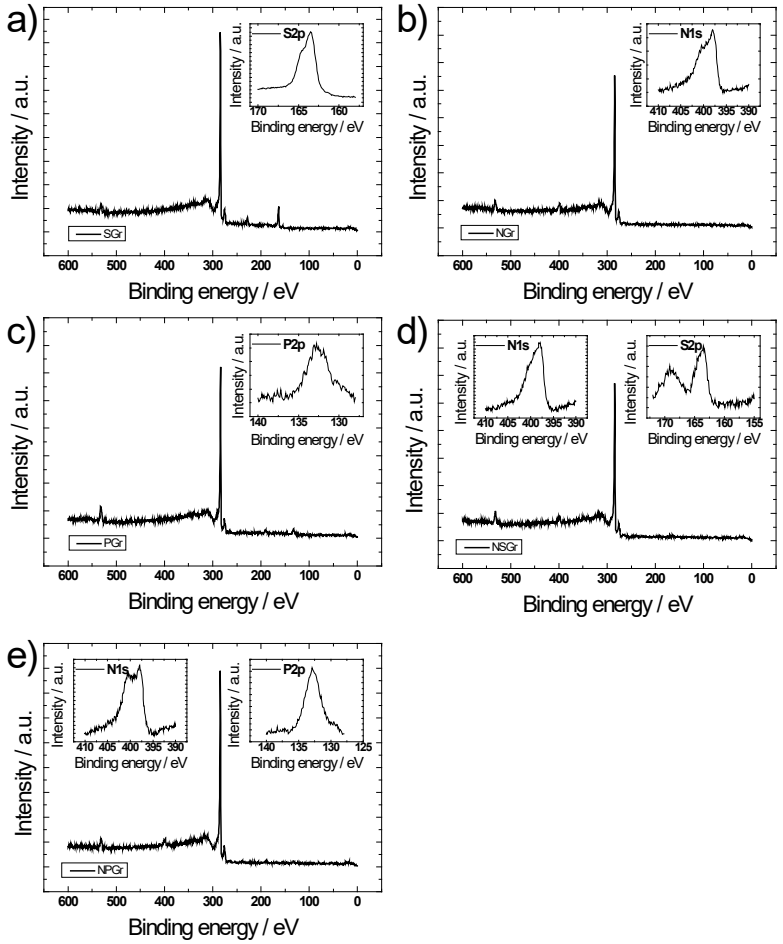

Figure 8. High resolution XPS survey spectra for a) SGr, b) NGr, c) PGr, d) NSGr, and e) NPGr samples. Inserts: high resolution XPS spectra in different regions.

Raman spectroscopy was used to analyze the structural disorder of the doped graphene supports. Figure 9 shows the first-order Raman spectra of the used materials, normalized to the intensity of the G band. All spectra were fitted following the five Voigt-shaped band model, where the G band (~1585 cm^{-1}) corresponds to the stretching vibrations of the sp^2 carbon atoms in the ideal graphitic lattice; D1 (~1350 cm^{-1}) to defect-activated breathing mode of aromatic rings; D2 (~1610 cm^{-1}) to disordered graphene layers at the surface of a graphitic crystal; D3 (~1490 cm^{-1}) to amorphous carbon and D4 (~1210 cm^{-1}) to disordered graphitic lattice.[127] It is important to note that the commonly used I_{D1}/I_G Raman band ratio is appropriate to quantify the structural imperfection for the graphene samples. However, in highly disordered carbon materials, the Raman band labeled as G is a superposition of the G and D2 bands. This band overlap renders the I_{D1}/I_G ratio an unreliable indicator of structural disorder in such

materials. The widths of the G and especially D1 bands provide indications of structural disorder in defective carbon materials.[128,129] However, the width of the G band cannot be used as a reliable measure of imperfection because it is impossible to separate the G and D2 bands, therefore in the fitting procedure, a composed (G+D2) band was used. To interpret the degree of structural disordering in used materials, the parameter W (full width at half-maximum of the D1 and G+D2 bands) and I_{D1}/I_{G+D2} (the ratio of the areas under the bands) were calculated as shown in Table 2. The data listed in Table 2 demonstrate that structural disorder is minimal in P-doped graphene and increases in the following order: NP-doped, NS-doped, N-doped, and S-doped graphene samples. Thus, the doped nature of the graphene powders was verified prior to the attachment of the PtNPs, and no undesirable elements were found.

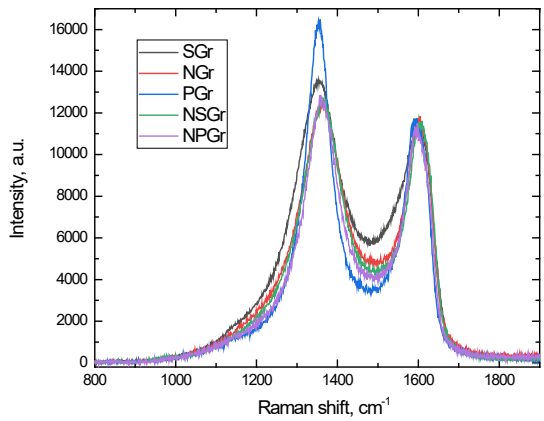

Figure 9. Raman spectra of SGr, NGr, PGr, NSGr, and NPGr samples.

Table 2. The value of I_{D1}/I_{G+D2}, W_{D1}, and W_{G+D2} calculated from the deconvolution of Raman bands for used heteroatom-doped graphene materials.

Catalyst Support	I_{D1}/I_{G+D2}	W_{D1}, cm^{-1}	W_{G+D2}, cm^{-1}
SGr	2.24	135	86
NGr	2.47	132	73
PGr	2.03	86	77
NSGr	2.49	126	78
NPGr	2.04	109	81

The physicochemical characterizations such as the particle size, particle distribution, and the elemental mappings of the PtNPs supported on the different heteroatom-doped graphene materials were analyzed using STEM (Figure 10), STEM-EDS (Figure 11) and XRF. The STEM images (Figure 10), confirm that PtNPs are present in all the catalyst materials and are uniformly distributed on the graphene flakes. Yet some agglomerations of PtNPs were still present; noticeably on Pt/SGr_{CD} (Figure 10a), Pt/NGr_{CD} (Figure 10b), and Pt/$NPGr_{CD}$ (Figure 10e) electrocatalysts. The STEM images also show that the dispersion of the PtNPs on the substrate varies with the support material. This could be due to a pH change during the chemical synthesis procedure used to attach the PtNPs to the support material. Therefore, it can be concluded that a similarity of charges led to a smaller dispersion and ultimately lower ECSA values (Table 3) for the materials in which the pH had to be altered to induce attachment of the PtNPs (Pt/PGr_{CD}, Pt/$NSGr_{CD}$). As Li et al. found, when the sodium citrate chemical deposition procedure is used in highly acidic solutions, the additional protons in the solution repel the carbon substrate, thereby hindering the attachment of the PtNPs.[130] ImageJ software was used to analyze the STEM images; the Pt particle sizes were: Pt/NGr_{CD} (4.72 nm), Pt/SGr_{CD} (4.70 nm), Pt/$NSGr_{CD}$ (3.64 nm), Pt/$NPGr_{CD}$ (3.58 nm), and Pt/PGr_{CD} (3.53 nm). Using the sodium citrate synthesis method, López-Cudero et al. synthesized PtNPs around 2 nm in size,[37] while Mazzotta et al. synthesized Pt particles around 4 nm.[131] Thus, confirming that the PtNPs synthesized were in accordance with those prepared in the literature.

To determine the distribution of elements in the materials, STEM-EDS analysis was performed (Figure 11). The Pt signal is observed throughout the graphene flakes, as indicated by the Pt EDS mappings, confirming the uniform dispersion of platinum throughout the support material. The STEM-EDS study also demonstrated phosphorus in the Pt/PGr_{CD} and Pt/$NPGr_{CD}$ samples, nitrogen in the Pt/$NSGr_{CD}$ and Pt/$NPGr_{CD}$ samples, and sulfur in the Pt/SGr_{CD} and Pt/$NSGr_{CD}$ catalyst materials, consistent with the XPS results. Despite some signal variations that are related to the variation in the local thickness of the graphene flakes and the changes in the local average atomic number of the electron beam-exited volume, it can be seen that the heteroatom dopants are relatively uniformly distributed in the graphene flakes.

The content of Pt in the final catalysts was determined via XRF. The expected Pt content for all materials was 20 wt%. As seen in Table 3 the synthesized material had the following Pt content: 24 wt% Pt (Pt/SGr_{CD}), 30 wt% Pt (Pt/NGr_{CD}), 12 wt% Pt (Pt/PGr_{CD}), 26 wt% Pt (Pt/$NSGr_{CD}$), 20 wt% Pt (Pt/$NPGr_{CD}$) and 16 wt% Pt (Pt/C). All of which fall within the expected range. As shown, Pt/PGr_{CD} has the lowest Pt content. However, this could result from the similarity in charges, leading to an initial repulsion of the PtNPs from the support material.[130]

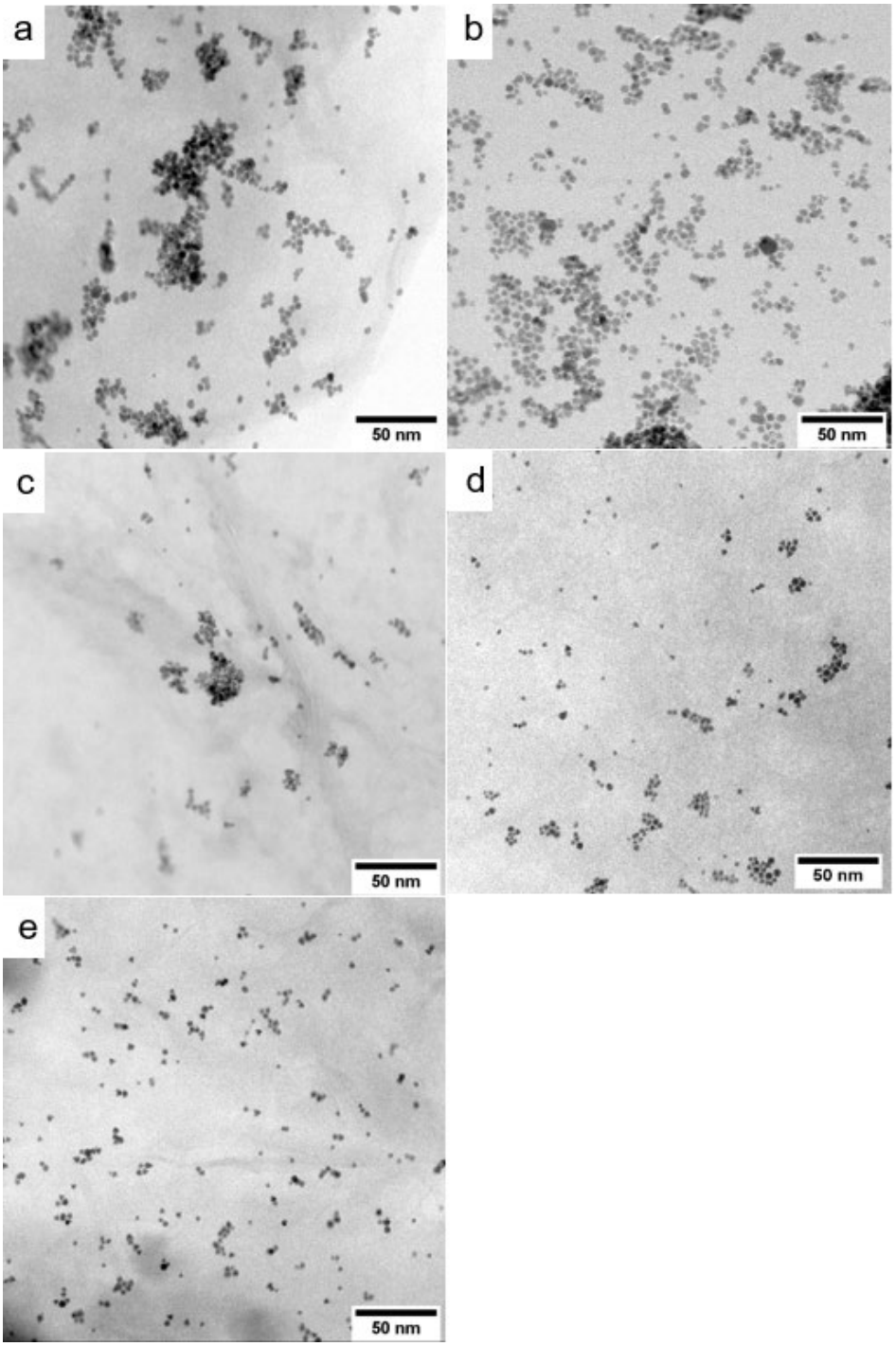

Figure 10. STEM images of a) Pt/SGr_{CD}, b) Pt/NGr_{CD}, c) Pt/PGr_{CD}, d) Pt/$NSGr_{CD}$, and e) Pt/$NPGr_{CD}$ samples.

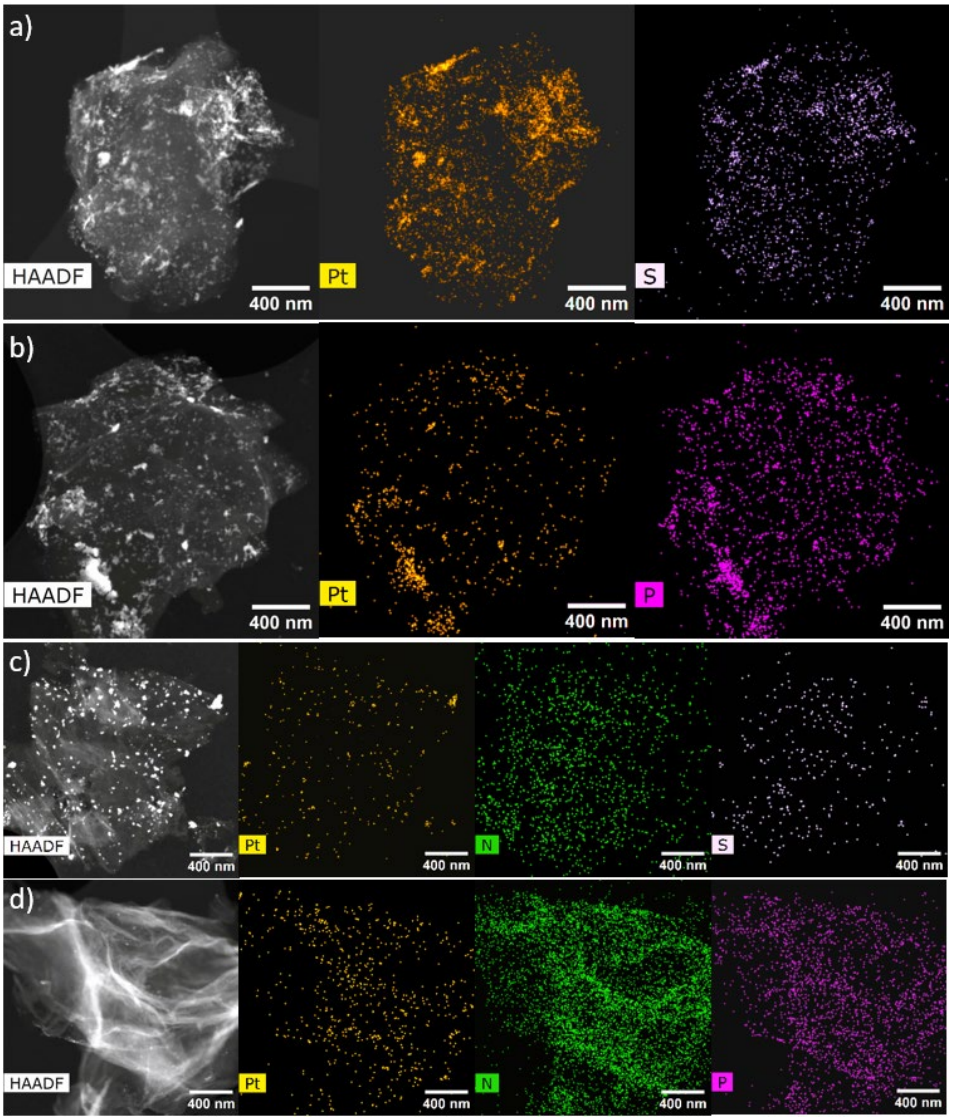

Figure 11. HAADF-STEM images and element mapping of a) Pt/SGr_{CD}, b) Pt/PGr_{CD}, c) $Pt/NSGr_{CD}$, and d) $Pt/NPGr_{CD}$ samples.

6.2.2 Electrochemical characterization of chemically deposited PtNPs on heteroatom-doped graphene

CO electro-oxidation was conducted in a 0.1 M $HClO_4$ solution saturated with Ar gas to clean the Pt catalyst surface without damaging the electrode surface.[132] The CO-oxidation profiles of the materials are depicted in Figure 13. Notably, all of the synthesized materials present CO-oxidation peaks containing multiplicities and oxidation that start at lower potentials than that of Pt/C. Pt/SGr_{CD} and

Pt/PGr$_{CD}$ catalysts have a broad oxidation peak immediately followed by a sharp narrow peak. Pt/NGr$_{CD}$ and Pt/NSGr$_{CD}$ catalysts have a peak with a broad shoulder, while Pt/NPGr$_{CD}$ has two peaks separated by a valley. These distinct features on the CO-stripping profiles could suggest that the different support materials result in PtNPs with different surface structures;[133] a shoulder indicative of PtNPs having more Pt(111) facets, and the PtNPs that have a multiplicity structure having more Pt(100) sites.[133] However, the exact position and the presence of a multiplicity could also be due to the catalyst and electrode preparation, the defects present in the PtNPs, the PtNPs' size, the amount of PtNP agglomerations, and/or the nature of the support material.[13]

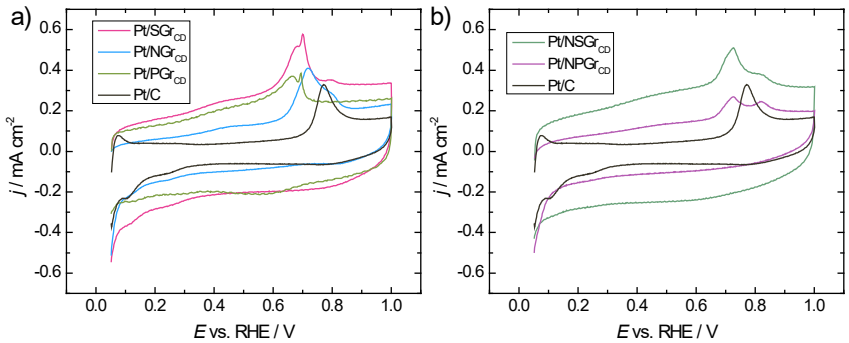

Figure 12. CO-stripping voltammograms of a) chemically deposited PtNPs supported on single heteroatom-doped graphenes and b) chemically deposited PtNPs supported on co-doped graphenes in Ar-saturated 0.1 M $HClO_4$ solution (v = 20 mV s^{-1}). The current densities are normalized to the geometric surface area of the electrode.

Cyclic voltammograms (Figure 13) were measured in Ar-saturated 0.1 M $HClO_4$ solution in a potential window of 0.05–1.45 V_{RHE} and a sweep rate of 50 mV s^{-1}. The presence of hydrogen adsorption/desorption peaks were observed within a potential range of 0.05–0.35 V_{RHE} and the presence of a Pt oxide reduction peak around 0.75 V_{RHE} was observed for all catalyst materials; thus confirming the expected CV behavior.[52,134–136] PtNPs on PGr$_{CD}$ and NSGr$_{CD}$ supports showed less pronounced H_{upd} and Pt oxide reduction peaks, resulting from lower Pt loadings on those supports. It can also be seen that the prepared catalysts exhibit different double-layer capacitances, suggesting that the structural differences of the support material influence their capacitance.[115] The electrochemical surface area of Pt was calculated by integrating the charge under the hydrogen desorption peaks with the assumption that 210 μC cm^{-2} is the charge density required for the desorption of a monolayer of hydrogen from the Pt surface.[9] The calculated ECSA values for all of the graphene-supported Pt catalysts are presented in Table 3. All of the synthesized catalysts had an ECSA value smaller than that of Pt/C (0.67 cm^2); the Pt/SGr$_{CD}$ had the highest ECSA (0.59 cm^2), and Pt/NSGr$_{CD}$ had the lowest ECSA (0.11 cm^2).

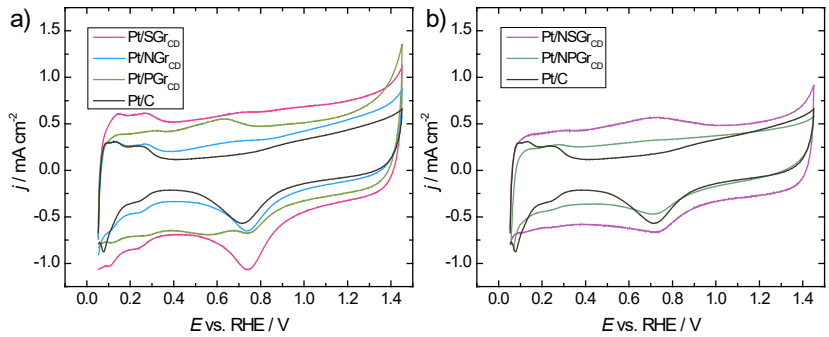

Figure 13. Comparison of CV curves of a) chemically deposited PtNPs supported on single heteroatom-doped graphenes and b) chemically deposited PtNPs supported on dual heteroatom-doped graphenes in Ar-saturated 0.1 M $HClO_4$ solution (v = 50 mV s^{-1}). The current densities are normalized to the geometric surface area of the electrode.

6.2.3 ORR on chemically deposited PtNPs on heteroatom-doped graphene

The ORR results at 1900 rpm are presented in Figure 14a for PtNPs deposited on single heteroatom-doped graphene and Figure 14b for dual heteroatom-doped graphene. Among the synthesized single heteroatom doped electrocatalysts both Pt/SGr$_{CD}$ and Pt/NGr$_{CD}$ exhibited a $E_{1/2}$ of 0.87 V vs. RHE, 20 mV higher than that of Pt/C ($E_{1/2}$ = 0.85 V). In contrast, only one dual heteroatom-doped graphene-supported Pt catalyst (Pt/NPGr$_{CD}$, $E_{1/2}$ = 0.86 V) demonstrated a larger half-wave potential than Pt/C. All of which is in agreement with previous literature, in which the doped carbon supports improved electrocatalytic activity of PtNPs for ORR.[108,137,138] Pt/PGr$_{CD}$ and Pt/NSGr$_{CD}$ catalysts possessed $E_{1/2}$ value of 0.82 V, which is lower than that of Pt/C. This contrasts with the PtNPs electrochemically deposited onto heteroatom doped graphene, which Pt/NP had the lowest $E_{1/2}$ of the synthesized catalyst (see Article [I]). During catalyst synthesis, challenges were encountered in attaching the PtNPs to P- and N,S-doped graphene. The observed impediments to the attachment of the PtNPs may contribute to their lower $E_{1/2}$ values as they are in contradiction to what is seen in the best results published in the literature.[73,76,139,140] Figure 15a shows the K–L plot for Pt/SGr$_{CD}$ with the n vs. E dependence as an inset. The K-L plot confirms that the ORR process on the catalyst material is mass transfer-limited in the current plateau region as the extrapolated trendline passes the origin. The linearity of the K-L plot further confirms that the ORR is a first-order reaction.[141] Using the K-L equation the number of electrons transferred during the ORR process was found to be close to 4 (Figure 15b). This value is consistent with other studies.[52,105,142,143] Thus, confirming that the ORR proceeds through a 4-electron pathway, which favors the formation of H_2O over H_2O_2.[4] The Tafel plots are shown in Figure 16. The Tafel slopes (Table 3) for all of the prepared catalysts are around -60 mV dec^{-1}. This confirms that the transfer of the first electron to the O_2 molecule is the rate-determining step.[120] It also confirms that the catalyst material behaves as anticipated.[105,143]

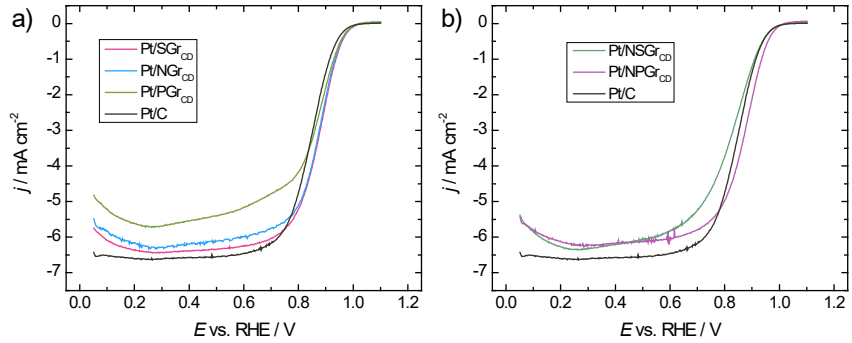

Figure 14. Comparison of ORR polarization curves for a) chemically deposited PtNPs supported on single heteroatom-doped graphenes and b) chemically deposited PtNPs supported on dual heteroatom-doped graphenes in O_2-saturated 0.1 M $HClO_4$ solution at 1900 rpm (v = 10 mV s^{-1}).

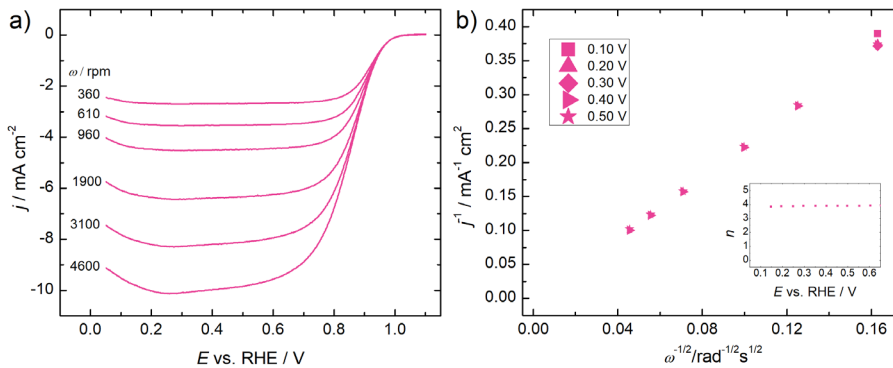

Figure 15. a) RDE polarization curves for ORR on Pt/SGr_{CD} in O_2-saturated 0.1 M $HClO_4$ (v = 10 mV s^{-1}). b) K-L plots derived from a). Inset shows the potential dependence of n.

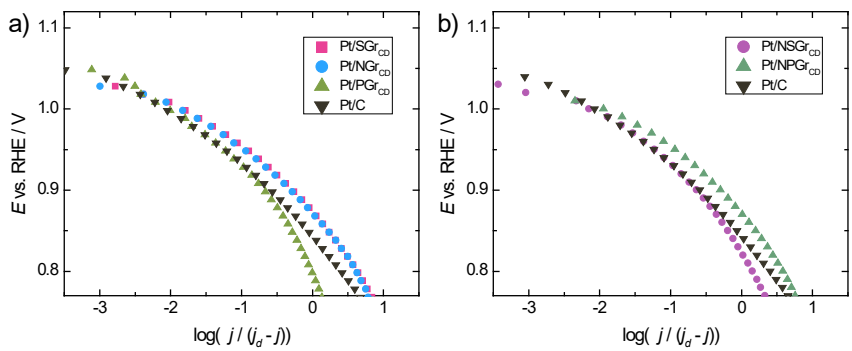

Figure 16. Tafel plots for O_2 reduction on a) chemically deposited PtNPs supported on single heteroatom-doped graphene and b) chemically deposited PtNPs supported on dual heteroatom-doped graphene in O_2-saturated 0.1 $HClO_4$ solution at 1900 rpm. Data derived from Figure 14.

Because the majority of the prepared catalysts exhibit half-wave potentials above 0.85 V, the catalyst's SA was determined at 0.9 V vs. RHE. The SA for the synthesized electrocatalysts is shown in Table 3. The Pt catalyst deposited on dual heteroatom-doped graphene materials had the highest SA value: Pt/NSGr$_{CD}$ (2.44 mA cm^{-2}) and Pt/NPGr$_{CD}$ (1.46 mA cm^{-2}). While the single heteroatom-doped graphene-supported Pt possessed the following SAs: Pt/PGr$_{CD}$ (1.44 mA cm^{-2}), Pt/NGr$_{CD}$ (1.10 mA cm^{-2}), and Pt/SGr$_{CD}$ (0.91 mA cm^{-2}). All Pt catalysts on heteroatom-doped graphene materials had a higher specific activity than the Pt/C catalyst (SA = 0.55 mA cm^{-2}). An increase in specific activity is an anticipated result of incorporating heteroatoms into graphene for use as a support for PtNPs.[144] The introduction of dopants can disrupt the electronic neutrality of graphene, thereby influencing the d-band center of Pt and enhancing its electrocatalytic activity.[145,146] The trend in SA differs from that reported in our previous publication (see section 6.1.), which showed that PtNPs supported on dual heteroatom-doped catalysts exhibit lower SA than those supported on single heteroatom-doped graphene. This difference could be due to the better attachment of the PtNPs to the support material resulting from their specific deposition procedure, the size and shape of the PtNPs or the difference in electrode preparation. As N was used in all the dual heteroatom-doped graphene supports, it can be assumed that the doping effect was enhanced by the synergistic effects of the other heteroatoms with nitrogen. As it is believed that nitrogen induces a superimposing positive effect.[147] This effect was explained by Groves et al., the addition of the nitrogen in the graphene lattice shifts the electron density, inducing a bond between the C and Pt; in undoped graphene, the Pt interacts with the delocalized double bond.[68,148] It is this bonding with the C atom rather than with the delocalized double bond that results in a bond with higher bonding energy, thus providing a more active material. An increase in specific activity was also observed by Cheng et al., who reported that the SA of Pt deposited on N-doped graphene was 93% higher than that of its undoped counterpart.[149] Hoque et al. also reported similar results with the SA of their Pt nanowires supported on S-doped graphene, increasing by 150% compared to those supported on non-doped graphene.[150] Similarly, Huang et al. saw an increase of SA when Pt was deposited on N,P dual heteroatom-doped carbon fiber frameworks.[151] Thus, confirming that by changing the support material in which the PtNPs are anchored, regardless of whether it is single heteroatom-doped or dual heteroatom-doped, has a positive effect on the overall ORR electrocatalytic activity. The impact of the support material was further proven by the PtNPs attached to phosphorus-doped carbon. Pt/C had a greater content of Pt (16 wt%) compared to Pt/PGr$_{CD}$ (12 wt%). However, the Pt/PGr$_{CD}$ had a significantly higher SA (2.44 mA cm^{-2}) than Pt/C (0.55 mA cm^{-2}). Thus, confirming that the specific activity is not dependent on the Pt content alone but is also a result of the doped support material providing a strong metal-support interaction. It is also interesting to note that the particles with the smallest size and highest specific activity were those for which the pH of the synthesis solution had to be adjusted to improve PtNP attachment to the doped graphene support. This difference in attachment styles due to the different

dopants further emphasizes the dopant's role in the nucleation of Pt on the support and thus its electrocatalytic activity.

Table 3. Pt content, particle size, ECSA, and kinetic parameters for ORR on Pt/SGr_{CD}, Pt/NGr_{CD}, Pt/PGr_{CD}, Pt/$NSGr_{CD}$, Pt/$NPGr_{CD}$, and Pt/C catalysts in 0.1 M $HClO_4$ solution.

Catalyst	Pt content (wt%)	Particle size (nm)	ECSA (cm^2)	$E_{1/2}$ (V)	Tafel slope (mV)	SA @ 0.9 V (mA cm^{-2})
Pt/SGr_{CD}	24 ± 2	4.70 ± 0.99	0.59 ± 0.01	0.87 ± 0.01	-61 ± 2	0.91 ± 0.11
Pt/NGr_{CD}	30 ± 1	4.72 ± 0.77	0.46 ± 0.03	0.87 ± 0.01	-61 ± 1	1.10 ± 0.07
Pt/PGr_{CD}	12 ± 1	3.53 ± 0.89	0.22 ± 0.01	0.82 ± 0.02	-59 ± 1	1.44 ± 0.02
Pt/$NSGr_{CD}$	26 ± 1	3.64 ± 1.12	0.11 ± 0.01	0.82 ± 0.01	-57 ± 1	2.44 ± 0.14
Pt/$NPGr_{CD}$	20 ± 3	3.56 ± 0.81	0.31 ± 0.01	0.86 ± 0.01	-63 ± 1	1.46 ± 0.02
Pt/C	16 ± 1	-	0.67 ± 0.06	0.85 ± 0.01	-61 ± 1	0.55 ± 0.04

6.2.4 ADT of chemically deposited PtNPs on heteroatom-doped graphene

PtNPs supported on nitrogen and sulfur dual heteroatom-doped graphene presented the highest specific activity. Therefore, these electrocatalysts were used to determine stability, as specific activity is a good indicator not only of the electrocatalytic activity of the material but also of the metal-support interaction.[152] The RDE polarization curves are shown in Figure 17 and correspond to 10,000 cycles over the potential range of 0.6–1.0 V_{RHE} at 100 mV s^{-1}. The Pt/$NSGr_{CD}$ catalyst did not show a change in $E_{1/2}$ (0.81 V), while the Pt/C showed a 10 mV drop from 0.84 to 0.83 V. This follows the same trend as reported by Bhaskaran et al. whose Pt/C dropped 9 mV after 5000 ADT cycles.[153] This increase in stability could be a result of the nitrogen dopant acting as a pseudo-barrier, slowing down the progression of PtNPs agglomeration.[68] The increase in stability could also be due to the use of graphene in the prepared catalyst, which is more corrosion-resistant.[118]

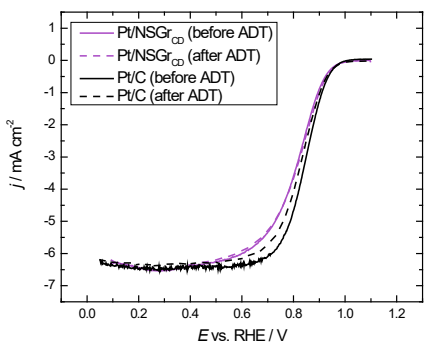

Figure 17. RDE polarization curves for ORR on Pt/$NSGr_{CD}$ and Pt/C catalysts recorded at 1900 rpm before and after ADT in O_2-saturated 0.1 M $HClO_4$ solution.

6.3 The ORR of PtNPs supported on nitrogen-doped porous carbon

6.3.1 Surface morphology of PtNPs on NC

For ionothermal synthesis, the precursor $Mg(NO_3)_2 \cdot 6H_2O$ was chosen due to its twofold action. Its low melting point of 88.9 °C, allows the formation of a molten salt phase before the onset of β-cyclodextrin carbonization. In addition, nitrate decomposition introduces nitrogen-containing moieties into the carbon material.[154] Using this carbonization method, mesopores in the catalyst support were generated in a stepwise manner. First, the macro- and mesopores are created through the liquid salt droplets during carbonization, and second, mesopores are created through the removal of the MgO template during the acid leaching.[154] From the N_2 adsorption isotherms, mesopores are indicated in the carbon support by the slopes at high relative pressure as observed in the inset of Figure 18a. The presence of micropores in the system is confirmed in the pore size distribution in Figure 18a. There is a higher amount of micropores in the Pt/NC-1pot catalyst as compared to the Pt/NC-2pot. This is further indicated in Table 4, in which the specific surface area (SSA) of micropores is 380 and 370 $m^2\ g^{-1}$ for Pt/NC-1pot and Pt/NC-2pot, respectively. This could indicate that the PtNPs synthesized by the 2-pot method are located on the surface of the carbon, outside the pores, and thus the micropores are being blocked by the PtNPs. Shen et al. concluded that the addition of PtNPs in both Vulcan carbon and Ketjen Black led to the complete disappearance of pores less than 2 nm.[57] The locality of the PtNPs is in part due to the high nominal loading value. For the synthesized catalysts, the SSA_{meso} is 760 and 529 $m^2\ g^{-1}$ for Pt/NC-1pot and Pt/NC-2pot, respectively. The presence of mesopores in the electrocatalytic system is important as these characteristics can mitigate some of the challenges arising from both micro- and macro-pores.[155] In that the mesopores in the carbon material can shield the PtNPs from the ionomer.[55,56] The XRD patterns of Pt/NC catalysts are shown in Figure 18b. From the XRD results it can be concluded that Pt/NC-1pot catalyst has a Pt crystallite size of 1.4 nm and a lattice parameter of 3.94 Å while Pt/NC-2pot has a Pt crystallite size of 1.9 nm and a lattice parameter of 3.93 Å.

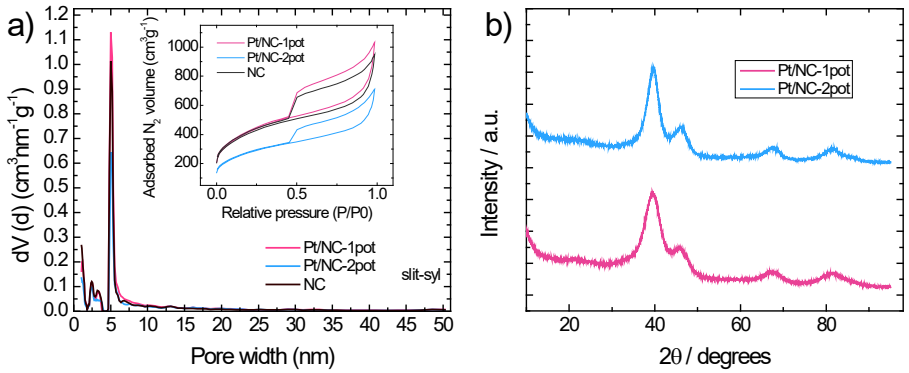

Figure 18. a) Pore size distribution of the synthesized catalyst. Inset: N_2 physisorption isotherms. b) XRD patterns of Pt/NC-1pot and Pt/NC-2pot catalysts.

Table 4. Specific surface area (SSA), microporous SSA (SSA_{μ}), mesoporous SSA (SSA_{meso}), and total pore volume of Pt/NC-1pot, Pt/NC-2pot, and NC catalysts.

Catalyst	SSA ($m^2\ g^{-1}$)	SSA_{μ} ($m^2\ g^{-1}$)	SSA_{meso} ($m^2\ g^{-1}$)	V_{tot} ($cm^3\ g^{-1}$)
Pt/NC-1pot	1140	380	760	1.24
Pt/NC-2pot	899	370	529	0.91
NC	1366	633	733	1.26

The porosity of the carbons is confirmed by the STEM images, as shown in Figure 19. The average PtNP size was analyzed through the ImageJ software and found to be 2.7 and 4.2 nm for Pt/NC-1pot and Pt/NC-2pot catalysts, respectively. This is in line with the results obtained by XRD. At this size, they can enter mesopores and achieve better PtNP dispersion[57] as the average mesopore width in both catalysts is around 5 nm and the average Pt particle size is less than that. The deposition procedure also appears to affect the PtNP agglomerations, as more agglomerations are evident in the Pt/NC-2pot than in the Pt/NC-1pot samples. The location of the PtNPs may result from using the sodium citrate method for deposition, as it has been shown to deposit PtNPs on the outer surfaces of pores.[156] Padgett et al. have shown that as the Pt loading increases, there is a greater tendency for PtNPs to deposit on the surface of the carbon support rather than in the pores.[157] The PtNP locality is further demonstrated in the HAADF-STEM images (Figure 20). The Pt/NC-1pot appears to have a greater number of pores in the structure in which the PtNPs could develop within, which are not present in Pt/NC-2pot.

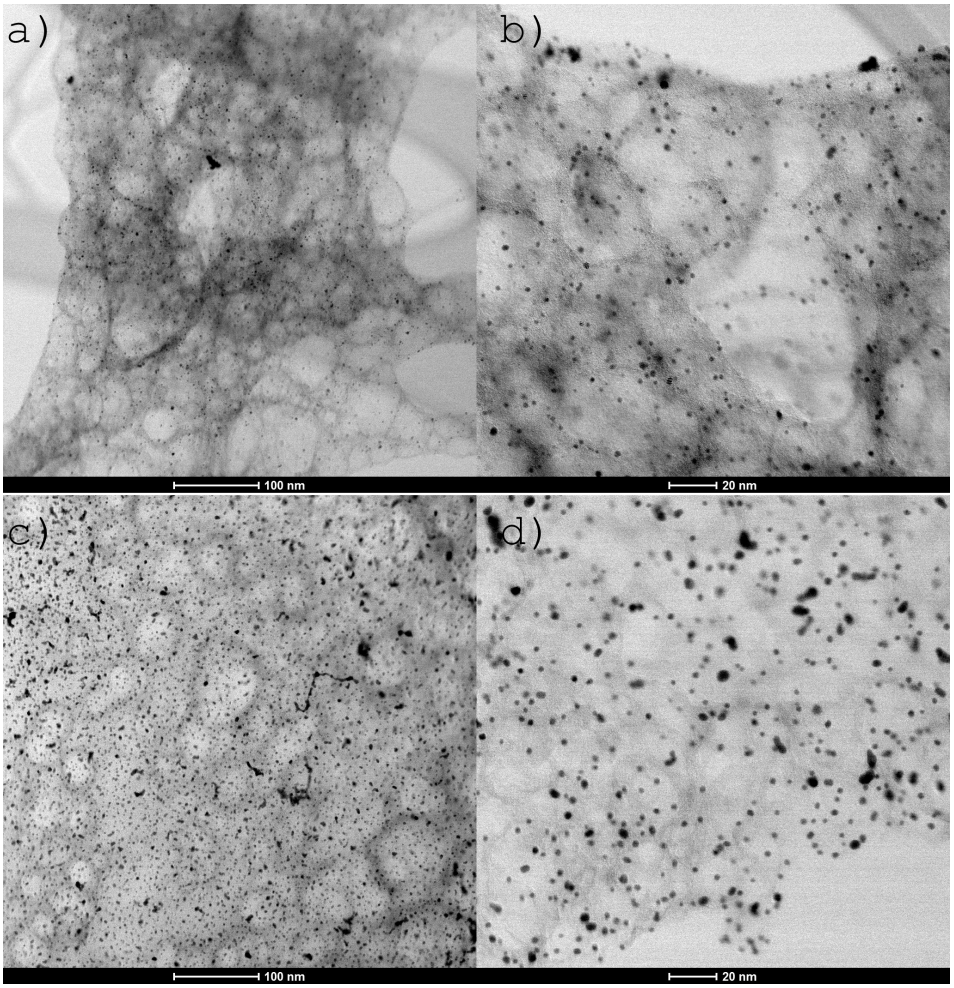

Figure 19. STEM images of a,b) Pt/NC-1pot and c,d) Pt/NC-2pot samples at different magnifications.

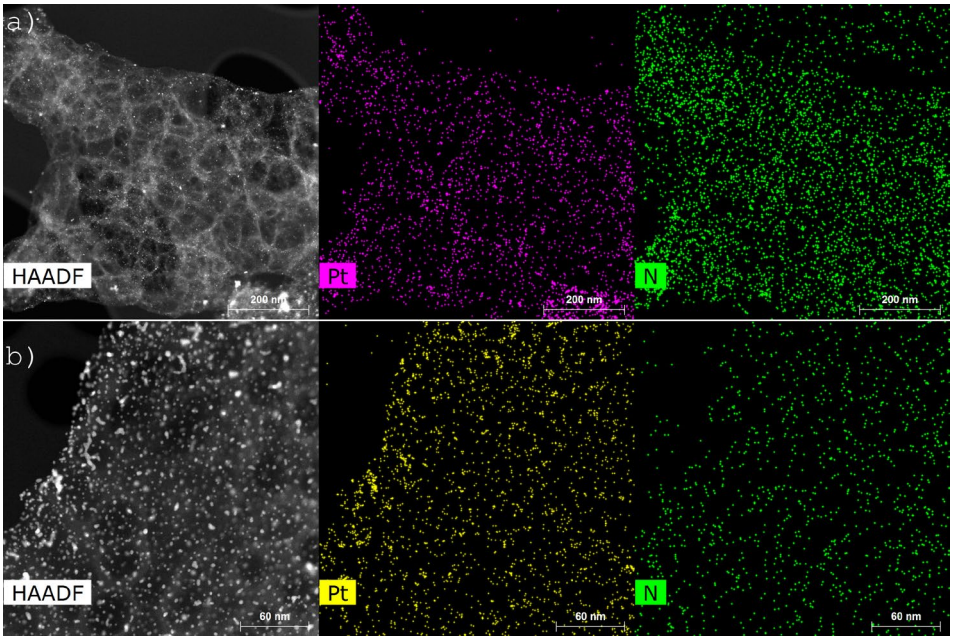

Figure 20. HAADF-STEM images and element maps of a) Pt/NC-1pot and b) Pt/NC-2pot.

The surface composition of catalyst materials was determined by XPS analysis (Figure 21). For both Pt/NC-1pot and Pt/NC-2pot materials, an intense carbon peak (C 1s) is observed at 284 eV. A nitrogen (N 1s) peak is present at 400 eV and a Pt 4f doublet at 71 and 75 eV is observed. The Pt 4f doublet is shifted more negative for the Pt/NC-2pot (74.5 and 71.2 eV) than the Pt/NC-1pot (74.8 and 71.5 eV), thus indicating a different metal support interaction for each catalyst. The XPS analysis aligns with the data published previously.[104,154,158] The carbon support used for the preparation of Pt/NC-1pot and Pt/NC-2pot electrocatalysts was previously analyzed by Ibrahim et al., and the different types of N species in the support material were reported.[103] In short, the samples contain the majority of pyridinic-N and graphitic-N. Pyridinic nitrogen is important because it can alter the electron density on the carbons.[65]

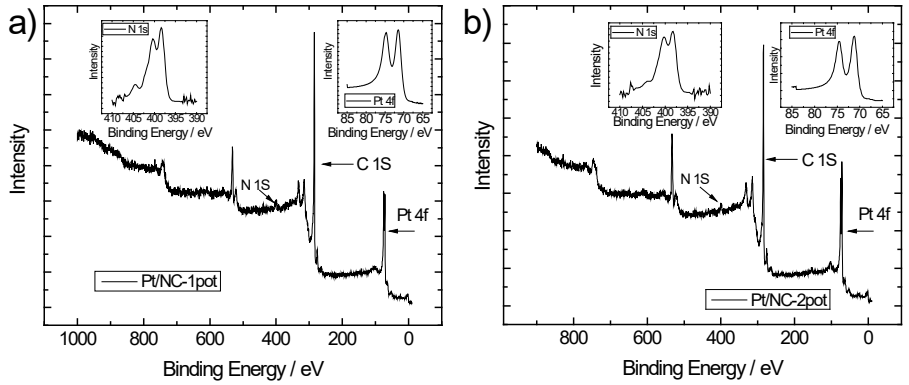

Figure 21. XPS survey spectra for a) Pt/NC-1pot and b) Pt/NC-2pot samples. Inserts: detailed XPS spectra in the Pt 4f and N 1s regions.

The Pt content in both Pt/NC-1pot and Pt/NC-2pot catalysts were determined by XRF analysis to be 40 and 37 wt%, respectively. From a synthesis route, the difference in Pt content, despite using the same synthesis method, could be a result of the varied pH of the colloidal system.[130] Li et al. found that when the colloidal PtNP synthesis method is highly dependent on the pH of the solution and varies based on the resulting zeta potential.[130]

6.3.2 Electrochemical characterization of PtNPs on NC

The CVs were run in a 0.1 M $HClO_4$ solution, that was saturated with Ar, in a potential range of 0.05–1.45 V_{RHE} at a scan rate of 50 mV s^{-1}. The presence of the Pt hydrogen adsorption/desorption peaks is visible in Figure 22a. However, the H_{upd} peaks are sharper and more defined in Pt/NC-1pot than in Pt/NC-2pot. Additionally, the Pt oxide reduction peak is broader and shifted to a more positive potential for Pt/NC-2pot (0.70 V) than it is for Pt/NC-1pot (0.63 V). This positive shift is indicative of OH_{ads} blocking the Pt catalyst sites for ORR.[104,158] The difference in the electrocatalytic ORR behavior between the two synthesized Pt/NC catalysts could also be ascribed to the localization of the PtNPs within the carbonaceous support and to the hydrophobicity of the different regions of the material, as the interior of the carbon pores are more hydrophobic than the exterior.[105] Additionally, there is also a difference in the EDLC. The Pt/NC-1pot catalyst has a higher EDLC than the Pt/NC-2pot and Pt/C catalysts. This could be due to the PtNPs being inside of the pores in the Pt/NC-1pot which allow for more of the carbon characteristic to show in the CV. The average Pt particle size for this catalyst was 2.7 nm, enabling PtNPs to be located in the pores and to exhibit more carbon-like characteristics in the CV. Based on the STEM images (Figure 19) and the shift in the oxide peak in the CV curves, it could indicate that PtNPs are located on the surface of Pt/NC-2pot rather than within its pores.

Prior to the RDE measurements, the catalysts underwent CO stripping (Figure 22b) to ensure the material was thoroughly cleaned and to further analyze the

effect of the support on the properties of PtNPs. The two synthesized Pt/NC catalysts exhibit a similar-shaped CO electro-oxidation peak at a more negative potential, 0.81 V (Pt/NC-1pot) and 0.82 V (Pt/NC-2pot), than that of Pt/C at 0.84 V. The broader peaks observed for the synthesized catalysts could indicate the presence of PtNP agglomerations.[37] The broad peaks could also indicate a wider range of PtNP sizes across the electrocatalysts.[159] The ECSA is shown in Table 5 and was 4.5, 0.9, and 9.5 cm^2 for Pt/NC-1pot, Pt/NC-2pot, and Pt/C, respectively. The low ECSA for Pt/NC-2pot is confirmed in both Figure 22a and Figure 22b, where the peaks for the synthesized catalyst are lower than those for Pt/NC-1pot and Pt/C. This contrasts with all three electrocatalysts having similar Pt wt%, suggesting that the Pt on Pt/NC-2pot is less accessible than that on the other catalysts.

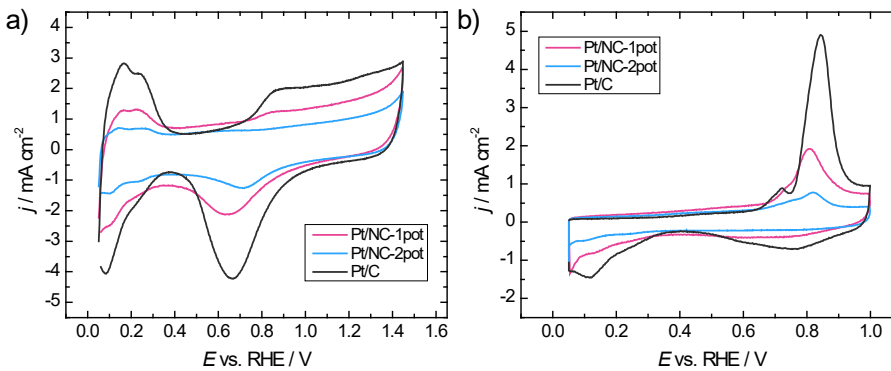

Figure 22. a) Comparison of CV curves of Pt/NC-1pot, Pt/NC-2pot, and Pt/C catalysts in Ar-saturated 0.1 M $HClO_4$ solution (v = 50 mV s^{-1}) and b) CO-stripping profiles of Pt/NC-1pot, Pt/NC-2pot, and Pt/C catalysts in Ar-saturated 0.1 M $HClO_4$ solution (v = 20 mV s^{-1}). The current densities are normalized to the geometric surface area of the GC electrode.

6.3.3 ORR studies of PtNPs on NC

The RDE polarization curves for Pt/NC-2pot at various electrode rotation rates are presented in Figure 23a. The $E_{1/2}$ values of the catalysts are 0.88, 0.87, and 0.92 V for Pt/NC-1pot, Pt/NC-2pot, and Pt/C, respectively. The differences in the half-wave potentials of the prepared catalysts may be due to variations in the locality of the PtNPs on the carbon support. As PtNPs within the pores have a higher activity than those located on the outside of the carbon support; the inclusion of pores can enhance the oxygen diffusion.[96] Thus, confirming that the locality of the PtNPs has an important role in the determination of the electrocatalytic activity of the catalyst. The diffusion-limited current density for the 4-electron ORR process is reached in both prepared Pt/NC catalysts. Thus, confirming the typical Pt electrocatalytic behavior in RDE tests.

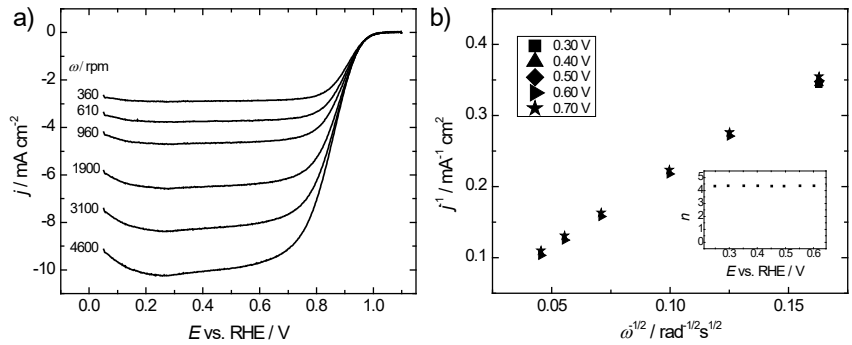

Figure 23. a) RDE polarization curves for ORR on a Pt/NC-2pot catalyst in O_2-saturated 0.1 M $HClO_4$ at various electrode rotation rates (v = 10 mV s^{-1}) and b) K–L plots derived from a). Inset shows the potential dependence of n.

The K-L plot for Pt/NC-2pot is shown in Figure 23b. Both catalysts followed similar trends. The K-L plots for both catalysts further confirm that, over the broad potential range the ORR process is mass-transfer limited, as the extrapolated trendline passes through the origin. This also indicated that the reaction follows first-order kinetics with respect to the O_2 concentration.[141] The inset in Figure 23b confirms that both catalysts follow a four-electron ORR pathway. This is the preferred pathway over the 2-electron pathway, as the latter produces a peroxide intermediate and results in lower fuel cell efficiency.[160] The Tafel plots are presented in Figure 24b for Pt/NC-1pot, Pt/NC-2pot, and Pt/C catalysts. The synthesized catalysts exhibit a Tafel slope of approximately -60 mV, indicating that the transfer of the first electron to O_2 is the rate-determining step in the ORR.[120] This is similar to other PtNPs supported on nanocarbons.[119]

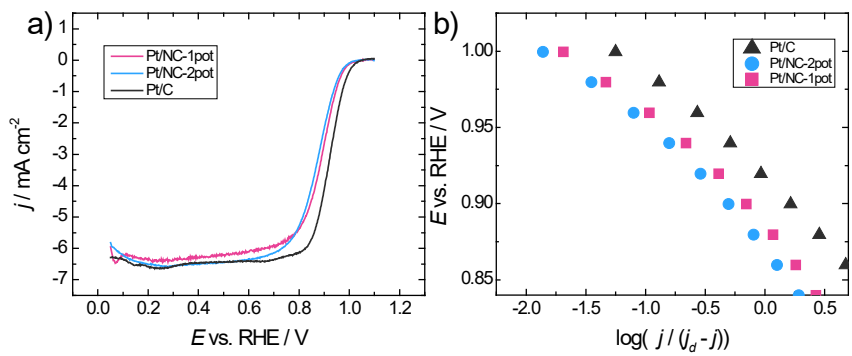

Figure 24. a) Comparison of the ORR polarization curves and b) Tafel plots derived from a) for Pt/NC-1pot, Pt/NC-2pot, and Pt/C catalysts in O_2-saturated 0.1 M $HClO_4$ solution at 1900 rpm (v = 10 mV s^{-1}).

The SA for ORR on Pt/NC-1pot, Pt/NC-2pot, and Pt/C electrocatalysts were calculated at 0.9 V vs. RHE, with ECSA determined from integration of the CO-stripping profile, as shown in Table 5. The specific activities for Pt/NC-1pot, Pt/NC-2pot, and Pt/C are 0.25, 0.51, and 0.25 mA cm^{-2}, respectively. Wang et al. found that PtNPs located on mesoporous carbons have a higher count of Pt active sites compared to conventional catalytic layers.[96] The differences among the electrocatalysts could result from the PtNPs' locality on the carbon support, as O_2 concentration varies across locations.[96] Additionally, Ferro et al. studied the effect of the locality of PtNPs on porous carbons and found that the PtNPs located within the mesopores had a higher mass activity than the PtNPs located outside of the pores.[156] The difference in specific activity could also be due to particle size. Inaba found that the SA of PtNPs at 1.8 nm decreased by 190% compared to those at 3.9 nm.[21] Thus, the Pt/NC-2pot catalyst could have a more optimized particle size of 4.2 nm as compared to the smaller nanoparticles of the Pt/NC-1pot material.

Table 5. Pt content, ECSA, and kinetic parameters for ORR of Pt/NC-1pot, Pt/NC-2pot, and Pt/C catalysts in 0.1 M $HClO_4$ solution.

Catalyst	Pt content (wt%)	ECSA (cm^2)	$E_{1/2}$ (V)	Tafel slope (mV)	SA @ 0.9 V (mA cm^{-2})
Pt/NC-1pot	40	4.5 ± 0.43	0.88 ± 0.01	-58 ± 2	0.25 ± 0.01
Pt/NC-2pot	37	0.9 ± 0.24	0.87 ± 0.01	-58 ± 2	0.51 ± 0.03
Pt/C	46	9.5 ± 0.49	0.92 ± 0.01	-61 ± 1	0.25 ± 0.04

6.3.4 Accelerated durability testing of PtNPs on NC

The synthesized Pt/NC catalysts underwent accelerated durability testing by undergoing 45,000 scans in the potential window of 0.05–1.2 V_{RHE} with a scan rate of 500 mV s^{-1}. The results of the ADT are presented in Figure 25a–c. In both Pt/NC-1pot and Pt/NC-2pot, an increased double-layer capacitance is observed in the CVs as presented in Figure 25d–f. This observed change in the synthesized carbon material characteristics could be a result of the wettability of the carbon, as the oxygen-containing groups on the carbon surface provide a pseudocapacitance.[114] As the ADT progresses, the oxygen concentration around the pores changes.[161] The presence of the quinone/hydroquinone peak at 0.6 V is further indicative of the oxidation of the carbon support occurring throughout the stability testing.[105] After 45,000 scans, a change in the hydrogen adsorption/desorption region is present for all catalysts. This region of the Pt/NC-1pot catalyst is relatively unchanged, whereas the Pt/NC-2pot material shows a major decrease, indicating an ECSA loss, which for Pt/NC-1pot catalyst decreased by 19%, for Pt/NC-2pot by 33%, and for Pt/C decreased the most – by 37%. The smaller change in the ECSA of the Pt/NC-1pot catalyst could be a result of the PtNP

located within the carbon support, due in part to the different chemical deposition procedures used. The change in ECSA could also be due to Ostwald ripening occurring at different rates among the different electrocatalysts. The larger drop in ECSA of the Pt/NC-2pot as compared to the Pt/NC-1pot could also indicate the detachment of the PtNPs from the Pt/NC-2pot catalyst due in part to the nucleation of the PtNPs prior to the addition of the carbon support in the chemical deposition procedure. Additionally, after 45,000 cycles, the ORR half-wave potential of the Pt/C catalyst decreased by 20 mV, whereas for Pt/NC-1pot and Pt/NC-2pot it decreased by 20 and 100 mV, respectively. The lower loss of ECSA of the Pt/NC catalysts could be due to N-doping, which reduces the adsorption of oxygen-containing species on PtNPs.[162] This could be due to a higher oxidation state of the PtNPs, resulting from electron transfer from Pt to nitrogen, which decreases the adsorption strength of oxygenated species on the PtNPs.[162] Fu et al. reported similar stability results with a PtCu catalyst supported on an one-dimensional hierarchical mesoporous nanostructure compared to Pt/C; after 5000 cycles of ADT, their material lost 18% of its original ECSA, while Pt/C lost 54%.[163] Further, the increased stability could be a result of the confinement of PtNPs inside the carbon pores, which could mitigate PtNP agglomeration.[57,58]

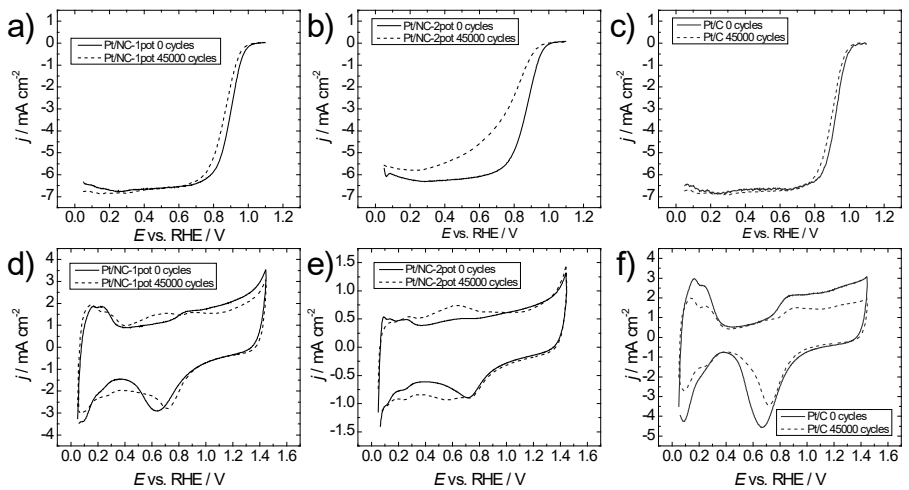

Figure 25. RDE polarization curves for the ORR on a) Pt/NC-1pot, b) Pt/NC-2pot, and c) Pt/C catalysts at 1900 rpm before and after ADT in O_2-saturated 0.1 M $HClO_4$ solution (v = 10 mV s^{-1}). CVs for d) Pt/NC-1pot, e) Pt/NC-2pot, and f) Pt/C catalysts before and after ADT in Ar-saturated 0.1 M $HClO_4$ solution (v = 50 mV s^{-1}). The current densities are normalized to the geometric surface area of the GC electrode.

6.3.5 Single-cell fuel cell test of PtNPs supported on NC

The synthesized Pt/NC catalysts were further tested in a single-cell PEMFC. The Pt/NC-1pot and the Pt/NC-2pot cathodes showed P_{max} of 274 and 180 mW cm^{-2}, respectively. The current densities for the synthesized catalysts were recorded at

0.8 V and were 106 and 54 mA cm^{-2} for Pt/NC-1pot and Pt/NC-2pot cathodes, respectively. Both the polarization curves and power density curves are shown in Figure 26. These results are similar to those reported by Arici et al., who studied PtNPs supported on graphene nanoplatelets, composite graphene nanoplatelets, and carbon black, and reported P_{max} of 247 and 377 mW cm^{-2}, respectively.[99] The Pt/NC-1pot catalyst showed improved PEMFC performance compared to the Pt/NC-2pot catalyst. This could be a result of smaller particle sizes, which, in turn, allow for more Pt active sites throughout the catalyst as has been reported previously.[161] The I/C ratio chosen to test the synthesized catalysts was 8. This was due to the nature of the low-density carbon support. The high I/C ratio enabled good adhesion of catalysts to the Nafion membrane. It is well known that too high I/C ratio can impede the electrocatalytic activity of the catalyst, due to the impedance of the O_2 diffusion across the catalyst layer.[96] However, the overall surface morphology of the carbon support is another factor, as Ignaszak et al. found that the optimal Nafion loading depends on the support morphology.[97] This point is further discussed by You et al., who noted that the pores within the carbon support can help prevent ionomer poisoning of the PtNPs as the solvent within the pores can block the ionomer from entering.[155] Additionally, doping nitrogen into the carbon support further improves the overall PEMFC performance. One way in which the nitrogen has an influence is through allowing for a uniform dispersion of PtNPs throughout the entirety of the catalyst.[164] Uniform Pt dispersion ensures uniform activity throughout the MEA. Xiong et al. further confirmed the importance of nitrogen doping both theoretically and experimentally; in PEMFC, the N-doped catalyst showed higher P_{max} than the undoped catalyst.[165] Additionally, by DFT calculations, they observed that the repulsion forces acting on the PtNPs decrease. The doping of nitrogen into the support could further lead to better ionomer distribution throughout the electrocatalyst.[166] However, the addition of a nitrogen dopant is not the only factor; the N species present in the catalyst is of importance.[67,164] Hornberger et al. point out that pyridinic-N groups can possibly interact with the ionomer sulfonic groups and allow for better ionomer dispersion, which in turn improves the PEMFC performance.[67] The results obtained herein confirm that by precisely designing PtNPs and the carbon support, the electrocatalytic activity of the catalysts can be improved.

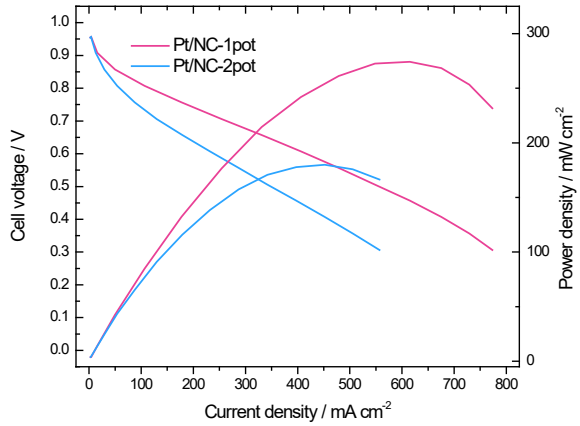

Figure 26. Polarization and power density curves for a H_2/O_2 PEMFC with the Nafion 211 proton exchange membrane, Pt/NC-1pot and Pt/NC-2pot cathodes (loading ~0.25 mg cm^{-2}), and Pt/C anode (~0.25 mg cm^{-2}). Backpressure 170 kPa and temperature 80 ºC.

6.4 The ORR of PtNPs supported on SnO_2-CNT

6.4.1 Surface morphology of PtNPs on SnO_2-CNT

XPS analysis was performed with the Pt/SnO_2–CNT catalyst to confirm its composition (Figure 27). An intense carbon peak (C 1s) is observed at 284 eV. A prominent oxygen peak (O 1s) originating from the carbon-oxygen groups on the CNTs and SnO_2 appeared at 540 eV. The presence of Sn was confirmed by the appearance of Sn 3d peaks at 485 and 495 eV. The presence of Pt was confirmed with the doublet of Pt 4f peaks at 71 and 75 eV. The peaks present in the sample are congruent with those found in literature.[97,104,158,167] In this sample, the most negative Pt 4f peak is centered at 71.2 eV, a negative shift relative to the Pt 4f peak reported by Li et al., which was 71.8 eV.[168] This negative shift indicates electron transfer between SnO_2 and Pt.[168] Electron transfer provides evidence of an electronic metal–support interaction, shifting the d-band center of Pt and enhancing the adsorption energy of O intermediates.[168] The Pt concentration on the electrode surface was analyzed by XPS and found to be 0.6 at%, whereas XRF analysis determined the Pt content to be 15 ± 3 wt%. The difference in values between XPS and XRF suggests a discrepancy between the platinum content within the bulk of the catalyst and its surface. The Pt mass determined by XRF was consistent with the EDS measurement, which indicated a Pt content of 13 ± 6% in the catalyst. The STEM-EDS element mapping (Figure 28b) confirms the uniform distribution of Sn on the CNTs. The STEM image (Figure 28a) of the PtNP/SnO_2–CNT catalyst further confirms the distribution of PtNPs throughout the sample. The Pt particle size was analyzed, yielding an average of 4.1 ± 1.5 nm. This is consistent with our previous studies that used the sodium citrate method to synthesize PtNPs [II, III].

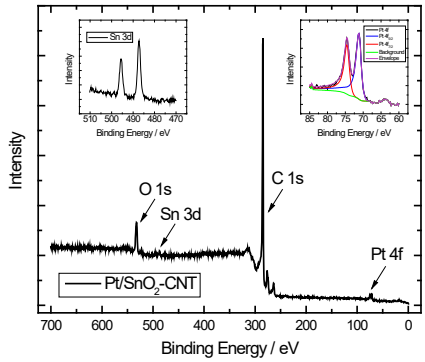

Figure 27. XPS survey spectra for Pt/SnO_2–CNT. Inserts: detailed XPS spectra in the Pt 4f and Sn 3d regions.

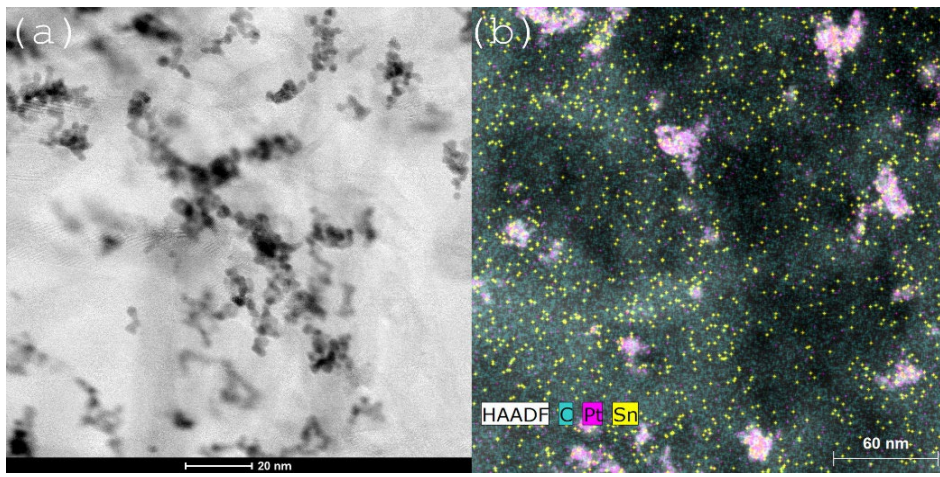

Figure 28. a) Bright-field STEM image and b) high-angle annular dark-field (HAADF) STEM image of a larger area with overlaid EDS elemental maps of C, Pt and Sn for the Pt/SnO_2–CNT sample.

6.4.2 Electrochemical characterization of PtNPs on SnO_2-CNT

Cyclic voltammograms of the catalyst materials were recorded over a potential range of 0.05–1.45 V_{RHE} at a scan rate of 50 mV s^{-1} in an Ar-saturated 0.1 M $HClO_4$ solution. The CVs are presented in Figure 29a, which compares Pt/SnO_2–CNT with Pt/C. The presence of the hydrogen adsorption and desorption peaks is observed in the potential window of 0.05–0.35 V_{RHE} [134] and the Pt oxide peak at 0.75 V_{RHE}.[134,135] The oxide peak is less pronounced on the Pt/SnO_2–CNT catalyst than on the commercial Pt/C catalyst, indicating SMSI between Pt and SnO_2. Both the synthesized and commercial catalysts exhibit a double peak in the hydrogen adsorption/desorption region, at approximately 0.15 and 0.23 V, indicating the presence of Pt(110) and Pt(100) crystal facets.[169] Additionally, the Pt/SnO_2–

CNT catalyst exhibits a small anodic peak at approximately 0.34 V, which is attributed to Pt (111) sites.[170] Gasteiger et al. reported a shift in the Pt oxide peaks between Pt/C (TKK), Pt/carbon black, and a pure Pt disk, and attributed the shift to OH_{ads} species blocking sites for ORR.[135] A more positive shift in the Pt oxide peak is an indicator for suppression of oxidized Pt.[85] Further, Spasov et al. showed that SnO_2 facilitates OH adsorption, therefore hindering adsorption of hydrogen onto the PtNPs.[171] The difference in the double-layer capacitance between Pt/SnO_2–CNT and Pt/C is due to the interactions that occur between the CNT_S and water.[169] This effect is enhanced with lower Pt loadings[172] and could also be due to the difference in the Pt d-band provided by electronic interactions.[168] The ECSA of the PtNPs was calculated through the integration of the charge under the hydrogen desorption peak, assuming that 210 μC cm^{-2} is the charge density required for the desorption of a monolayer of hydrogen from the Pt surface.[9] The calculated ECSA values for both Pt/SnO_2–CNT and Pt/C catalysts are presented in Table 6. Pt/SnO_2–CNT had an ECSA of 0.96 cm^2, while Pt/C had an ECSA of 4.7 cm^2. This is comparable to what has been found in the literature.[135,171,173,174] Sun et al. measured the ORR activity of Pt nanowires supported on tin oxide-coated CNTs in H_2SO_4 solution; the synthesized catalyst had 50% lower ECSA than the commercial Pt on carbon black.[174] Li et al. found similar results in that the total amount of PtNPs on SnO_2-decorated CNTs was lower than that on pristine CNTs.[168] The decreased loading of PtNPs could be due to the SMSI occurring between SnO_2 and CNTs, causing a difference in the attachment of the PtNPs.

The electro-oxidation of pre-adsorbed CO was conducted in an Ar-saturated 0.1 M $HClO_4$ solution, in a potential range of 0.05–1.0 V_{RHE} with a scan rate of 20 mV s^{-1}. The CO-stripping profiles for Pt/SnO_2–CNT and Pt/C are provided in Figure 29b. The difference in ECSA between Pt/SnO_2–CNT and Pt/C is also reflected in the height of the CO-stripping peak. Pt/SnO_2–CNT exhibits a broader, shallower CO-stripping profile compared to Pt/C, which shows two peaks: a smaller, sharp peak and a taller, sharp peak—these differences further indicate SMSI between the PtNPs and SnO_2. The shallower CO-stripping profile of the Pt/SnO_2–CNT catalyst could be due to a restriction of contact between the PtNPs and the CO molecules.[175] The prepared Pt/SnO_2–CNT catalyst has a CO-stripping profile that occurs at a lower potential than that of the commercial Pt/C. The shoulder formed at 0.3 – 0.7 V could be a result of the CO oxidation on the PtNPs adjacent to the Sn atoms as a result of electronic interaction.[176,177] This negative shift of the CO-stripping profile could be indicative of the bifunctional mechanism that occurs in response to the addition of SnO_2,[169] in that SnO_2 provides oxygen-containing species for the PtNPs in the proximity through the creation of oxygen vacancies, thus lowering the CO oxidation overpotential.[176,178] To a lesser extent, the difference of the CO-stripping profiles could also be a result of the different Pt facets on the catalyst.[133]

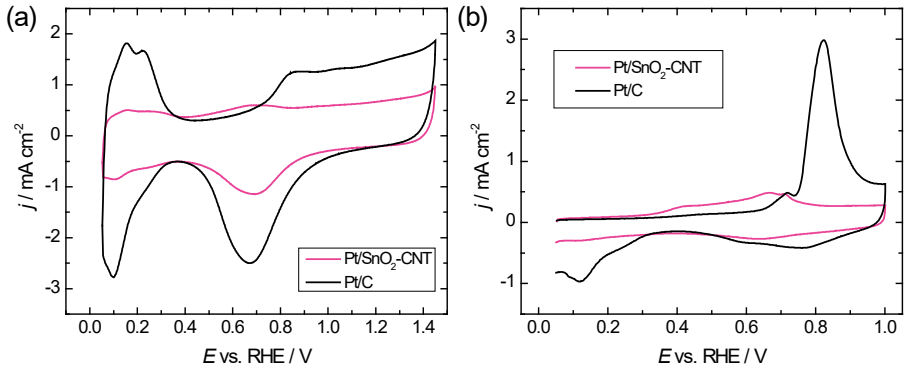

Figure 29. a) Comparison of CV curves of Pt/SnO_2–CNT and Pt/C in Ar-saturated 0.1 M $HClO_4$ solution (v = 50 mV s^{-1}) and b) CO-stripping voltammograms of Pt/SnO_2–CNT and Pt/C in Ar-saturated 0.1 M $HClO_4$ solution (v = 20 mV s^{-1}). The current densities are normalized to the geometric surface area of the electrode.

6.4.3 ORR studies of PtNPs on SnO_2-CNT

The ORR measurements were conducted in an O_2-saturated 0.1 M $HClO_4$ solution in a potential range of 0.05–1.1 V_{RHE} and a scan rate of 10 mV s^{-1}. Figure 30a presents the RDE polarization curve for Pt/SnO_2–CNT at various electrode rotation rates, where the diffusion-limited current density is constantly reached, thus further confirming typical Pt electrocatalytic behavior for a four-electron pathway of the ORR.[113] A slight decrease in current density is seen at the lower potentials. This could indicate the blocking of ORR-active sites by hydrogen adsorption.[112]

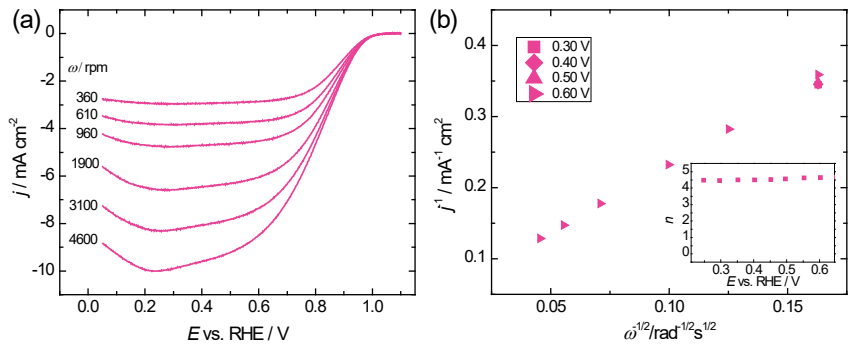

Figure 30. a) RDE polarization curves for the ORR on the Pt/SnO_2–CNT catalyst in O_2-saturated 0.1 M $HClO_4$ (v = 10 mV s^{-1}) and b) K–L plots derived from a). Inset shows the potential dependence of n.

Figure 31a shows a comparison of the Pt/SnO_2–CNT and the Pt/C catalysts at 1900 rpm. Pt/SnO_2–CNT shows an $E_{1/2}$ of 0.83 V, while Pt/C possesses an $E_{1/2}$ of 0.88 V. The 50 mV difference could be a result of SnO_2 blocking some of the reaction sites.[135] SnO_2 also affects the efficiency of the oxidation of Pt,[85] which could result in the lower $E_{1/2}$ compared to the commercial Pt/C. The effects on Pt due to the decoration of SnO_2 onto the CNTs are a result of the influence that SnO_2 has on the redistribution of the d-band center of Pt.[168] However, this effect can be mitigated through optimization of the d-band center, as there is an optimal relation between the ORR activity and the tuning of the d-band center.[168] These results are similar to those reported by Ruiz Camacho et al. ($E_{1/2}$ = 0.83 V) for Pt supported on SnO_2-decorated carbon.[179] Hussain et al. also found that PtNPs on tin oxide photo-deposited onto CNTs had a lower half-wave potential than Pt/C.[169] This is in opposition to a study by Jia et al., which explored PtNPs on tin oxide chemically deposited onto nitrogen-doped carbon that outperformed the Pt/C catalyst.[180] These results could also be due to the amount of SnO_2 in the electrocatalytic system, as Gu et al. and Li et al. both showed that there is an optimal relationship between the amount of SnO_2 and the reactivity of Pt toward the ORR.[168,181]

The K–L equation (Eq. 15) was used to analyze the ORR polarization data. Figure 30b shows the K–L plot for Pt/SnO_2–CNT, with an inset presenting the dependence of n vs. E. As the extrapolated trendline passes the origin of the K–L plot, it can be confirmed that the ORR process on the Pt/SnO_2–CNT catalyst is mass-transfer limited in a wide potential range; the K–L plot further confirms that the reaction follows a first-order kinetics toward O_2 concentration.[141] The ORR process proceeds by a four-electron pathway, as is evident from the K–L plot. The number of electrons transferred in the ORR process is slightly above four, but this can be attributed to the electrode coating. The four-electron pathway is further confirmed by the attainment of the diffusion-limited current density at various electrode rotation rates in Figure 30b.

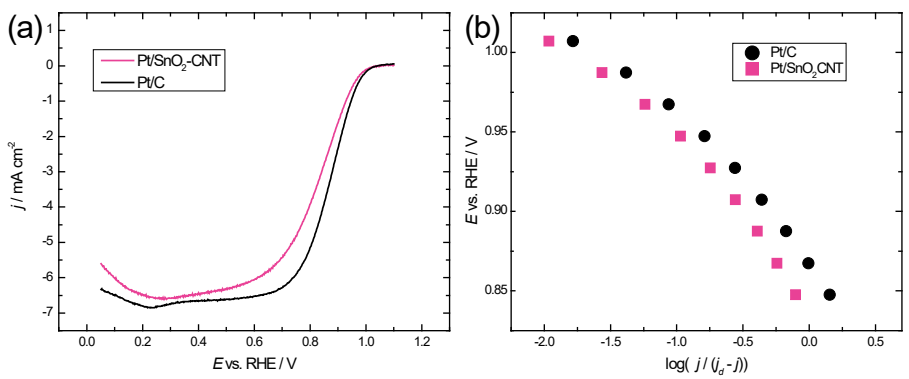

Figure 31. a) Comparison of the ORR polarization curves and b) Tafel plots derived from a) for O_2 reduction on Pt/SnO_2–CNT and Pt/C catalysts in O_2-saturated 0.1 M $HClO_4$ solution at 1900 rpm (v = 10 mV s^{-1}).

The Tafel slopes for both Pt/SnO_2–CNT and Pt/C are −61 mV, as provided in Table 6, and the Tafel plots are shown in Figure 31b. Both confirm that the transfer of the first electron to the O_2 molecule is the rate-determining step of the ORR.[120] In previous literature, Tafel slopes for PtNPs supported on oxide-coated carbon materials are around −60 mV.[90,169,182] However, Zhang et al. measured a Tafel slope of −80 mV for a Pt catalyst on SnO_2-decorated carbon fibers.[183] The Tafel slope value is dependent on the roughness of the electrode surface,[120] and some deviations are to be expected.

The specific and mass activities for the Pt/SnO_2–CNT and Pt/C catalysts were calculated at 0.9 V. The SA values for Pt/SnO_2–CNT and Pt/C are 0.15 and 0.05 mA cm^{-2}, respectively. There is a 3-fold increase in the ORR activity as compared to the commercial Pt/C catalyst. The improved SA is a result of the electronic interaction induced by the addition of SnO_2 to the electrocatalytic system. The electronic interaction is further confirmed in Figure 29b, where the bifunctional mechanism occurs, in which oxygen vacancies are created due to SnO_2 being adjacent to PtNPs.[169,176,178] Thus, confirming that when SnO_2 is added to CNTs via ALD to serve as a support for PtNPs, the overall ORR activity increases.

The mass activity of Pt/SnO_2–CNT is 44 A g^{-1}, which was calculated using the loading of Pt from the XRF measurements (Table 6). The MA of Pt/C was 61 A g^{-1}. Hussain et al. reported similar findings in that the PtNPs supported on photo-deposited SnO_2 on CNTs had a lower MA as compared to commercial Pt/C; their synthesized catalyst has an MA of 72 A g^{-1} as compared to the commercial Pt/C, with an MA of 90 A g^{-1}.[173] Rivera Rocabado et al. suggested that the lower activity could be due to the PtNPs being less negatively charged and reacting with nucleophilic species, thus blocking sites for which the ORR could occur.[184] PtNPs supported on tin oxide-decorated carbons studied by Jia et al. followed a different trend; their synthesized catalyst of tin oxide on nitrogen-doped carbon had a mass activity that was 3.5 times more active than Pt/C.[180] The higher specific activity of our prepared Pt/SnO_2-CNT confirms that, when SnO_2 is added to CNTs via ALD, the overall electrocatalytic activity of the PtNPs is improved through the electronic interaction.

Table 6. Pt content, ECSA and kinetic parameters for ORR of Pt/SnO_2–CNT and Pt/C catalysts in 0.1 M $HClO_4$ solution.

Catalyst	Pt content (wt%)	ECSA (cm^2)	$E_{1/2}$ (V)	Tafel slope (mV)	SA @ 0.9 V (mA cm^{-2})	MA @ 0.9 V (A g^{-1})
Pt/SnO_2-CNT	15 ± 3 [1]	0.96 ± 0.02	0.83 ± 0.01	-61 ± 2	0.15 ± 0.03	44 ± 9
Pt/C	20	4.7 ± 0.2	0.88 ± 0.01	-61 ± 1	0.05 ± 0.01	61 ± 6

[1] from XRF analysis.

6.4.4 Accelerated durability testing of PtNPs on SnO_2-CNT

The ADT was conducted in an Ar-saturated 0.1 M $HClO_4$ solution by applying 12,500 potential scans between 0.05 and 1.2 V using a scan rate of 100 mV s^{-1}. CV and RDE measurements were conducted prior to starting and following the ADT experiment and are shown in Figure 32 and Figure 33, respectively. Figure 32b shows a drastic decrease in the hydrogen adsorption/desorption and Pt oxide regions, indicating the dissolution and Ostwald ripening of Pt on the catalyst; there is also a decrease in the carbon characteristic area, which could indicate carbon corrosion occurring during the stability testing, whereas this is not as present on the synthesized Pt/SnO_2-CNT catalyst. Changes also appear in the Pt/SnO_2-CNT catalyst; however, these are not as drastic, which could indicate the strong stability enhancements provided to the catalyst due to the SnO_2 coating, which induces an SMSI. The ECSA of both the prepared Pt/SnO_2-CNT and Pt/C catalysts was calculated before and after the durability testing and was found to have decreased. Pt/SnO_2-CNT retained 58% of its original ECSA, while Pt/C only retained 31%, further emphasizing the superior stability afforded to the support as a result of the inclusion of SnO_2 onto the CNTs. This could be due to the anti-corrosion properties that SnO_2 enacts onto the CNTs, which ultimately results in lower dissolution of PtNPs.[168] Following the ADT, the addition of a peak around 0.6 V on the Pt/SnO_2-CNT catalyst was observed. This peak could be attributed to the two-electron transfer of quinone/hydroquinone.[168,185,186] Hussain et al. also concluded that a Pt–Sn alloy was present on the CVs of a photo-deposited SnO_2-CNT catalyst,[169] which could indicate why the total ECSA of Pt/SnO_2-CNT did not decrease to the same extent as the Pt/C catalyst.

Figure 33 compares the RDE results before and after the ADT experiments. In Figure 33a, there is a change in the electrocatalytic behavior of the Pt/SnO_2-CNT catalyst after the ADT experiments, showing an effect of SnO_2 on the overall ORR electrocatalytic activity of the catalyst. Both catalysts exhibit similar shifts in $E_{1/2}$ by 30 mV. This increased stability could be a result of the anchoring properties that SnO_2 provides to the PtNPs due to strong electronic interactions as a result of the Pt–O–Sn bonds, which strengthen the anchoring of the PtNPs and reduce their coalescence.[85,187] The introduction of SnO_2 onto the CNTs induces a synergetic effect by redistributing charges in the carbon 2p-states and the valence and conductive bands of SnO_2,[85] which increases the overall stability of the support. The onset potential of the synthesized Pt/SnO_2-CNT catalyst changes by 4 mV throughout the entirety of the ADT, while that of Pt/C decreases by 10 mV, showing the superior stability afforded to the synthesized catalyst through the electronic interaction with SnO_2. The addition of a metal oxide may be able to explain this, as Promsawan et al. mentioned that there is a decreased amount of carbonaceous intermediate species.[188] The results herein confirm that depositing SnO_2 via ALD onto the CNT surface results in strong support for PtNPs and produces an active, stable electrocatalyst.

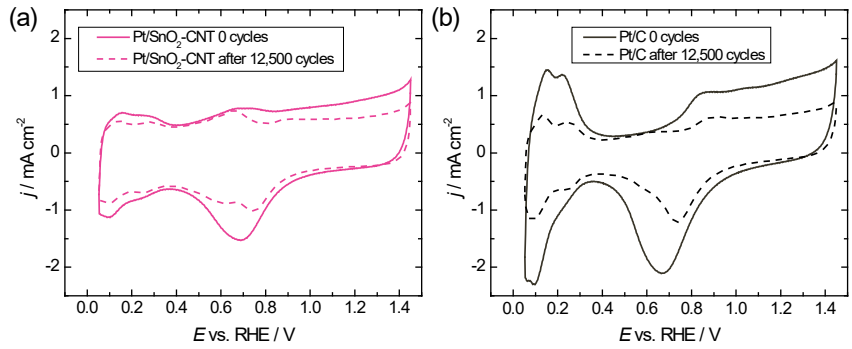

Figure 32. CVs for a) Pt/SnO_2-CNT and b) Pt/C catalysts before and after ADT in Ar-saturated 0.1 M $HClO_4$ solution (v = 50 mV s^{-1}). The current densities are normalized to the geometric surface area of the electrode.

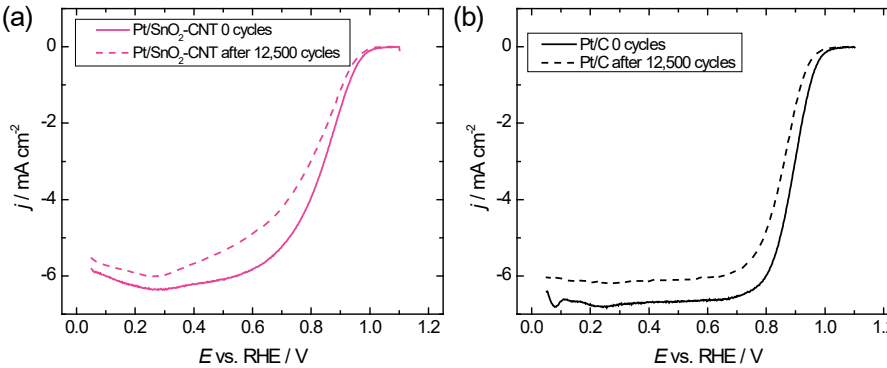

Figure 33. RDE polarization curves for the ORR on a) Pt/SnO_2-CNT and b) Pt/C catalysts at 1900 rpm before and after ADT in O_2-saturated 0.1 M $HClO_4$ solution (v = 10 mV s^{-1}).

7. SUMMARY

The effect that the functionalization of carbon support material has on the electrocatalytic activity of PtNPs was investigated using a variety of physical and electrochemical techniques. The ORR was investigated in a 0.1 M $HClO_4$ solution using the RDE method and single-cell PEMFC tests. The effects that commercially available heteroatom-doped graphene had on both electrochemically and chemically deposited PtNPs were systematically studied. Additionally, the effects of nitrogen-doped porous carbon and SnO_2-coated CNTs on the electrocatalytic activity of chemically deposited PtNPs were also studied.

In the first part of the PhD thesis, PtNPs were electrochemically deposited on commercially available heteroatom-doped graphene nanosheets using the chronoamperometric technique in which the electrode was held in 1 mM H_2PtCl_6 solution for 30 s at -0.30 V_{SCE}. For comparison, the deposition was also done with Vulcan carbon. In this work, the PtNPs deposited on dual heteroatom-doped graphenes have lower specific activity than those supported on single heteroatom-doped graphenes, with the exception of PtNPs supported on nitrogen-doped graphene. The PtNPs supported on boron-doped graphene had the highest specific activity, while the PtNPs supported on boron and nitrogen dual-doped graphene had the highest mass activity. Additionally, the PtNPs supported on N,B dual-doped graphene were more durable than those supported on N-doped graphene or B-doped graphene, suggesting a synergetic effect of the N and B heteroatoms interacting with the PtNPs.

In the second part of the thesis, PtNPs were chemically deposited on commercially available heteroatom-doped graphene nanosheets. The synthesized electrocatalysts were compared with a Vulcan carbon catalyst, with the PtNPs deposited in-house using the same chemical deposition method. In this section, the PtNPs deposited on dual heteroatom-doped graphene had a higher specific activity than those supported on single heteroatom-doped graphene. The PtNPs deposited on N,S dual-doped graphene possessed the highest specific activity for ORR, while those deposited on S-doped graphene had the lowest. The CO-stripping profiles varied among the electrocatalysts, further confirming the support effect on the PtNPs.

In the third part of the thesis, PtNPs were chemically deposited onto N-doped porous carbon. In this section, the deposition procedure was investigated, and PtNPs were deposited using both a one-pot and a two-pot synthesis method. The synthesized electrocatalysts were compared against a commercial 46% Pt/C catalyst. The catalyst synthesized by the two-pot route had a higher specific activity, while the catalyst synthesized by the one-pot route had a higher P_{max} in the single-cell PEMFC test. Thus, suggesting that the locality of the PtNPs within the pores of the carbon support further has an effect on their overall electrocatalytic activity.

In the final part of the thesis, PtNPs were chemically deposited onto SnO_2-coated CNTs. The synthesized electrocatalyst was compared against a commer-

cial 20% Pt/C catalyst. The synthesized electrocatalyst had a lower specific activity than the Pt/C catalyst but had a higher mass activity. The synthesized electrocatalyst also demonstrated superior durability during accelerated durability testing, with minimal ECSA loss compared to the commercial catalyst.

In all the studied electrocatalysts, the ORR proceeded via a 4-electron pathway, with the rate-determining step being the transfer of the first electron to the O_2 molecule. All of the electrocatalysts also had a Tafel slope close to -60 mV at low current densities. Thus, confirming ORR behavior similar to Pt electrocatalysts throughout the literature. Therefore, it was found that the functionalization of the carbon support onto which PtNPs are deposited affects the overall electrocatalytic activity of the PtNPs and the specific support effects should not be overlooked in the optimization of a Pt/C electrocatalyst for ORR.

8. REFERENCES

(1) *PEM Fuel Cell Electrocatalysts and Catalyst Layers: Fundamentals and Applications*; Zhang, J., Ed.; Springer London: London, 2008. https://doi.org/10.1007/978-1-84800-936-3.

(2) Adzic, R. Recent Advances in the Kinetics of Oxygen Reduction. In *Electrocatalysis;* Lipkowski, J.; Ross, P.N., Eds.; Wiley-VCH: New York, 1998; pp 197–242.

(3) Zhang, W.; Zhou, Q.; Bi, X.; Luo, L.; Cheng, Y.; Wang, R.; Chen, Z. Beyond Activity: The Unified Framework of the Sabatier Principle to Guide Rational Design of Durable and Active Electrocatalysts. *Carbon Energy* **2026**, e70246. https://doi.org/10.1002/cey2.70246.

(4) Holton, O. T.; Stevenson, J. W. The Role of Platinum in Proton Exchange Membrane Fuel Cells. *Platin. Met. Rev.* **2013**, *57* (4), 259–271. https://doi.org/10.1595/147106713X671222.

(5) Dong, J.-C.; Zhang, X.-G.; Briega-Martos, V.; Jin, X.; Yang, J.; Chen, S.; Yang, Z.-L.; Wu, D.-Y.; Feliu, J. M.; Williams, C. T.; Tian, Z.-Q.; Li, J.-F. In Situ Raman Spectroscopic Evidence for Oxygen Reduction Reaction Intermediates at Platinum Single-Crystal Surfaces. *Nat. Energy* **2018**, *4* (1), 60–67. https://doi.org/10.1038/s41560-018-0292-z.

(6) Maciá, M. D.; Campiña, J. M.; Herrero, E.; Feliu, J. M. On the Kinetics of Oxygen Reduction on Platinum Stepped Surfaces in Acidic Media. *J. Electroanal. Chem.* **2004**, *564*, 141–150. https://doi.org/10.1016/j.jelechem.2003.09.035.

(7) Kuzume, A.; Herrero, E.; Feliu, J. M. Oxygen Reduction on Stepped Platinum Surfaces in Acidic Media. *J. Electroanal. Chem.* **2007**, *599* (2), 333–343. https://doi.org/10.1016/j.jelechem.2006.05.006.

(8) Stamenkovic, V.; Markovic, N. M.; Ross, P. N. Structure-Relationships in Electrocatalysis: Oxygen Reduction and Hydrogen Oxidation Reactions on Pt(111) and Pt(100) in Solutions Containing Chloride Ions. *J. Electroanal. Chem.* **2001**, *500* (1–2), 44–51. https://doi.org/10.1016/S0022-0728(00)00352-1.

(9) Mayrhofer, K. J. J.; Strmcnik, D.; Blizanac, B. B.; Stamenkovic, V.; Arenz, M.; Markovic, N. M. Measurement of Oxygen Reduction Activities via the Rotating Disc Electrode Method: From Pt Model Surfaces to Carbon-Supported High Surface Area Catalysts. *Electrochim. Acta* **2008**, *53* (7), 3181–3188. https://doi.org/10.1016/j.electacta.2007.11.057.

(10) Wang, J. X.; Markovic, N. M.; Adzic, R. R. Kinetic Analysis of Oxygen Reduction on Pt(111) in Acid Solutions: Intrinsic Kinetic Parameters and Anion Adsorption Effects. *J. Phys. Chem. B* **2004**, *108* (13), 4127–4133. https://doi.org/10.1021/jp037593v.

(11) Kinoshita, K. Particle Size Effects for Oxygen Reduction on Highly Dispersed Platinum in Acid Electrolytes. *J. Electrochem. Soc.* **1990**, *137* (3), 845–848. https://doi.org/10.1149/1.2086566.

(12) Erikson, H.; Antoniassi, R. M.; Solla-Gullón, J.; Torresi, R. M.; Tammeveski, K.; Feliu, J. M. Oxygen Electroreduction on Small (<10 nm) and {100}-Oriented Pt Nanoparticles. *Electrochim. Acta* **2022**, *403*, 139631. https://doi.org/10.1016/j.electacta.2021.139631.

(13) Ciapina, E. G.; Santos, S. F.; Gonzalez, E. R. Electrochemical CO Stripping on Nanosized Pt Surfaces in Acid Media: A Review on the Issue of Peak Multiplicity. *J. Electroanal. Chem.* **2018**, *815*, 47–60.

https://doi.org/10.1016/j.jelechem.2018.02.047.
(14) Mayrhofer, K. J. J.; Blizanac, B. B.; Arenz, M.; Stamenkovic, V. R.; Ross, P. N.; Markovic, N. M. The Impact of Geometric and Surface Electronic Properties of Pt-Catalysts on the Particle Size Effect in Electrocatalysis. *J. Phys. Chem. B* **2005**, *109* (30), 14433–14440. https://doi.org/10.1021/jp051735z.
(15) Li, D.; Wang, C.; Strmcnik, D. S.; Tripkovic, D. V.; Sun, X.; Kang, Y.; Chi, M.; Snyder, J. D.; van der Vliet, D.; Tsai, Y.; Stamenkovic, V. R.; Sun, S.; Markovic, N. M. Functional Links between Pt Single Crystal Morphology and Nanoparticles with Different Size and Shape: The Oxygen Reduction Reaction Case. *Energy Environ. Sci.* **2014**, *7* (12), 4061–4069. https://doi.org/10.1039/C4EE01564A.
(16) Kabbabi, A.; Gloaguen, F.; Andolfatto, F.; Durand, R. Particle Size Effect for Oxygen Reduction and Methanol Oxidation on Pt/C inside a Proton Exchange Membrane. *J. Electroanal. Chem.* **1994**, *373* (1–2), 251–254. https://doi.org/10.1016/0022-0728(94)03503-2.
(17) Shao, Y.; Yin, G.; Gao, Y. Understanding and Approaches for the Durability Issues of Pt-Based Catalysts for PEM Fuel Cell. *J. Power Sources* **2007**, *171* (2), 558–566. https://doi.org/10.1016/j.jpowsour.2007.07.004.
(18) Lagarteira, T.; Delgado, S.; Garcia, G. P.; Ortiz, A.; Mendes, A. Oxygen Reduction Stability of Graphene-Supported Electrocatalyst: Electrochemical and Morphological Evidences. *Int. J. Hydrog. Energy* **2023**, *48* (54), 20901–20913. https://doi.org/10.1016/j.ijhydene.2023.03.359.
(19) Wikander, K.; Ekström, H.; Palmqvist, A. E. C.; Lindbergh, G. On the Influence of Pt Particle Size on the PEMFC Cathode Performance. *Electrochim. Acta* **2007**, *52* (24), 6848–6855. https://doi.org/10.1016/j.electacta.2007.04.106.
(20) Perez-Alonso, F. J.; McCarthy, D. N.; Nierhoff, A.; Hernandez-Fernandez, P.; Strebel, C.; Stephens, I. E. L.; Nielsen, J. H.; Chorkendorff, I. The Effect of Size on the Oxygen Electroreduction Activity of Mass-Selected Platinum Nanoparticles. *Angew. Chem. Int. Ed.* **2012**, *51* (19), 4641–4643. https://doi.org/10.1002/anie.201200586.
(21) Inaba, M.; Zana, A.; Quinson, J.; Bizzotto, F.; Dosche, C.; Dworzak, A.; Oezaslan, M.; Simonsen, S. B.; Kuhn, L. T.; Arenz, M. The Oxygen Reduction Reaction on Pt: Why Particle Size and Interparticle Distance Matter. *ACS Catal.* **2021**, *11* (12), 7144–7153. https://doi.org/10.1021/acscatal.1c00652.
(22) Nesselberger, M.; Ashton, S.; Meier, J. C.; Katsounaros, I.; Mayrhofer, K. J. J.; Arenz, M. The Particle Size Effect on the Oxygen Reduction Reaction Activity of Pt Catalysts: Influence of Electrolyte and Relation to Single Crystal Models. *J. Am. Chem. Soc.* **2011**, *133* (43), 17428–17433. https://doi.org/10.1021/ja207016u.
(23) Yano, H.; Watanabe, M.; Iiyama, A.; Uchida, H. Particle-Size Effect of Pt Cathode Catalysts on Durability in Fuel Cells. *Nano Energy* **2016**, *29*, 323–333. https://doi.org/10.1016/j.nanoen.2016.02.016.
(24) Xu, Z.; Zhang, H.; Zhong, H.; Lu, Q.; Wang, Y.; Su, D. Effect of Particle Size on the Activity and Durability of the Pt/C Electrocatalyst for Proton Exchange Membrane Fuel Cells. *Appl. Catal. B Environ.* **2012**, *111–112*, 264–270. https://doi.org/10.1016/j.apcatb.2011.10.007.
(25) Tritsaris, G. A.; Greeley, J.; Rossmeisl, J.; Nørskov, J. K. Atomic-Scale Modeling of Particle Size Effects for the Oxygen Reduction Reaction on Pt. *Catal. Lett.* **2011**, *141* (7), 909–913. https://doi.org/10.1007/s10562-011-0637-8.

(26) Sheng, W.; Chen, S.; Vescovo, E.; Shao-Horn, Y. Size Influence on the Oxygen Reduction Reaction Activity and Instability of Supported Pt Nanoparticles. *J. Electrochem. Soc.* **2011**, *159* (2), B96–B103. https://doi.org/10.1149/2.009202jes.
(27) Sandbeck, D. J. S.; Secher, N. M.; Speck, F. D.; Sørensen, J. E.; Kibsgaard, J.; Chorkendorff, I.; Cherevko, S. Particle Size Effect on Platinum Dissolution: Considerations for Accelerated Stability Testing of Fuel Cell Catalysts. *ACS Catal.* **2020**, *10* (11), 6281–6290. https://doi.org/10.1021/acscatal.0c00779.
(28) Gan, L.; Rudi, S.; Cui, C.; Heggen, M.; Strasser, P. Size-Controlled Synthesis of Sub-10 Nm $PtNi_3$ Alloy Nanoparticles and Their Unusual Volcano-Shaped Size Effect on ORR Electrocatalysis. *Small* **2016**, *12* (23), 3189–3196. https://doi.org/10.1002/smll.201600027.
(29) Sánchez-Sánchez, C. M.; Solla-Gullón, J.; Vidal-Iglesias, F. J.; Aldaz, A.; Montiel, V.; Herrero, E. Imaging Structure Sensitive Catalysis on Different Shape-Controlled Platinum Nanoparticles. *J. Am. Chem. Soc.* **2010**, *132* (16), 5622–5624. https://doi.org/10.1021/ja100922h.
(30) Shinozaki, K.; Morimoto, Y.; Pivovar, B. S.; Kocha, S. S. Re-Examination of the Pt Particle Size Effect on the Oxygen Reduction Reaction for Ultrathin Uniform Pt/C Catalyst Layers without Influence from Nafion. *Electrochim. Acta* **2016**, *213*, 783–790. https://doi.org/10.1016/j.electacta.2016.08.001.
(31) Jackson, C.; Smith, G. T.; Mpofu, N.; Dawson, J. M. S.; Khoza, T.; September, C.; Taylor, S. M.; Inwood, D. W.; Leach, A. S.; Kramer, D.; Russell, A. E.; Kucernak, A. R. J.; Levecque, P. B. J. A Quick and Versatile One Step Metal–Organic Chemical Deposition Method for Supported Pt and Pt-Alloy Catalysts. *RSC Adv.* **2020**, *10* (34), 19982–19996. https://doi.org/10.1039/D0RA03001E.
(32) Woitassek, D.; Lerch, S.; Jiang, W.; Shviro, M.; Roitsch, S.; Strassner, T.; Janiak, C. The Facile Deposition of Pt Nanoparticles on Reduced Graphite Oxide in Tunable Aryl Alkyl Ionic Liquids for ORR Catalysts. *Molecules* **2022**, *27* (3), 1018. https://doi.org/10.3390/molecules27031018.
(33) Gao, M.; Lin, Z.; Jiang, J.; Cui, C.; Zheng, Y.; Yu, S. Completely Green Synthesis of Colloid Adams' Catalyst α-PtO_2 Nanocrystals and Derivative Pt Nanocrystals with High Activity and Stability for Oxygen Reduction. *Chem. Eur. J.* **2012**, *18* (27), 8423–8429. https://doi.org/10.1002/chem.201200353.
(34) Meng, H.; Zhan, Y.; Zeng, D.; Zhang, X.; Zhang, G.; Jaouen, F. Factors Influencing the Growth of Pt Nanowires via Chemical Self-Assembly and Their Fuel Cell Performance. *Small* **2015**, *11* (27), 3377–3386. https://doi.org/10.1002/smll.201402904.
(35) Taylor, S.; Fabbri, E.; Levecque, P.; Schmidt, T. J.; Conrad, O. The Effect of Platinum Loading and Surface Morphology on Oxygen Reduction Activity. *Electrocatalysis* **2016**, *7* (4), 287–296. https://doi.org/10.1007/s12678-016-0304-3.
(36) Venkateswara Rao, Ch.; Viswanathan, B. ORR Activity and Direct Ethanol Fuel Cell Performance of Carbon-Supported Pt−M (M = Fe, Co, and Cr) Alloys Prepared by Polyol Reduction Method. *J. Phys. Chem. C* **2009**, *113* (43), 18907–18913. https://doi.org/10.1021/jp9041606.
(37) López-Cudero, A.; Solla-Gullón, J.; Herrero, E.; Aldaz, A.; Feliu, J. M. CO Electro-oxidation on Carbon Supported Platinum Nanoparticles: Effect of Aggregation. *J. Electroanal. Chem.* **2010**, *644* (2), 117–126. https://doi.org/10.1016/j.jelechem.2009.06.016.
(38) Alexeyeva, N.; Tammeveski, K.; Lopez-Cudero, A.; Solla-Gullón, J.; Feliu, J. M. Electroreduction of Oxygen on Pt Nanoparticle/Carbon Nanotube Nanocomposites

in Acid and Alkaline Solutions. *Electrochim. Acta* **2010**, *55* (3), 794–803. https://doi.org/10.1016/j.electacta.2009.09.030.
(39) Park, S.-J.; Cho, W.; Oh, M.; Kim, J.; Kim, K. M.; Lee, Y.-G.; Kim, S. Precursor Solvent Influence on Preparation and Electrochemical Properties of Platinum Nanoparticles Electrodes. *J. Nanosci. Nanotechnol.* **2012**, *12* (2), 1705–1708. https://doi.org/10.1166/jnn.2012.4678.
(40) Wang, Y.-J.; Zhao, N.; Fang, B.; Li, H.; Bi, X. T.; Wang, H. Effect of Different Solvent Ratio (Ethylene Glycol/Water) on the Preparation of Pt/C Catalyst and Its Activity toward Oxygen Reduction Reaction. *RSC Adv.* **2015**, *5* (70), 56570–56577. https://doi.org/10.1039/C5RA08068A.
(41) Cao, F.; Zang, Z.; Sun, S.; Sun, X.; Li, X.; Liu, T.; Wu, J. The Influence of Deposited Potential on the ORR Activity of Pt Catalysts on Glassy Carbon Electrode. *RSC Adv.* **2017**, *7* (41), 25429–25436. https://doi.org/10.1039/C7RA02444D.
(42) Dhanasekaran, P.; Lokesh, K.; Ojha, P. K.; Sahu, A. K.; Bhat, S. D.; Kalpana, D. Electrochemical Deposition of Three-Dimensional Platinum Nanoflowers for High-Performance Polymer Electrolyte Fuel Cells. *J. Colloid Interface Sci.* **2020**, *572*, 198–206. https://doi.org/10.1016/j.jcis.2020.03.078.
(43) Ye, F.; Wang, Z.; Xu, C.; Yuan, M.; Liu, P.; Yang, W.; Liu, G. Mechanism and Kinetic Study of Pulse Electrodeposition Process of Pt/C Catalysts for Fuel Cells. *Renew. Energy* **2020**, *145*, 514–520. https://doi.org/10.1016/j.renene.2019.06.034.
(44) Hussain, S.; Erikson, H.; Kongi, N.; Merisalu, M.; Rähn, M.; Sammelselg, V.; Maia, G.; Tammeveski, K. Platinum Particles Electrochemically Deposited on Multi-walled Carbon Nanotubes for Oxygen Reduction Reaction in Acid Media. *J. Electrochem. Soc.* **2017**, *164* (9), F1014–F1021. https://doi.org/10.1149/2.0091712jes.
(45) Huang, C.; Bunmi Odetola, C.; Rodgers, M. Nanoparticle Seeded Pulse Electro-deposition for Preparing High Performance Pt/C Electrocatalysts. *Appl. Catal. Gen.* **2015**, *499*, 55–65. https://doi.org/10.1016/j.apcata.2015.03.043.
(46) Hussain, S.; Erikson, H.; Kozlova, J.; Tamm, A.; Tammeveski, K. Comparing Pt Electrodeposition Processes on Nitrogen-Doped Graphene Nanosheets for the Electroreduction of Oxygen. *J. Solid State Electrochem.* **2023**, *28*, 1681–1690. https://doi.org/10.1007/s10008-023-05687-4.
(47) Ma, J.; Habrioux, A.; Alonso-Vante, N. The Effect of Substrates at Cathodes in Low-temperature Fuel Cells. *ChemElectroChem* **2014**, *1* (1), 37–46. https://doi.org/10.1002/celc.201300105.
(48) Mukherjee, S.; Bates, A.; Lee, S. C.; Lee, D.-H.; Park, S. A Review of the Application of CNTs in PEM Fuel Cells. *Int. J. Green Energy* **2015**, *12* (8), 787–809. https://doi.org/10.1080/15435075.2013.867270.
(49) Kongkanand, A.; Kuwabata, S.; Girishkumar, G.; Kamat, P. Single-Wall Carbon Nanotubes Supported Platinum Nanoparticles with Improved Electrocatalytic Activity for Oxygen Reduction Reaction. *Langmuir* **2006**, *22* (5), 2392–2396. https://doi.org/10.1021/la052753a.
(50) Rasouli, S.; Myers, D.; Higashida, K.; Nakashima, N.; Crozier, P.; Ferreira, P. Electrochemical Evolution of Fuel Cell Platinum Nanocatalysts on Carbon Nanotubes at the Atomic Scale. *ACS Appl. Energy Mater.* **2023**, *6* (23), 11861–11873. https://doi.org/10.1021/acsaem.3c01765.
(51) Del Carmen Gimenez-Lopez, M.; Kurtoglu, A.; Walsh, D. A.; Khlobystov, A. N. Extremely Stable Platinum-Amorphous Carbon Electrocatalyst within Hollow

Graphitized Carbon Nanofibers for the Oxygen Reduction Reaction. *Adv. Mater.* **2016**, *28* (41), 9103–9108. https://doi.org/10.1002/adma.201602485.
(52) Zhang, W.; Wang, Z.; Shen, Y.; Xi, M.; Chu, X.; Xi, C. Graphene Supported Platinum Nanoparticles as Catalyst for Oxygen Reduction Reaction. *Chem. Res. Chin. Univ.* **2015**, *31* (6), 1007–1011. https://doi.org/10.1007/s40242-015-5171-6.
(53) Xin, L.; Yang, F.; Rasouli, S.; Qiu, Y.; Li, Z.-F.; Uzunoglu, A.; Sun, C.-J.; Liu, Y.; Ferreira, P.; Li, W.; Ren, Y.; Stanciu, L. A.; Xie, J. Understanding Pt Nanoparticle Anchoring on Graphene Supports through Surface Functionalization. *ACS Catal.* **2016**, *6* (4), 2642–2653. https://doi.org/10.1021/acscatal.5b02722.
(54) Angel, G. M. A.; Mansor, N.; Jervis, R.; Rana, Z.; Gibbs, C.; Seel, A.; Kilpatrick, A. F. R.; Shearing, P. R.; Howard, C. A.; Brett, D. J. L.; Cullen, P. L. Realising the Electrochemical Stability of Graphene: Scalable Synthesis of an Ultra-Durable Platinum Catalyst for the Oxygen Reduction Reaction. *Nanoscale* **2020**, *12* (30), 16113–16122. https://doi.org/10.1039/D0NR03326J.
(55) Kikkawa, N.; Kimura, M. Comprehensive Molecular Dynamics Study of Oxygen Diffusion in Carbon Mesopores: Insights for Designing Fuel-Cell Catalyst Supports. *Langmuir* **2024**, *40* (3), 1674–1687. https://doi.org/10.1021/acs.langmuir.3c02627.
(56) Kamitaka, Y.; Takeshita, T.; Morimoto, Y. MgO-Templated Mesoporous Carbon as a Catalyst Support for Polymer Electrolyte Fuel Cells. *Catalysts* **2018**, *8* (6), 230. https://doi.org/10.3390/catal8060230.
(57) Shen, L.; Ma, M.; Zhao, Z.; Tu, F.; Liu, J.; Xu, B.; Zhang, Y.; Zhao, L.; Shao, G.; Wang, Z. The Relative Humidity Sensitivity of Fuel Cell Catalyst Layer with Solid or Porous Carbon Support Structure. *J. Power Sources* **2023**, *575*, 233202. https://doi.org/10.1016/j.jpowsour.2023.233202.
(58) Perazzolo, V.; Brandiele, R.; Durante, C.; Zerbetto, M.; Causin, V.; Rizzi, G. A.; Cerri, I.; Granozzi, G.; Gennaro, A. Density Functional Theory (DFT) and Experimental Evidences of Metal–Support Interaction in Platinum Nanoparticles Supported on Nitrogen- and Sulfur-Doped Mesoporous Carbons: Synthesis, Activity, and Stability. *ACS Catal.* **2018**, *8* (2), 1122–1137. https://doi.org/10.1021/acscatal.7b03942.
(59) Sakthivel, M.; Drillet, J.-F. An Extensive Study about Influence of the Carbon Support Morphology on Pt Activity and Stability for Oxygen Reduction Reaction. *Appl. Catal. B Environ.* **2018**, *231*, 62–72. https://doi.org/10.1016/j.apcatb.2018.02.050.
(60) Zhao, Z.; Castanheira, L.; Dubau, L.; Berthomé, G.; Crisci, A.; Maillard, F. Carbon Corrosion and Platinum Nanoparticles Ripening under Open Circuit Potential Conditions. *J. Power Sources* **2013**, *230*, 236–243. https://doi.org/10.1016/j.jpowsour.2012.12.053.
(61) Liu, Y.; Ji, C.; Gu, W.; Jorne, J.; Gasteiger, H. A. Effects of Catalyst Carbon Support on Proton Conduction and Cathode Performance in PEM Fuel Cells. *J. Electrochem. Soc.* **2011**, *158* (6), B614–B621. https://doi.org/10.1149/1.3562945.
(62) Li, H.; You, J.; Cheng, X.; Luo, L.; Yan, X.; Yin, J.; Shen, S.; Zhang, J. Unraveling the Effects of Carbon Corrosion on Oxygen Transport Resistance in Low Pt Loading Proton Exchange Membrane Fuel Cells. *ACS Appl. Mater. Interfaces* **2024**, *16* (1), 540–554. https://doi.org/10.1021/acsami.3c13450.
(63) Zhu, J.; Wei, P.; Li, K.; He, S.; Pan, Z.; Nie, S.; Key, J.; Shen, P. K. Self-Assembled Nanofiber Networks of Well-Separated B and N Codoped Carbon as Pt Supports for Highly Efficient and Stable Oxygen Reduction Electrocatalysis. *ACS Sustain. Chem. Eng.* **2019**, *7* (1), 660–668. https://doi.org/10.1021/acssuschemeng.8b04259.

(64) Müller, M.; Kintzel, B.; Seidel, C.; Günthel, M.; Kunkel, R.; Tübke, J. Functionalization and Characterization of Supports for Catalysts in Fuel Cells. *Appl. Surf. Sci.* **2026**, *737*, 166885. https://doi.org/10.1016/j.apsusc.2026.166885.
(65) Lv, Q.; Wang, N.; Si, W.; Hou, Z.; Li, X.; Wang, X.; Zhao, F.; Yang, Z.; Zhang, Y.; Huang, C. Pyridinic Nitrogen Exclusively Doped Carbon Materials as Efficient Oxygen Reduction Electrocatalysts for Zn-Air Batteries. *Appl. Catal. B Environ.* **2020**, *261*, 118234. https://doi.org/10.1016/j.apcatb.2019.118234.
(66) Yi, L.; Yu, Y.; Tao, Y.; Hu, W. Pt–Co Intermetallic Nanoparticles Anchored on Nitrogen-Rich Graphene for Efficient Oxygen Reduction Reaction in Acid. *Int. J. Hydrog. Energy* **2026**, *200*, 152821. https://doi.org/10.1016/j.ijhydene.2025.152821.
(67) Hornberger, E.; Merzdorf, T.; Schmies, H.; Hübner, J.; Klingenhof, M.; Gernert, U.; Kroschel, M.; Anke, B.; Lerch, M.; Schmidt, J.; Thomas, A.; Chattot, R.; Martens, I.; Drnec, J.; Strasser, P. Impact of Carbon N-Doping and Pyridinic-N Content on the Fuel Cell Performance and Durability of Carbon-Supported Pt Nanoparticle Catalysts. *ACS Appl. Mater. Interfaces* **2022**, *14* (16), 18420–18430. https://doi.org/10.1021/acsami.2c00762.
(68) Groves, M. N.; Chan, A. S. W.; Malardier-Jugroot, C.; Jugroot, M. Improving Platinum Catalyst Binding Energy to Graphene through Nitrogen Doping. *Chem. Phys. Lett.* **2009**, *481* (4–6), 214–219. https://doi.org/10.1016/j.cplett.2009.09.074.
(69) Xie, Z.; Zhang, D.; Peng, H.; Lei, Y.; Yang, B.; Liang, F. Nitrogen Doped Single-Walled Carbon Nanohorns as Pt Catalyst Carrier: Balance of Strong Durability and High Activity of ORR. *Int. J. Miner. Metall. Mater.* **2025**, *32* (9), 2260–2269. https://doi.org/10.1007/s12613-025-3113-y.
(70) Haque, Md. A.; Kurosaki, R.; Oiwa, K.; Ikeda, K.; Sato, K.; Nishi, N.; Tachibana, H.; Kawawaki, T.; Negishi, Y. Suppression of Pt Nanocluster Aggregation and Enhanced Oxygen Reduction Activity by Heteroatom Doping of Carbon Nanotubes. *ACS Appl. Energy Mater.* **2024**, *7* (22), 10317–10325. https://doi.org/10.1021/acsaem.4c01742.
(71) Yang, C.-L.; Wang, L.-N.; Yin, P.; Liu, J.; Chen, M.-X.; Yan, Q.-Q.; Wang, Z.-S.; Xu, S.-L.; Chu, S.-Q.; Cui, C.; Ju, H.; Zhu, J.; Lin, Y.; Shui, J.; Liang, H.-W. Sulfur-Anchoring Synthesis of Platinum Intermetallic Nanoparticle Catalysts for Fuel Cells. *Science* **2021**, *374* (6566), 459–464. https://doi.org/10.1126/science.abj9980.
(72) Panchakarla, L. S.; Subrahmanyam, K. S.; Saha, S. K.; Govindaraj, A.; Krishnamurthy, H. R.; Waghmare, U. V.; Rao, C. N. R. Synthesis, Structure and Properties of Boron and Nitrogen Doped Graphene. arXiv February 18, 2009. http://arxiv.org/abs/0902.3077 (accessed 2022-10-17).
(73) Liu, D.; Gao, S.; Xu, J.; Zhang, X.; Yang, Z.; Yang, T.; Wang, B.; Yang, S.; Liang, C.; Kong, C. Boron Induced Strong Metal-Support Interaction for High Sintering Resistance of Pt-Based Catalysts toward Oxygen Reduction Reaction. *Appl. Surf. Sci.* **2022**, *604*, 154466. https://doi.org/10.1016/j.apsusc.2022.154466.
(74) Shen, J.-F.; Hu, S.-N.; Tian, N.; Li, M.-Y.; Yang, S.-L.; Tian, S.-Y.; Chen, M.-S.; Zhou, Z.-Y.; Sun, S.-G. P-Doping Strategy Increasing the Durability of PtCo Nanoparticles for the Oxygen Reduction Reaction. *ACS Sustain. Chem. Eng.* **2023**, *11* (31), 11660–11667. https://doi.org/10.1021/acssuschemeng.3c02903.
(75) Wen, Y.; Wang, B.; Huang, C.; Wang, L.; Hulicova-Jurcakova, D. Synthesis of Phosphorus-Doped Graphene and Its Wide Potential Window in Aqueous Supercapacitors. *Chem. Eur. J.* **2015**, *21* (1), 80–85. https://doi.org/10.1002/chem.201404779.

(76) Zhu, J.; He, G.; Tian, Z.; Liang, L.; Shen, P. K. Facile Synthesis of Boron and Nitrogen-Dual-Doped Graphene Sheets Anchored Platinum Nanoparticles for Oxygen Reduction Reaction. *Electrochim. Acta* **2016**, *194*, 276–282. https://doi.org/10.1016/j.electacta.2016.01.222.
(77) Ukai, J.; Wang, P.; Chae, S.; Akceoglu, G. A.; Pakkang, N.; Sawada, Y.; Saito, N. Fabrication of Pt Nanoparticles Encapsulated by N, P Co-Doped Carbon via Solution Plasma for the Oxygen Reduction Reaction. *J. Electroanal. Chem.* **2025**, *994*, 119273. https://doi.org/10.1016/j.jelechem.2025.119273.
(78) Liu, Z.; Qu, J.; Fu, X.; Wang, Q.; Zhong, G.; Peng, F. Low Pt Content Catalyst Supported on Nitrogen and Phosphorus-Codoped Carbon Nanotubes for Electrocatalytic O_2 Reaction in Acidic Medium. *Mater. Lett.* **2015**, *142*, 115–118. https://doi.org/10.1016/j.matlet.2014.12.011.
(79) Renugadevi, C.; Singh, A. P.; Cindrella, L. Tailored Pt–rGO Catalyst with Dual Heteroatom Doping: A Synergistic Leap in HER and ORR Electrocatalysis. *Electrocatalysis* **2026**, *17* (1), 155–172. https://doi.org/10.1007/s12678-025-00995-x.
(80) Fan, F.; Che, Y.; Efimov, V.; Anton, K.; Yan, S.; Bian, T. Hofmann-Type MOFs Derived Small-Sized Pt Nanoparticles Embedded in S, N Codoped Carbon Matrix for Enhanced Oxygen Reduction Reaction. *J. Electroanal. Chem.* **2025**, *998*, 119545. https://doi.org/10.1016/j.jelechem.2025.119545.
(81) Pan, P.; Liang, J.; Zhou, W.; Zhong, C.; Tan, W.; Song, H.; Zhang, H.; Cui, Z. Engineering Strong p-p Orbital Coupling Stabilizing Pt Nanoparticles for Highly Efficient and Durable Cathode of Fuel Cells. *J. Energy Chem.* **2026**, *117*, 709–717. https://doi.org/10.1016/j.jechem.2026.02.043.
(82) Jin, H.; Jiang, N.; Chen, Y.; Feng, Z.; Cheng, H.; Guan, L. High-Yield Synthesis of FeNC as Support of PtFe Nanoparticles for the Oxygen Reduction Reaction by a Green Ball Milling Method. *Nanotechnology* **2025**, *36* (15), 155402. https://doi.org/10.1088/1361-6528/adb8c2.
(83) Niu, F.; Pang, Y.; Liu, W.; Shi, Z.; Cui, Y.; Yang, Z.; Yang, S.; Yin, Y. Strong Metal-Support Interaction Induced by Oxygen Vacancies to Enhance the Activity and Durability of Pt/TiO_2/ Hollow Carbon Nanospheres ORR Catalyst. *J. Alloys Compd.* **2025**, *1010*, 177039. https://doi.org/10.1016/j.jallcom.2024.177039.
(84) Gao, W.; Zhang, Z.; Dou, M.; Wang, F. Highly Dispersed and Crystalline Ta_2O_5 Anchored Pt Electrocatalyst with Improved Activity and Durability Toward Oxygen Reduction: Promotion by Atomic-Scale Pt–Ta_2O_5 Interactions. *ACS Catal.* **2019**, *9* (4), 3278–3288. https://doi.org/10.1021/acscatal.8b04505.
(85) Guan, J.; Zan, Y.; Shao, R.; Niu, J.; Dou, M.; Zhu, B.; Zhang, Z.; Wang, F. Phase Segregated Pt–SnO_2/C Nanohybrids for Highly Efficient Oxygen Reduction Electrocatalysis. *Small* **2020**, *16* (51), 2005048. https://doi.org/10.1002/smll.202005048.
(86) Liu, X.; Zhu, S.; Li, S.; Li, L.; Zhu, X.; Tang, H.; Wang, Y. Pt Nanoparticles Supported on N-Doped TiO_2/C Composite Supports for Fuel Cell Catalysis. *J. Alloys Compd.* **2025**, *1042*, 184103. https://doi.org/10.1016/j.jallcom.2025.184103.
(87) Zhang, N.; Yang, L.; Bai, J.; Lan, C.; Xiao, M.; Xing, W.; Liu, C. TaO_x-C Supported Ultra-Small Platinum Nanoparticles as Efficient and Durable Catalysts for PEMFCs. *Chin. Chem. Lett.* **2026**, *37* (6), 111044. https://doi.org/10.1016/j.cclet.2025.111044.

(88) Hussain, S.; Erikson, H.; Kongi, N.; Sarapuu, A.; Solla-Gullón, J.; Maia, G.; Kannan, A. M.; Alonso-Vante, N.; Tammeveski, K. Oxygen Reduction Reaction on Nanostructured Pt-Based Electrocatalysts: A Review. *Int. J. Hydrog. Energy* **2020**, *45* (56), 31775–31797. https://doi.org/10.1016/j.ijhydene.2020.08.215.
(89) Hoque, M. A.; Higgins, D. C.; Hassan, F. M.; Choi, J.-Y.; Pritzker, M. D.; Chen, Z. Tin Oxide – Mesoporous Carbon Composites as Platinum Catalyst Supports for Ethanol Oxidation and Oxygen Reduction. *Electrochim. Acta* **2014**, *121*, 421–427. https://doi.org/10.1016/j.electacta.2013.12.075.
(90) Elezovic, N. R.; Radmilovic, V. R.; Kovac, J.; Babic, B. M.; Gaijic-Krstajic, Lj. M.; Krstajic, N. V. Pt Nanoparticles on Tin Oxide Based Support as a Beneficial Catalyst for Oxygen Reduction in Alkaline Solutions. *RSC Adv.* **2015**, *5* (21), 15923–15929. https://doi.org/10.1039/C4RA13391A.
(91) Murase, R.; Inaba, M.; Matsuoka, Y.; Kamitaka, Y.; Yoshino, S.; Koiwai, A.; Takeshita, T.; Kodama, K. Influence of Ionomer Content in Pt/Mesoporous SnO_2 Electrodes on PEM Fuel Cell Performance. *ECS Adv.* **2025**, *4* (1), 014503. https://doi.org/10.1149/2754-2734/adb31b.
(92) Cao, W.; Mao, Y.; Hu, B.; Yang, Y.; Zhou, W.; Shao, Z. Significantly Improved Stability and Water Retention for Pt Supported on W-Doped SnO_2 to Catalyse the Oxygen Reduction Reaction in Proton Exchange Membrane Fuel Cells. *J. Mater. Chem. A* **2024**, *12* (18), 10799–10807. https://doi.org/10.1039/D4TA00388H.
(93) European Commission. Joint Research Centre; Weidner, E.; Dolci, F.; Georgakaki, A.; Letout, S.; Mountraki, A.; Ince, E.; Shtjefni, D. *Clean Energy Technology Observatory, Fuel Cell Technology in the European Union*; EUR; Publications Office of the European Union: LU, 2025. https://doi.org/10.2760/0458721.
(94) Hou, Y.; Deng, H.; Pan, F.; Chen, W.; Du, Q.; Jiao, K. Pore-Scale Investigation of Catalyst Layer Ingredient and Structure Effect in Proton Exchange Membrane Fuel Cell. *Appl. Energy* **2019**, *253*, 113561. https://doi.org/10.1016/j.apenergy.2019.113561.
(95) Liu, Y.; Li, X.; Xia, Y.; Cai, X.; Du, A.; Lin, R. Mitigating Mass Transport Capacity in Ultralow Pt PEMFCs via Optimization of Ionomer Coverage and Pt Utilization. *ACS Appl. Mater. Interfaces* **2026**, *18* (17), 24365–24377. https://doi.org/10.1021/acsami.5c25006.
(96) Wang, Y.; Qin, S.; Ma, F.; Wang, C.; He, W.; Zhang, B.; Li, H. Boosting PEM Fuel Cell Performance with a Designed Mesoporous Carbon-Supported Catalytic Layer. *Renew. Energy* **2025**, *246*, 122885. https://doi.org/10.1016/j.renene.2025.122885.
(97) Ignaszak, A.; Ye, S.; Gyenge, E. A Study of the Catalytic Interface for O_2 Electroreduction on Pt: The Interaction between Carbon Support Meso/Microstructure and Ionomer (Nafion) Distribution. *J. Phys. Chem. C* **2009**, *113* (1), 298–307. https://doi.org/10.1021/jp8060398.
(98) Yang, B.; Hao, C.; Liao, Q.; Liu, J.; Yan, B.; Lin, M.; Shen, P. K.; Feng, L.; Tian, Z. Q. Atomic Layer Deposition of Pt Nanoparticles Grown onto 3D B-Doped Graphene as an Efficient Ultra-Low Pt Loading Catalyst Layer for PEMFC. *J. Colloid Interface Sci.* **2025**, *683*, 460–473. https://doi.org/10.1016/j.jcis.2024.12.176.
(99) Arici, E.; Kaplan, B. Y.; Mert, A. M.; Alkan Gursel, S.; Kinayyigit, S. An Effective Electrocatalyst Based on Platinum Nanoparticles Supported with Graphene Nanoplatelets and Carbon Black Hybrid for PEM Fuel Cells. *Int. J. Hydrog. Energy* **2019**, *44* (27), 14175–14183. https://doi.org/10.1016/j.ijhydene.2018.11.210.

(100) You, C.; Wang, L.; Huang, Y.; Jiang, X.; Li, X.; Wang, C.; Hua, Y.; Wang, X.; Liao, S. High Porosity Nitrogen and Phosphorous Co-Doped Carbon Nanosheets as an Efficient Catalyst for Oxygen Reduction. *Int. J. Hydrog. Energy* **2018**, *43* (20), 9749–9756. https://doi.org/10.1016/j.ijhydene.2018.03.219.
(101) Li, H.; You, J.; Yuan, S.; Wang, E.; Cheng, X.; Luo, L.; Yan, X.; Shen, S.; Zhang, J. High Oxygen Transport Electrode with Long-Term Stability for High-Power and Low Pt-Loaded Proton Exchange Membrane Fuel Cells. *Nano Res.* **2026**, *19* (7), 94908445. https://doi.org/10.26599/NR.2026.94908445.
(102) Zhang, R.; Chen, L.; Wang, Y.; Sun, G.; You, J.; Li, T.; Tao, W.-Q. Multiscale Study of Carbon Corrosion and Pt Degradation in the Cathode Catalyst Layer and Their Effects on PEMFC Performance Decay over 5000 h Operation. *Chem. Eng. J.* **2025**, *522*, 167960. https://doi.org/10.1016/j.cej.2025.167960.
(103) Ibrahim, F. O.; Kisand, K.; Douglin, J. C.; Sarapuu, A.; Kikas, A.; Käärik, M.; Kozlova, J.; Aruväli, J.; Treshchalov, A.; Leis, J.; Kisand, V.; Kukli, K.; Yassin, K.; Dekel, D. R.; Tammeveski, K. Ionothermal Synthesis of Mesoporous FeNC Electrocatalysts for High-Performance Anion-Exchange Membrane Fuel Cells. *Chem. Eng. J.* **2025**, *510*, 161560. https://doi.org/10.1016/j.cej.2025.161560.
(104) Choudhury, D.; Das, B.; Sarma, D. D.; Rao, C. N. R. XPS Evidence for Molecular Charge-Transfer Doping of Graphene. *Chem. Phys. Lett.* **2010**, *497* (1–3), 66–69. https://doi.org/10.1016/j.cplett.2010.07.089.
(105) Jukk, K.; Kongi, N.; Rauwel, P.; Matisen, L.; Tammeveski, K. Platinum Nanoparticles Supported on Nitrogen-Doped Graphene Nanosheets as Electrocatalysts for Oxygen Reduction Reaction. *Electrocatalysis* **2016**, *7* (5), 428–440. https://doi.org/10.1007/s12678-016-0322-1.
(106) Wang, H.; Zhou, Y.; Wu, D.; Liao, L.; Zhao, S.; Peng, H.; Liu, Z. Synthesis of Boron-Doped Graphene Monolayers Using the Sole Solid Feedstock by Chemical Vapor Deposition. *Small* **2013**, *9* (8), 1316–1320. https://doi.org/10.1002/smll.201203021.
(107) Shaikhutdinov, Sh. K.; Schildenberger, M.; Noeske, M.; Mestl, G. Platinum Colloid Supported on Graphite: X-Ray Photoelectron Spectroscopy Study. *React. Kinet. Catal. Lett.* **1999**, *67* (1), 129–135. https://doi.org/10.1007/BF02475838.
(108) Brandiele, R.; Zerbetto, M.; Dalconi, M. C.; Rizzi, G. A.; Isse, A. A.; Durante, C.; Gennaro, A. Mesoporous Carbon with Different Density of Thiophenic-Like Functional Groups and Their Effect on Oxygen Reduction. *ChemSusChem* **2019**, *12* (18), 4229–4239. https://doi.org/10.1002/cssc.201901568.
(109) Brandiele, R.; Parnigotto, M.; Mazzucato, M.; Dalconi, M. C.; Bertolotti, F.; Rizzi, G. A.; Sasso, G. D.; Durante, C. The Interplay between Surface Area and Sulfur Doping of Carbon Support on Pt NPs Nucleation and Growth: A Synergistic Enhancement of Catalytic Activity for Oxygen Reduction. *Appl. Catal. B Environ.* **2024**, *344*, 123620. https://doi.org/10.1016/j.apcatb.2023.123620.
(110) Holme, T.; Zhou, Y.; Pasquarelli, R.; O'Hayre, R. First Principles Study of Doped Carbon Supports for Enhanced Platinum Catalysts. *Phys. Chem. Chem. Phys.* **2010**, *12* (32), 9461. https://doi.org/10.1039/b927263a.
(111) Labata, M. F.; Li, G.; Ocon, J.; Chuang, P.-Y. A. Insights on Platinum-Carbon Catalyst Degradation Mechanism for Oxygen Reduction Reaction in Acidic and Alkaline Media. *J. Power Sources* **2021**, *487*, 229356. https://doi.org/10.1016/j.jpowsour.2020.229356.

(112) Gómez-Marín, A. M.; Schouten, K. J. P.; Koper, M. T. M.; Feliu, J. M. Interaction of Hydrogen Peroxide with a Pt(111) Electrode. *Electrochem. Commun.* **2012**, *22*, 153–156. https://doi.org/10.1016/j.elecom.2012.06.016.
(113) Bard, A. J.; Faulkner, L. R. *Electrochemical Methods: Fundamentals and Applications*; Wiley: New York, 1980.
(114) Erikson, H.; Lüsi, M.; Sarapuu, A.; Tammeveski, K.; Solla-Gullón, J.; Feliu, J. M. Oxygen Electroreduction on Carbon-Supported Pd Nanocubes in Acid Solutions. *Electrochim. Acta* **2016**, *188*, 301–308. https://doi.org/10.1016/j.electacta.2015.11.125.
(115) Melke, J.; Schuster, R.; Möbus, S.; Jurzinsky, T.; Elsässer, P.; Heilemann, A.; Fischer, A. Electrochemical Stability of Silica-Templated Polyaniline-Derived Mesoporous N-Doped Carbons for the Design of Pt-Based Oxygen Reduction Reaction Catalysts. *Carbon* **2019**, *146*, 44–59. https://doi.org/10.1016/j.carbon.2019.01.057.
(116) Mittal, V.; Kunz, R.; Fenton, J. H_2O_2 Formation Mechanism in PEMFC. *ECS Trans.* **2006**, *1* (8), 295–301. https://doi.org/10.1149/1.2214562.
(117) Bai, F.; Zhang, Y.; Hou, D.; Chen, J.; Meng, F.; Leung, M. K. H.; Zhou, L.; Zhang, Y.; Zhang, C.; Wang, W.; Hu, J. Mechanism and Preparation Research of Binary Heteroatom Co-Doped (X = N, S, P) Platinum/Carbon Black Electrocatalysts for an Enhanced Oxygen Reduction Reaction *via* a One-Pot Pyrolysis Method. *J. Mater. Chem. A* **2024**, *12* (1), 384–395. https://doi.org/10.1039/D3TA04599D.
(118) Hussain, S.; Kongi, N.; Treshchalov, A.; Kahro, T.; Rähn, M.; Merisalu, M.; Tamm, A.; Sammelselg, V.; Tammeveski, K. Enhanced Oxygen Reduction Reaction Activity and Durability of Pt Nanoparticles Deposited on Graphene-Coated Alumina Nanofibres. *Nanoscale Adv.* **2021**, *3* (8), 2261–2268. https://doi.org/10.1039/D1NA00007A.
(119) Schonvogel, D.; Hülstede, J.; Wagner, P.; Dyck, A.; Agert, C.; Wark, M. Durability of Electrocatalysts for ORR: Pt on Nanocomposite of Reduced Graphene Oxide with FTO versus Pt/C. *J. Electrochem. Soc.* **2018**, *165* (6), F3373–F3382. https://doi.org/10.1149/2.0361806jes.
(120) Shinagawa, T.; Garcia-Esparza, A. T.; Takanabe, K. Insight on Tafel Slopes from a Microkinetic Analysis of Aqueous Electrocatalysis for Energy Conversion. *Sci. Rep.* **2015**, *5* (1), 13801. https://doi.org/10.1038/srep13801.
(121) Han, C.; Chen, Z. The Mechanism Study of Oxygen Reduction Reaction (ORR) on Non-Equivalent P, N Co-Doped Graphene. *Appl. Surf. Sci.* **2020**, *511*, 145382. https://doi.org/10.1016/j.apsusc.2020.145382.
(122) Sun, J.-K.; Pan, Y.-W.; Xu, M.-Q.; Sun, L.; Zhang, S.; Deng, W.-Q.; Zhai, D. Heteroatom Doping Regulates the Catalytic Performance of Single-Atom Catalyst Supported on Graphene for ORR. *Nano Res.* **2024**, *17* (3), 1086–1093. https://doi.org/10.1007/s12274-023-5898-1.
(123) Hong, J.; Kim, S.; Kim, J. First-Principles Study on the d-Band Center of Pt Alloyed with 3d Transition Metals. *J. Korean Phys. Soc.* **2023**, *83* (12), 964–969. https://doi.org/10.1007/s40042-023-00934-3.
(124) Zheng, X.; Wu, J.; Cao, X.; Abbott, J.; Jin, C.; Wang, H.; Strasser, P.; Yang, R.; Chen, X.; Wu, G. N-, P-, and S-Doped Graphene-like Carbon Catalysts Derived from Onium Salts with Enhanced Oxygen Chemisorption for Zn-Air Battery Cathodes. *Appl. Catal. B Environ.* **2019**, *241*, 442–451. https://doi.org/10.1016/j.apcatb.2018.09.054.

(125) Zhang, X.; Wang, Y.; Du, Y.; Qing, M.; Yu, F.; Tian, Z. Q.; Shen, P. K. Highly Active N,S Co-Doped Hierarchical Porous Carbon Nanospheres from Green and Template-Free Method for Super Capacitors and Oxygen Reduction Reaction. *Electrochim. Acta* **2019**, *318*, 272–280. https://doi.org/10.1016/j.electacta.2019.06.081.
(126) Dong, Y.; Wang, Y.; Tian, Z.; Jiang, K.; Li, Y.; Lin, Y.; Oloman, C. W.; Gyenge, E. L.; Su, J.; Chen, L. Enhanced Catalytic Performance of Pt by Coupling with Carbon Defects. *The Innovation* **2021**, *2* (4), 100161. https://doi.org/10.1016/j.xinn.2021.100161.
(127) Sadezky, A.; Muckenhuber, H.; Grothe, H.; Niessner, R.; Pöschl, U. Raman Microspectroscopy of Soot and Related Carbonaceous Materials: Spectral Analysis and Structural Information. *Carbon* **2005**, *43* (8), 1731–1742. https://doi.org/10.1016/j.carbon.2005.02.018.
(128) King, A. A. K.; Davies, B. R.; Noorbehesht, N.; Newman, P.; Church, T. L.; Harris, A. T.; Razal, J. M.; Minett, A. I. A New Raman Metric for the Characterisation of Graphene Oxide and Its Derivatives. *Sci. Rep.* **2016**, *6* (1), 19491. https://doi.org/10.1038/srep19491.
(129) Kouketsu, Y.; Mizukami, T.; Mori, H.; Endo, S.; Aoya, M.; Hara, H.; Nakamura, D.; Wallis, S. A New Approach to Develop the Raman Carbonaceous Material Geothermometer for Low-grade Metamorphism Using Peak Width. *Isl. Arc* **2014**, *23* (1), 33–50. https://doi.org/10.1111/iar.12057.
(130) Li, S.; Xie, H.; Dong, Q.; Jing, S.; Li, T.; Xu, L.; Hu, L. Synthesizing Carbon-Supported, High-Loading, Ultra-Small Pt_3Ni Nanoparticles via Tuning the Surface Electrostatic Effect. *Small Struct.* **2023**, *4* (1), 2200176. https://doi.org/10.1002/sstr.202200176.
(131) Mazzotta, E.; Di Giulio, T.; Mastronardi, V.; Pompa, P. P.; Moglianetti, M.; Malitesta, C. Bare Platinum Nanoparticles Deposited on Glassy Carbon Electrodes for Electrocatalytic Detection of Hydrogen Peroxide. *ACS Appl. Nano Mater.* **2021**, *4* (8), 7650–7662. https://doi.org/10.1021/acsanm.1c00754.
(132) Erikson, H.; Sarapuu, A.; Alexeyeva, N.; Tammeveski, K.; Solla-Gullón, J.; Feliu, J. M. Electrochemical Reduction of Oxygen on Palladium Nanocubes in Acid and Alkaline Solutions. *Electrochim. Acta* **2012**, *59*, 329–335. https://doi.org/10.1016/j.electacta.2011.10.074.
(133) Solla-Gullón, J.; Vidal-Iglesias, F. J.; Herrero, E.; Feliu, J. M.; Aldaz, A. CO Monolayer Oxidation on Semi-Spherical and Preferentially Oriented (100) and (111) Platinum Nanoparticles. *Electrochem. Commun.* **2006**, *8* (1), 189–194. https://doi.org/10.1016/j.elecom.2005.11.008.
(134) Prass, S.; St-Pierre, J.; Klingele, M.; Friedrich, K. A.; Zamel, N. Hydrogen Oxidation Artifact During Platinum Oxide Reduction in Cyclic Voltammetry Analysis of Low-Loaded PEMFC Electrodes. *Electrocatalysis* **2021**, *12* (1), 45–55. https://doi.org/10.1007/s12678-020-00627-6.
(135) Gasteiger, H. A.; Kocha, S. S.; Sompalli, B.; Wagner, F. T. Activity Benchmarks and Requirements for Pt, Pt-Alloy, and Non-Pt Oxygen Reduction Catalysts for PEMFCs. *Appl. Catal. B Environ.* **2005**, *56* (1–2), 9–35. https://doi.org/10.1016/j.apcatb.2004.06.021.
(136) Schonvogel, D.; Hülstede, J.; Wagner, P.; Kruusenberg, I.; Tammeveski, K.; Dyck, A.; Agert, C.; Wark, M. Stability of Pt Nanoparticles on Alternative Carbon Supports for Oxygen Reduction Reaction. *J. Electrochem. Soc.* **2017**, *164* (9), F995–F1004. https://doi.org/10.1149/2.1611709jes.

(137) Zhang, S.; Fu, T.; Li, J.; Peng, Y.; Zhao, J. Platinum Nanoparticles Dispersed on High-Surface-Area Roelike Nitrogen-Doped Mesoporous Carbon for Oxygen Reduction Reaction. *ACS Appl. Energy Mater.* **2018**, *1* (11), 6198–6207. https://doi.org/10.1021/acsaem.8b01242.

(138) Zhu, J.; He, G.; Liang, L.; Wan, Q.; Shen, P. K. Direct Anchoring of Platinum Nanoparticles on Nitrogen and Phosphorus-Dual-Doped Carbon Nanotube Arrays for Oxygen Reduction Reaction. *Electrochim. Acta* **2015**, *158*, 374–382. https://doi.org/10.1016/j.electacta.2015.01.173.

(139) Lu, B.-A.; Shen, L.-F.; Liu, J.; Zhang, Q.; Wan, L.-Y.; Morris, D. J.; Wang, R.-X.; Zhou, Z.-Y.; Li, G.; Sheng, T.; Gu, L.; Zhang, P.; Tian, N.; Sun, S.-G. Structurally Disordered Phosphorus-Doped Pt as a Highly Active Electrocatalyst for an Oxygen Reduction Reaction. *ACS Catal.* **2021**, *11* (1), 355–363. https://doi.org/10.1021/acscatal.0c03137.

(140) Zehtab Yazdi, A.; Roberts, E. P. L.; Sundararaj, U. Nitrogen/Sulfur Co-Doped Helical Graphene Nanoribbons for Efficient Oxygen Reduction in Alkaline and Acidic Electrolytes. *Carbon* **2016**, *100*, 99–108. https://doi.org/10.1016/j.carbon.2015.12.096.

(141) Perini, L.; Durante, C.; Favaro, M.; Perazzolo, V.; Agnoli, S.; Schneider, O.; Granozzi, G.; Gennaro, A. Metal–Support Interaction in Platinum and Palladium Nanoparticles Loaded on Nitrogen-Doped Mesoporous Carbon for Oxygen Reduction Reaction. *ACS Appl. Mater. Interfaces* **2015**, *7* (2), 1170–1179. https://doi.org/10.1021/am506916y.

(142) Geboes, B.; Ustarroz, J.; Sentosun, K.; Vanrompay, H.; Hubin, A.; Bals, S.; Breugelmans, T. Electrochemical Behavior of Electrodeposited Nanoporous Pt Catalysts for the Oxygen Reduction Reaction. *ACS Catal.* **2016**, *6* (9), 5856–5864. https://doi.org/10.1021/acscatal.6b00668.

(143) Fortunato, G. V.; De Lima, F.; Maia, G. Oxygen-Reduction Reaction Strongly Electrocatalyzed by Pt Electrodeposited onto Graphene or Graphene Nanoribbons. *J. Power Sources* **2016**, *302*, 247–258. https://doi.org/10.1016/j.jpowsour.2015.10.069.

(144) Brandiele, R.; Durante, C.; Zerbetto, M.; Vicentini, N.; Kosmala, T.; Badocco, D.; Pastore, P.; Rizzi, G. A.; Isse, A. A.; Gennaro, A. Probing the Correlation between Pt-Support Interaction and Oxygen Reduction Reaction Activity in Mesoporous Carbon Materials Modified with Pt-N Active Sites. *Electrochim. Acta* **2018**, *277*, 287–300. https://doi.org/10.1016/j.electacta.2018.04.182.

(145) Liu, T.; Li, M.; Bo, X.; Zhou, M. Designing Iron Carbide Embedded Isolated Boron (B) and Nitrogen (N) Atoms Co-Doped Porous Carbon Fibers Networks with Tiny Amount of B N Bonds as High-Efficiency Oxygen Reduction Reaction Catalysts. *J. Colloid Interface Sci.* **2019**, *533*, 709–722. https://doi.org/10.1016/j.jcis.2018.08.087.

(146) Shrestha, S.; Asheghi, S.; Timbro, J.; Mustain, W. E. Effects of Pore Structure in Nitrogen Functionalized Mesoporous Carbon on Oxygen Reduction Reaction Activity of Platinum Nanoparticles. *Carbon* **2013**, *60*, 28–40. https://doi.org/10.1016/j.carbon.2013.03.053.

(147) Martin, J.; Melke, J.; Njel, C.; Schökel, A.; Büttner, J.; Fischer, A. Electrochemical Stability of Platinum Nanoparticles Supported on *N* -Doped Hydrothermal Carbon Aerogels as Electrocatalysts for the Oxygen Reduction Reaction. *ChemElectro Chem* **2021**, *8* (24), 4835–4847. https://doi.org/10.1002/celc.202101162.

(148) Melke, J.; Peter, B.; Habereder, A.; Ziegler, J.; Fasel, C.; Nefedov, A.; Sezen, H.; Wöll, C.; Ehrenberg, H.; Roth, C. Metal–Support Interactions of Platinum Nanoparticles Decorated N-Doped Carbon Nanofibers for the Oxygen Reduction Reaction. *ACS Appl. Mater. Interfaces* **2016**, *8* (1), 82–90. https://doi.org/10.1021/acsami.5b06225.
(149) Cheng, Y.; Lu, H.; Zhang, K.; Yang, F.; Dai, W.; Liu, C.; Dong, H.; Zhang, X. Fabricating Pt-Decorated Three Dimensional N-Doped Carbon Porous Microspherical Cavity Catalyst for Advanced Oxygen Reduction Reaction. *Carbon* **2018**, *128*, 38–45. https://doi.org/10.1016/j.carbon.2017.10.102.
(150) Hoque, Md. A.; Hassan, F. M.; Seo, M.-H.; Choi, J.-Y.; Pritzker, M.; Knights, S.; Ye, S.; Chen, Z. Optimization of Sulfur-Doped Graphene as an Emerging Platinum Nanowires Support for Oxygen Reduction Reaction. *Nano Energy* **2016**, *19*, 27–38. https://doi.org/10.1016/j.nanoen.2015.11.004.
(151) Huang, G.; Ali, A.; He, S.; Luo, S.; Shen, P. K.; Zhu, J. Celery-like Nitrogen and Phosphorous Co-Doped Carbon Nanofiber Frameworks Supporting Oxygen Reduction and Methanol Oxidation Electrocatalysis. *Int. J. Hydrog. Energy* **2023**, *48* (24), 8877–8887. https://doi.org/10.1016/j.ijhydene.2022.11.328.
(152) Durante, C. Metal–Carbon Interaction in Metal Nanoparticles and Implication in the Electrocatalysis of Oxygen Reduction. *Curr. Opin. Electrochem.* **2022**, *36*, 101119. https://doi.org/10.1016/j.coelec.2022.101119.
(153) Bhaskaran, R.; Chetty, R. One-Pot Room Temperature Synthesis of Nitrogen-Doped Graphene and Its Application as Catalyst Support for ORR in PEMFCs. *ACS Appl. Energy Mater.* **2024**, *7* (2), 390–402. https://doi.org/10.1021/acsaem.3c01956.
(154) Kisand, K.; Sarapuu, A.; Douglin, J. C.; Kikas, A.; Käärik, M.; Kozlova, J.; Aruväli, J.; Treshchalov, A.; Leis, J.; Kisand, V.; Kukli, K.; Dekel, D. R.; Tammeveski, K. Hierarchically Porous Fe−N−C Single-Atom Catalysts via Ionothermal Synthesis for Oxygen Reduction Reaction. *ChemSusChem* **2025**, *18* (2), e202401332. https://doi.org/10.1002/cssc.202401332.
(155) You, J.; Hu, J.; Zheng, Z.; Li, H.; Luo, L.; Cheng, X.; Yan, X.; Shen, S.; Zhang, J. Porous Carbon Supports for Low-Pt Proton-Exchange Membrane Fuel Cells. *Electrochem. Energy Rev.* **2025**, *8* (1), 22. https://doi.org/10.1007/s41918-025-00259-8.
(156) Ferro, G.; Roiron, C.; Wang, H.; Braaten, J.; Stühmeier, B. M.; Johnston, C.; Cheng, L.; Zenyuk, I. V.; Atanassov, P. Designer Electrocatalysts for the Oxygen Reduction Reaction with Controlled Platinum Nanoparticle Locality. *Adv. Energy Mater.* **2025**, *15* (25), 2403165. https://doi.org/10.1002/aenm.202403165.
(157) Padgett, E.; Andrejevic, N.; Liu, Z.; Kongkanand, A.; Gu, W.; Moriyama, K.; Jiang, Y.; Kumaraguru, S.; Moylan, T. E.; Kukreja, R.; Muller, D. A. Editors' Choice—Connecting Fuel Cell Catalyst Nanostructure and Accessibility Using Quantitative Cryo-STEM Tomography. *J. Electrochem. Soc.* **2018**, *165* (3), F173–F180. https://doi.org/10.1149/2.0541803jes.
(158) Bayindir, Z.; Duchesne, P. N.; Cook, S. C.; MacDonald, M. A.; Zhang, P. X-Ray Spectroscopy Studies on the Surface Structural Characteristics and Electronic Properties of Platinum Nanoparticles. *J. Chem. Phys.* **2009**, *131* (24), 244716. https://doi.org/10.1063/1.3276917.
(159) Maillard, F.; Schreier, S.; Hanzlik, M.; Savinova, E. R.; Weinkauf, S.; Stimming, U. Influence of Particle Agglomeration on the Catalytic Activity of Carbon-

Supported Pt Nanoparticles in CO Monolayer Oxidation. *Phys. Chem. Chem. Phys.* **2005**, *7* (2), 385–393. https://doi.org/10.1039/B411377B.

(160) Zhang, D.; Ding, R.; Shi, S.; He, Y. Efficient Four-Electron Transfer Platinum-Based Oxygen Reduction Catalysts: A Mini Review. *Int. J. Hydrog. Energy* **2023**, *48* (78), 30391–30406. https://doi.org/10.1016/j.ijhydene.2023.04.161.

(161) Gribov, E. N.; Kuznetsov, A. N.; Golovin, V. A.; Krasnikov, D. V.; Kuznetsov, V. L. Effect of Modification of Multi-Walled Carbon Nanotubes with Nitrogen-Containing Polymers on the Electrochemical Performance of Pt/CNT Catalysts in PEMFC. *Mater. Renew. Sustain. Energy* **2019**, *8* (1), 7. https://doi.org/10.1007/s40243-019-0143-2.

(162) Qiao, Z.; Hwang, S.; Li, X.; Wang, C.; Samarakoon, W.; Karakalos, S.; Li, D.; Chen, M.; He, Y.; Wang, M.; Liu, Z.; Wang, G.; Zhou, H.; Feng, Z.; Su, D.; Spendelow, J. S.; Wu, G. 3D Porous Graphitic Nanocarbon for Enhancing the Performance and Durability of Pt Catalysts: A Balance between Graphitization and Hierarchical Porosity. *Energy Environ. Sci.* **2019**, *12* (9), 2830–2841. https://doi.org/10.1039/C9EE01899A.

(163) Fu, S.; Zhu, C.; Song, J.; Engelhard, M. H.; Xia, H.; Du, D.; Lin, Y. Kinetically Controlled Synthesis of Pt-Based One-Dimensional Hierarchically Porous Nanostructures with Large Mesopores as Highly Efficient ORR Catalysts. *ACS Appl. Mater. Interfaces* **2016**, *8* (51), 35213–35218. https://doi.org/10.1021/acsami.6b11537.

(164) Zhang, H.; Li, H.; Zhang, X.; Yu, S.; Wang, S.; Sun, G. Enhanced Metal-Support Interaction of Nitrogen-Doped Carbon Supported Pt Nanoparticles with High Activity for Electrocatalytic Oxygen Reduction Reaction. *Carbon Neutrality* **2025**, *4* (1), 10. https://doi.org/10.1007/s43979-025-00122-1.

(165) Xiong, Y.; Ma, Y.; Zou, L.; Han, S.; Chen, H.; Wang, S.; Gu, M.; Shen, Y.; Zhang, L.; Xia, Z.; Li, J.; Yang, H. N-Doping Induced Tensile-Strained Pt Nanoparticles Ensuring an Excellent Durability of the Oxygen Reduction Reaction. *J. Catal.* **2020**, *382*, 247–255. https://doi.org/10.1016/j.jcat.2019.12.025.

(166) Cosenza, A.; Roiron, C.; Ferro, G.; Atanassov, P. Nitrogen-Doped Carbon Supports for Pt-Based Fuel Cell Electrocatalysts. *Chem. Eng. J.* **2025**, *512*, 162816. https://doi.org/10.1016/j.cej.2025.162816.

(167) Izydorczyk, W.; Izydorczyk, J. Structure, Surface Morphology, Chemical Composition, and Sensing Properties of SnO_2 Thin Films in an Oxidizing Atmosphere. *Sensors* **2021**, *21* (17), 5741. https://doi.org/10.3390/s21175741.

(168) Li, S.; Liu, J.; Liang, J.; Lin, Z.; Liu, X.; Chen, Y.; Lu, G.; Wang, C.; Wei, P.; Han, J.; Huang, Y.; Wu, G.; Li, Q. Tuning Oxygen Vacancy in SnO_2 Inhibits Pt Migration and Agglomeration towards High-Performing Fuel Cells. *Appl. Catal. B Environ.* **2023**, *320*, 122017. https://doi.org/10.1016/j.apcatb.2022.122017.

(169) Hussain, S.; Kongi, N.; Erikson, H.; Rähn, M.; Merisalu, M.; Matisen, L.; Paiste, P.; Aruväli, J.; Sammelselg, V.; Estudillo-Wong, L. A.; Tammeveski, K.; Alonso-Vante, N. Platinum Nanoparticles Photo-Deposited on SnO_2-C Composites: An Active and Durable Electrocatalyst for the Oxygen Reduction Reaction. *Electrochim. Acta* **2019**, *316*, 162–172. https://doi.org/10.1016/j.electacta.2019.05.104.

(170) Ganassin, A.; Colic, V.; Tymoczko, J.; Bandarenka, A. S.; Schuhmann, W. Non-Covalent Interactions in Water Electrolysis: Influence on the Activity of Pt(111) and Iridium Oxide Catalysts in Acidic Media. *Phys. Chem. Chem. Phys.* **2015**, *17* (13), 8349–8355. https://doi.org/10.1039/C4CP04791E.

(171) Spasov, D. D.; Ivanova, N. A.; Pushkarev, A. S.; Pushkareva, I. V.; Presnyakova, N. N.; Chumakov, R. G.; Presnyakov, M. Yu.; Grigoriev, S. A.; Fateev, V. N. On the Influence of Composition and Structure of Carbon-Supported Pt-SnO_2 Hetero-Clusters onto Their Electrocatalytic Activity and Durability in PEMFC. *Catalysts* **2019**, *9* (10), 803. https://doi.org/10.3390/catal9100803.

(172) Rabis, A.; Binninger, T.; Fabbri, E.; Schmidt, T. J. Impact of Support Physicochemical Properties on the CO Oxidation and the Oxygen Reduction Reaction Activity of Pt/SnO_2 Electrocatalysts. *J. Phys. Chem. C* **2018**, *122* (9), 4739–4746. https://doi.org/10.1021/acs.jpcc.7b09976.

(173) Hussain, S.; Erikson, H.; Kongi, N.; Rähn, M.; Merisalu, M.; Tamm, A.; Sammelselg, V.; Alonso-Vante, N.; Tammeveski, K. High Oxygen Reduction Reaction Activity and Durability of Pt Catalyst Photo-Deposited on SnO_2-Coated and Uncoated Multi-Walled Carbon Nanotubes. *J. Electroanal. Chem.* **2021**, *896*, 115147. https://doi.org/10.1016/j.jelechem.2021.115147.

(174) Sun, S.; Zhang, G.; Geng, D.; Chen, Y.; Banis, M. N.; Li, R.; Cai, M.; Sun, X. Direct Growth of Single-Crystal Pt Nanowires on Sn@CNT Nanocable: 3D Electrodes for Highly Active Electrocatalysts. *Chem. Eur. J.* **2010**, *16* (3), 829–835. https://doi.org/10.1002/chem.200902320.

(175) Li, S.-Z.; Lin, Z.-J.; Chen, Q.-A.; Cai, Z.; Li, Q. Electrochemical-Method-Induced Strong Metal-Support Interaction in Pt-CNT@SnO_2 for CO-Tolerant Hydrogen Oxidation Reaction. *J. Electrochem.* **2024**, *30* (12). https://doi.org/10.61558/2993-074X.3474.

(176) Higuchi, E.; Miyata, K.; Takase, T.; Inoue, H. Ethanol Oxidation Reaction Activity of Highly Dispersed Pt/SnO_2 Double Nanoparticles on Carbon Black. *J. Power Sources* **2011**, *196* (4), 1730–1737. https://doi.org/10.1016/j.jpowsour.2010.10.008.

(177) Borbáth, I.; Gubán, D.; Pászti, Z.; Sajó, I. E.; Drotár, E.; De La Fuente, J. L. G.; Herranz, T.; Rojas, S.; Tompos, A. Controlled Synthesis of Pt_3Sn/C Electrocatalysts with Exclusive Sn–Pt Interaction Designed for Use in Direct Methanol Fuel Cells. *Top. Catal.* **2013**, *56* (11), 1033–1046. https://doi.org/10.1007/s11244-013-0067-5.

(178) Đurasović, I.; Peter, R.; Dražić, G.; Faraguna, F.; Anelić, R.; Marciuš, M.; Jurkin, T.; Mohaček Grošev, V.; Gracheva, M.; Klencsár, Z.; Ivanda, M.; Štefanić, G.; Gotić, M. Catalytically Active Oxidized PtO_x Species on SnO_2 Supports Synthesized via Anion Exchange Reaction for 4-Nitrophenol Reduction. *Nanomaterials* **2025**, *15* (15), 1159. https://doi.org/10.3390/nano15151159.

(179) Ruiz Camacho, B.; Morais, C.; Valenzuela, M. A.; Alonso-Vante, N. Enhancing Oxygen Reduction Reaction Activity and Stability of Platinum via Oxide-Carbon Composites. *Catal. Today* **2013**, *202*, 36–43. https://doi.org/10.1016/j.cattod.2012.03.033.

(180) Jia, J.; Wang, H.; Ji, S.; Yang, H.; Li, X.; Wang, R. SnO_2-Embedded Worm-like Carbon Nanofibers Supported Pt Nanoparticles for Oxygen Reduction Reaction. *Electrochim. Acta* **2014**, *141*, 13–19. https://doi.org/10.1016/j.electacta.2014.07.020.

(181) Gu, S.; Huang, H.-Y.; Lin, Y.-C.; Hsieh, C.-A.; Panda, P. K.; Chang, J.-K.; Hsieh, C.-T. High-Entropy Alloys with Low Platinum Content: Novel Catalysts for Oxygen Reduction and Evolution Reactions. *Emergent Mater.* **2025**. https://doi.org/10.1007/s42247-025-01011-0.

(182) Tiido, K.; Alexeyeva, N.; Couillard, M.; Bock, C.; MacDougall, B. R.; Tammeveski, K. Graphene–TiO_2 Composite Supported Pt Electrocatalyst for Oxygen Reduction Reaction. *Electrochim. Acta* **2013**, *107*, 509–517. https://doi.org/10.1016/j.electacta.2013.05.155.

(183) Zhang, K.; Feng, C.; He, B.; Dong, H.; Dai, W.; Lu, H.; Zhang, X. An Advanced Electrocatalyst of Pt Decorated SnO_2/C Nanofibers for Oxygen Reduction Reaction. *J. Electroanal. Chem.* **2016**, *781*, 198–203. https://doi.org/10.1016/j.jelechem.2016.11.002.

(184) Rivera Rocabado, D. S.; Ishimoto, T.; Koyama, M. The Effect of SnO_2(110) Supports on the Geometrical and Electronic Properties of Platinum Nanoparticles. *SN Appl. Sci.* **2019**, *1* (11), 1485. https://doi.org/10.1007/s42452-019-1478-0.

(185) Krasnova, A.; Nechitailov, A. A.; Pelageikina, A.; Glebova, N. V. Differences in the Electrochemical Behavior of Vulcan XC-72 Carbon Black and Glassy Carbon after Prolonged Potential Cycling. *Electrochem. Commun.* **2023**, *155*, 107578. https://doi.org/10.1016/j.elecom.2023.107578.

(186) Castanheira, L.; Dubau, L.; Mermoux, M.; Berthomé, G.; Caqué, N.; Rossinot, E.; Chatenet, M.; Maillard, F. Carbon Corrosion in Proton-Exchange Membrane Fuel Cells: From Model Experiments to Real-Life Operation in Membrane Electrode Assemblies. *ACS Catal.* **2014**, *4* (7), 2258–2267. https://doi.org/10.1021/cs500449q.

(187) Jiménez-Morales, I.; Cavaliere, S.; Jones, D.; Rozière, J. Strong Metal–Support Interaction Improves Activity and Stability of Pt Electrocatalysts on Doped Metal Oxides. *Phys. Chem. Chem. Phys.* **2018**, *20* (13), 8765–8772. https://doi.org/10.1039/C8CP00176F.

(188) Promsawan, N.; Saipanya, S.; Rattanakansang, S.; Themsirimongkon, S.; Inceesungvorn, B.; Waenkaew, P. Modification of Various Carbons with Various Metal Oxides and Noble Metal Compositions as Electrocatalysts for Ethanol Oxidation. *Compos. Interfaces* **2020**, *27* (11), 1023–1045. https://doi.org/10.1080/09276440.2020.1722522.

9. SUMMARY IN ESTONIAN

Hapniku elektrokatalüütiline redutseerumine uudsetele katalüsaatorikandjatele sadestatud Pt nanoosakestel

Selles doktoritöös uuriti süsiniku dopeerimise mõju plaatina nanoosakeste hapniku elektrokeemilise redutseerumise aktiivsusele kasutades erinevaid füüsikalis-keemilisi ja elektrokeemilisi meetodeid. Hapniku redutseerumise reaktsiooni uuriti 0,1 M $HClO_4$ lahuses, kasutades pöörlevaketaselektroodi meetodit ja üherakulist prootonivahetusmembraaniga kütuseelementi. Süstemaatiliselt uuriti kommertsiaalse päritoluga erinevate heteroaatomitega dopeeritud grafeenipulbrite mõju keemiliselt ja elektrokeemiliselt sadestatud plaatina nanoosakeste aktiivsusele. Lisaks uuriti lämmastikuga dopeeritud poorse süsiniku mõju ning tina(IV)-oksiidiga osaliselt kaetud süsiniknanotorude mõju keemiliselt sadestatud Pt nanoosakeste elektrokatalüütilisele aktiivsusele.

Doktoritöö esimeses osas sadestati plaatina nanoosakesed elektrokeemiliselt kommertsiaalselt kättesaadavatele heteroaatomitega dopeeritud grafeenipulbritele kasutades kronoamperomeetrilist meetodit, kus elektroodi hoiti 1 mM H_2PtCl_6 lahuses -0,3 V_{SCE} juures 30 s. Võrdluseks sadestati Pt ka kommertsiaalsele Vulcan-süsinikule. Selles töö osas selgus, et kahe heteroaatomiga kaasdopeeritud grafeenile sadestatud Pt nanoosakeste eriaktiivsus on madalam, kui ühe heteroaatomiga dopeeritud grafeenile sadestatu, erandiks ainult N-dopeeritud grafeenile sadestatu. Booriga dopeeritud grafeenile sadestatud Pt nanoosakesed näitasid suurimat eriaktiivsust ning boori ja lämmastikuga kaasdopeeritud grafeenile sadestatud Pt omas suurimat massaktiivsust. Lisaks lämmastiku ja booriga kaasdopeeritud grafeenile sadestatud Pt nanoosakesed näitasid suuremat elektrokeemilist stabiilsust, kui eraldi N-dopeeritud ja B-dopeeritud grafeenipulbritele sadestatu, viidates sünergilisele efektile.

Töö teises osas valmistati Pt nanoosakesed keemilise meetodiga kommertsiaalse päritoluga heteroaatomitega dopeeritud grafeenipulbritele. Võrdluseks sadestati Pt ka Vulcan-süsinikule. Selles töö osas tuvastati, et kahe heteroaatomiga dopeeritud grafeenile sadestatud Pt nanoosakesed omasid suuremat eriaktiivsust kui ühe heteroaatomiga dopeeritud grafeenile sadestatud Pt. Lämmastiku ja väävliga kaasdopeeritud grafeenile kantud Pt nanoosakesed näitasid suurimat eriaktiivsust, kusjuures ainult väävliga dopeeritud grafeenile sadestatud Pt oli madalaima eriaktiivsusega. Eeladsorbeeritud CO oksüdeerimise profiilid näitasid tugevat katalüsaatorikandja mõju Pt aktiivsusele.

Doktoritöö kolmandas osas sadestati plaatina nanoosakesed lämmastikuga dopeeritud poorsele süsinikule, kasutades keemilist meetodit. Uuriti sadestusprotseduuri, kus Pt nanoosakesed valmistati nii süsinikkandja juuresolekul kui ka kanti süsinikule pärast sünteesi. Võrdluseks kasutati kommertsiaalset 46% Pt/C katalüsaatorit. Katalüsaator, millele lisati süsinik pärast nanoosakeste valmistamist, näitas suuremat eriaktiivsust, kuid süsiniku juuresolekul valmistatud materjal omas suuremat võimsust üherakulises kütuseelemendis. See vihjab, et Pt nano-

osakeste paiknemine süsiniku poorides omas suurt mõju elektrokatalüütilisele aktiivsusele.

Töö viimases osas kasutati katalüsaatorikandjana süsiniknanotorusid, millele oli kantud SnO_2. Võrdluseks kasutati kommertsiaalset 20% Pt/C katalüsaatorit. Valmistatud katalüsaatori eriaktiivsus oli madalam kui Pt/C katalüsaatoril, kuid massaktiivsus suurem. Lisaks omas SnO_2 lisandiga katalüsaator suuremat stabiilsust kuna testi jooksul vähenes elektroaktiivne pindala vähem kui kommertsiaalsel katalüsaatoril.

Kõik doktoritöös uuritud elektrokatalüsaatorid katalüüsisid hapniku redutseerumist neljaelektronilise reaktsioonitee kaudu, kusjuures kiirust limiteerivaks staadiumiks oli esimese elektroni ülekanne hapniku molekulile. Kõikide valmistatud katalüsaatorite Tafeli tõusu väärtused madalatel voolutihedustel oli ca -60 mV, kinnitades, et hapniku redutseerumise kineetika valmistatud materjalidel on kirjanduses esitatutega kooskõlas. Seega leiti, et süsiniku funktsionaliseerimine mõjutab sadestatavate Pt nanoosakeste aktiivsust ehk katalüsaatorikandja mõjusid ei tohi jätta tähelepanuta kui valmistatakse Pt/C katalüsaatoreid hapniku elektrokeemiliseks redutseerumiseks.

10. ACKNOWLEDGEMENTS

Above all, I would like to express my deepest gratitude to my supervisors, Dr. Heiki Erikson and Professor Kaido Tammeveski, for their unwavering support throughout this entire journey. Not only have they positively impacted the outcome of this thesis but also on my life and to the scientist I have become.

I also want to thank my lab mates throughout the years who have made long days in the lab all the more fun, who have made conferences memorable, and who have listened to no less than a thousand hours of Taylor Swift in the lab with me. I especially want to thank those who I have been blessed to be co-authors with; Dr. Jaana Lilloja-Lensment, Dr. Kaarel Kisand, Dr. Sajid Hussain.

I want to thank all of my co-authors from other institutes who have contributed to my work and have made things even more pink when they could: Aivar Tarre, Markus Otsus, Dr. Jekaterina Kozlova, Prof. Kaupo Kukli, Dr. Arvo Kikas, Prof. Vambola Kisand, Peeter Ritslaid, Dr. Helle-Mai Piirsoo, Dr. Aile Tamm, Dr. Alexey Treshchalov, Dr. Maike Käärik, Dr. Jaan Leis and Dr. Jaan Aruväli.

Finally, I would like to thank my family and friends for their encouragement throughout my studies. Your love and support means the world to me, and I could not have made it this far without such an amazing support system. I love you more! Nawnaw, Mom, Dan, and Debi, thank you for trusting me to make the decision to move halfway across the world. J, Brent, Drew, and Jordan, thank you for allowing me to still be a part of your big life events even though I am miles away. Laura, thank you for standing by my side through all of the fun and stressful moments.

The work in this thesis was financially supported by the Estonian Research Council (grants PRG723 and PRG2569) and the Estonian Ministry of Education and Research (TK210, Centre of Excellence in Sustainable Green Hydrogen and Energy Technology).

PUBLICATIONS

CURRICULUM VITAE

Name: Raegan Danielle Chambers
Birthdate: June 26th, 1997
Citizenship: American
Address: Ravila 14a, 50411 Tartu, Estonia
E-mail: raegandchambers@gmail.com

Education:

2022–	University of Tartu, PhD (Chemistry)
2020–2022	University of Tartu, MSc (Excellence in Analytical Chemistry)
2021–2022	Åbo Akademi University, MSc (Excellence in Analytical Chemistry)
2015–2019	Oklahoma State University, BSc (Chemistry)

Professional Experience:

2022–	Junior research fellow, Tartu University, Institute of Chemistry
2019–2020	Quality assurance analyst, Paycom, USA

Major scientific publications:

1. **Chambers, R.;** Hussain, S.; Kozlova, J.; Kukli, K.; Ritslaid, P.; Kikas, A.; Kisand, V.; Erikson, H.; Tammeveski, K. Pt Nanoparticles Electrochemically Deposited onto Heteroatom-Doped Graphene Supports as Electrocatalysts for ORR in Acid Media. J. Electrochem. Soc. 2024, 171 (9), 096506. https://doi.org/10.1149/1945-7111/ad7296.
2. **Chambers, R**.; Piirsoo, H.-M.; Tamm, A.; Kozlova, J.; Kukli, K.; Ritslaid, P.; Treshchalov, A.; Erikson, H.; Tammeveski, K. Heteroatom-Doped Graphene-Supported Pt Nanoparticles as Electrocatalysts for Proton Exchange Membrane Fuel Cells. ACS Appl. Nano Mater. 2024, 7, 5943–5955. https://doi.org/10.1021/acsanm.3c05713.
3. **Chambers, R**.; Tarre, A.; Otsus, M.; Kozlova, J.; Kukli, K.; Kikas, A.; Kisand, V.; Erikson, H.; Tammeveski, K. Platinum Nanoparticles Supported on Atomic Layer Deposited SnO_2 Decorated Multiwalled Carbon Nanotubes as the Electrocatalyst for the Oxygen Reduction Reaction. Catalysts 2025, 15 (11), 1052. https://doi.org/10.3390/catal15111052.

ELULOOKIRJELDUS

Nimi: Raegan Danielle Chambers
Sünniaeg: 26. juuni 1997
Kodakondsus: Ameerika
Aadress: Ravila 14a, 50411 Tartu, Estonia
E-post: raegandchambers@gmail.com

Haridus:

2022–	Tartu Ülikool, PhD (keemia)
2020–2022	Tartu Ülikool, MSc (analüütiline keemia)
2021–2022	Åbo Akademi, MSc (analüütiline keemia)
2015–2019	Oklahoma Osariigi Ülikool, BSc (keemia)

Töökogemus:

2022–	Tartu Ülikool, Keemia instituut, nooremteadur
2019–2020	Paycom, USA, kvaliteedianalüütik

Oluisemad publikatsioonid:

1. **Chambers, R.;** Hussain, S.; Kozlova, J.; Kukli, K.; Ritslaid, P.; Kikas, A.; Kisand, V.; Erikson, H.; Tammeveski, K. Pt Nanoparticles Electrochemically Deposited onto Heteroatom-Doped Graphene Supports as Electrocatalysts for ORR in Acid Media. J. Electrochem. Soc. 2024, 171 (9), 096506. https://doi.org/10.1149/1945-7111/ad7296.
2. **Chambers, R**.; Piirsoo, H.-M.; Tamm, A.; Kozlova, J.; Kukli, K.; Ritslaid, P.; Treshchalov, A.; Erikson, H.; Tammeveski, K. Heteroatom-Doped Graphene-Supported Pt Nanoparticles as Electrocatalysts for Proton Exchange Membrane Fuel Cells. ACS Appl. Nano Mater. 2024, 7, 5943–5955. https://doi.org/10.1021/acsanm.3c05713.
3. **Chambers, R**.; Tarre, A.; Otsus, M.; Kozlova, J.; Kukli, K.; Kikas, A.; Kisand, V.; Erikson, H.; Tammeveski, K. Platinum Nanoparticles Supported on Atomic Layer Deposited SnO_2 Decorated Multiwalled Carbon Nanotubes as the Electrocatalyst for the Oxygen Reduction Reaction. Catalysts 2025, 15 (11), 1052. https://doi.org/10.3390/catal15111052.

DISSERTATIONES CHIMICAE UNIVERSITATIS TARTUENSIS

1. **Toomas Tamm.** Quantum-chemical simulation of solvent effects. Tartu, 1993, 110 p.
2. **Peeter Burk.** Theoretical study of gas-phase acid-base equilibria. Tartu, 1994, 96 p.
3. **Victor Lobanov.** Quantitative structure-property relationships in large descriptor spaces. Tartu, 1995, 135 p.
4. **Vahur Mäemets.** The ^{17}O and ^{1}H nuclear magnetic resonance study of H_2O in individual solvents and its charged clusters in aqueous solutions of electrolytes. Tartu, 1997, 140 p.
5. **Andrus Metsala.** Microcanonical rate constant in nonequilibrium distribution of vibrational energy and in restricted intramolecular vibrational energy redistribution on the basis of slater's theory of unimolecular reactions. Tartu, 1997, 150 p.
6. **Uko Maran.** Quantum-mechanical study of potential energy surfaces in different environments. Tartu, 1997, 137 p.
7. **Alar Jänes.** Adsorption of organic compounds on antimony, bismuth and cadmium electrodes. Tartu, 1998, 219 p.
8. **Kaido Tammeveski.** Oxygen electroreduction on thin platinum films and the electrochemical detection of superoxide anion. Tartu, 1998, 139 p.
9. **Ivo Leito.** Studies of Brønsted acid-base equilibria in water and non-aqueous media. Tartu, 1998, 101 p.
10. **Jaan Leis.** Conformational dynamics and equilibria in amides. Tartu, 1998, 131 p.
11. **Toonika Rinken.** The modelling of amperometric biosensors based on oxidoreductases. Tartu, 2000, 108 p.
12. **Dmitri Panov.** Partially solvated Grignard reagents. Tartu, 2000, 64 p.
13. **Kaja Orupõld.** Treatment and analysis of phenolic wastewater with microorganisms. Tartu, 2000, 123 p.
14. **Jüri Ivask.** Ion Chromatographic determination of major anions and cations in polar ice core. Tartu, 2000, 85 p.
15. **Lauri Vares.** Stereoselective Synthesis of Tetrahydrofuran and Tetrahydropyran Derivatives by Use of Asymmetric Horner-Wadsworth-Emmons and Ring Closure Reactions. Tartu, 2000, 184 p.
16. **Martin Lepiku.** Kinetic aspects of dopamine D_2 receptor interactions with specific ligands. Tartu, 2000, 81 p.
17. **Katrin Sak.** Some aspects of ligand specificity of P2Y receptors. Tartu, 2000, 106 p.
18. **Vello Pällin.** The role of solvation in the formation of iotsitch complexes. Tartu, 2001, 95 p.
19. **Katrin Kollist.** Interactions between polycyclic aromatic compounds and humic substances. Tartu, 2001, 93 p.

20. **Ivar Koppel.** Quantum chemical study of acidity of strong and superstrong Brønsted acids. Tartu, 2001, 104 p.
21. **Viljar Pihl.** The study of the substituent and solvent effects on the acidity of OH and CH acids. Tartu, 2001, 132 p.
22. **Natalia Palm.** Specification of the minimum, sufficient and significant set of descriptors for general description of solvent effects. Tartu, 2001, 134 p.
23. **Sulev Sild.** QSPR/QSAR approaches for complex molecular systems. Tartu, 2001, 134 p.
24. **Ruslan Petrukhin.** Industrial applications of the quantitative structure-property relationships. Tartu, 2001, 162 p.
25. **Boris V. Rogovoy.** Synthesis of (benzotriazolyl)carboximidamides and their application in relations with *N*- and *S*-nucleophyles. Tartu, 2002, 84 p.
26. **Koit Herodes.** Solvent effects on UV-vis absorption spectra of some solvatochromic substances in binary solvent mixtures: the preferential solvation model. Tartu, 2002, 102 p.
27. **Anti Perkson.** Synthesis and characterisation of nanostructured carbon. Tartu, 2002, 152 p.
28. **Ivari Kaljurand.** Self-consistent acidity scales of neutral and cationic Brønsted acids in acetonitrile and tetrahydrofuran. Tartu, 2003, 108 p.
29. **Karmen Lust.** Adsorption of anions on bismuth single crystal electrodes. Tartu, 2003, 128 p.
30. **Mare Piirsalu.** Substituent, temperature and solvent effects on the alkaline hydrolysis of substituted phenyl and alkyl esters of benzoic acid. Tartu, 2003, 156 p.
31. **Meeri Sassian.** Reactions of partially solvated Grignard reagents. Tartu, 2003, 78 p.
32. **Tarmo Tamm.** Quantum chemical modelling of polypyrrole. Tartu, 2003. 100 p.
33. **Erik Teinemaa.** The environmental fate of the particulate matter and organic pollutants from an oil shale power plant. Tartu, 2003. 102 p.
34. **Jaana Tammiku-Taul.** Quantum chemical study of the properties of Grignard reagents. Tartu, 2003. 120 p.
35. **Andre Lomaka.** Biomedical applications of predictive computational chemistry. Tartu, 2003. 132 p.
36. **Kostyantyn Kirichenko.** Benzotriazole – Mediated Carbon–Carbon Bond Formation. Tartu, 2003. 132 p.
37. **Gunnar Nurk.** Adsorption kinetics of some organic compounds on bismuth single crystal electrodes. Tartu, 2003, 170 p.
38. **Mati Arulepp.** Electrochemical characteristics of porous carbon materials and electrical double layer capacitors. Tartu, 2003, 196 p.
39. **Dan Cornel Fara.** QSPR modeling of complexation and distribution of organic compounds. Tartu, 2004, 126 p.
40. **Riina Mahlapuu.** Signalling of galanin and amyloid precursor protein through adenylate cyclase. Tartu, 2004, 124 p.

41. **Mihkel Kerikmäe.** Some luminescent materials for dosimetric applications and physical research. Tartu, 2004, 143 p.
42. **Jaanus Kruusma.** Determination of some important trace metal ions in human blood. Tartu, 2004, 115 p.
43. **Urmas Johanson.** Investigations of the electrochemical properties of polypyrrole modified electrodes. Tartu, 2004, 91 p.
44. **Kaido Sillar.** Computational study of the acid sites in zeolite ZSM-5. Tartu, 2004, 80 p.
45. **Aldo Oras.** Kinetic aspects of dATPαS interaction with $P2Y_1$ receptor. Tartu, 2004, 75 p.
46. **Erik Mölder.** Measurement of the oxygen mass transfer through the air-water interface. Tartu, 2005, 73 p.
47. **Thomas Thomberg.** The kinetics of electroreduction of peroxodisulfate anion on cadmium (0001) single crystal electrode. Tartu, 2005, 95 p.
48. **Olavi Loog.** Aspects of condensations of carbonyl compounds and their imine analogues. Tartu, 2005, 83 p.
49. **Siim Salmar.** Effect of ultrasound on ester hydrolysis in aqueous ethanol. Tartu, 2006, 73 p.
50. **Ain Uustare.** Modulation of signal transduction of heptahelical receptors by other receptors and G proteins. Tartu, 2006, 121 p.
51. **Sergei Yurchenko.** Determination of some carcinogenic contaminants in food. Tartu, 2006, 143 p.
52. **Kaido Tämm.** QSPR modeling of some properties of organic compounds. Tartu, 2006, 67 p.
53. **Olga Tšubrik.** New methods in the synthesis of multisubstituted hydrazines. Tartu. 2006, 183 p.
54. **Lilli Sooväli.** Spectrophotometric measurements and their uncertainty in chemical analysis and dissociation constant measurements. Tartu, 2006, 125 p.
55. **Eve Koort.** Uncertainty estimation of potentiometrically measured ph and pK_a values. Tartu, 2006, 139 p.
56. **Sergei Kopanchuk.** Regulation of ligand binding to melanocortin receptor subtypes. Tartu, 2006, 119 p.
57. **Silvar Kallip.** Surface structure of some bismuth and antimony single crystal electrodes. Tartu, 2006, 107 p.
58. **Kristjan Saal.** Surface silanization and its application in biomolecule coupling. Tartu, 2006, 77 p.
59. **Tanel Tätte.** High viscosity $Sn(OBu)_4$ oligomeric concentrates and their applications in technology. Tartu, 2006, 91 p.
60. **Dimitar Atanasov Dobchev**. Robust QSAR methods for the prediction of properties from molecular structure. Tartu, 2006, 118 p.
61. **Hannes Hagu**. Impact of ultrasound on hydrophobic interactions in solutions. Tartu, 2007, 81 p.
62. **Rutha Jäger.** Electroreduction of peroxodisulfate anion on bismuth electrodes. Tartu, 2007, 142 p.

63. **Kaido Viht.** Immobilizable bisubstrate-analogue inhibitors of basophilic protein kinases: development and application in biosensors. Tartu, 2007, 88 p.
64. **Eva-Ingrid Rõõm.** Acid-base equilibria in nonpolar media. Tartu, 2007, 156 p.
65. **Sven Tamp.** DFT study of the cesium cation containing complexes relevant to the cesium cation binding by the humic acids. Tartu, 2007, 102 p.
66. **Jaak Nerut.** Electroreduction of hexacyanoferrate(III) anion on Cadmium (0001) single crystal electrode. Tartu, 2007, 180 p.
67. **Lauri Jalukse.** Measurement uncertainty estimation in amperometric dissolved oxygen concentration measurement. Tartu, 2007, 112 p.
68. **Aime Lust.** Charge state of dopants and ordered clusters formation in CaF_2:Mn and CaF_2:Eu luminophors. Tartu, 2007, 100 p.
69. **Iiris Kahn**. Quantitative Structure-Activity Relationships of environmentally relevant properties. Tartu, 2007, 98 p.
70. **Mari Reinik.** Nitrates, nitrites, N-nitrosamines and polycyclic aromatic hydrocarbons in food: analytical methods, occurrence and dietary intake. Tartu, 2007, 172 p.
71. **Heili Kasuk.** Thermodynamic parameters and adsorption kinetics of organic compounds forming the compact adsorption layer at Bi single crystal electrodes. Tartu, 2007, 212 p.
72. **Erki Enkvist.** Synthesis of adenosine-peptide conjugates for biological applications. Tartu, 2007, 114 p.
73. **Svetoslav Hristov Slavov**. Biomedical applications of the QSAR approach. Tartu, 2007, 146 p.
74. **Eneli Härk.** Electroreduction of complex cations on electrochemically polished Bi(*hkl*) single crystal electrodes. Tartu, 2008, 158 p.
75. **Priit Möller.** Electrochemical characteristics of some cathodes for medium temperature solid oxide fuel cells, synthesized by solid state reaction technique. Tartu, 2008, 90 p.
76. **Signe Viggor.** Impact of biochemical parameters of genetically different pseudomonads at the degradation of phenolic compounds. Tartu, 2008, 122 p.
77. **Ave Sarapuu.** Electrochemical reduction of oxygen on quinone-modified carbon electrodes and on thin films of platinum and gold. Tartu, 2008, 134 p.
78. **Agnes Kütt.** Studies of acid-base equilibria in non-aqueous media. Tartu, 2008, 198 p.
79. **Rouvim Kadis.** Evaluation of measurement uncertainty in analytical chemistry: related concepts and some points of misinterpretation. Tartu, 2008, 118 p.
80. **Valter Reedo.** Elaboration of IVB group metal oxide structures and their possible applications. Tartu, 2008, 98 p.
81. **Aleksei Kuznetsov.** Allosteric effects in reactions catalyzed by the cAMP-dependent protein kinase catalytic subunit. Tartu, 2009, 133 p.

82. **Aleksei Bredihhin.** Use of mono- and polyanions in the synthesis of multisubstituted hydrazine derivatives. Tartu, 2009, 105 p.
83. **Anu Ploom.** Quantitative structure-reactivity analysis in organosilicon chemistry. Tartu, 2009, 99 p.
84. **Argo Vonk.** Determination of adenosine A_{2A}- and dopamine D_1 receptor-specific modulation of adenylate cyclase activity in rat striatum. Tartu, 2009, 129 p.
85. **Indrek Kivi.** Synthesis and electrochemical characterization of porous cathode materials for intermediate temperature solid oxide fuel cells. Tartu, 2009, 177 p.
86. **Jaanus Eskusson.** Synthesis and characterisation of diamond-like carbon thin films prepared by pulsed laser deposition method. Tartu, 2009, 117 p.
87. **Marko Lätt.** Carbide derived microporous carbon and electrical double layer capacitors. Tartu, 2009, 107 p.
88. **Vladimir Stepanov.** Slow conformational changes in dopamine transporter interaction with its ligands. Tartu, 2009, 103 p.
89. **Aleksander Trummal.** Computational Study of Structural and Solvent Effects on Acidities of Some Brønsted Acids. Tartu, 2009, 103 p.
90. **Eerold Vellemäe.** Applications of mischmetal in organic synthesis. Tartu, 2009, 93 p.
91. **Sven Parkel.** Ligand binding to 5-HT_{1A} receptors and its regulation by Mg^{2+} and Mn^{2+}. Tartu, 2010, 99 p.
92. **Signe Vahur.** Expanding the possibilities of ATR-FT-IR spectroscopy in determination of inorganic pigments. Tartu, 2010, 184 p.
93. **Tavo Romann**. Preparation and surface modification of bismuth thin film, porous, and microelectrodes. Tartu, 2010, 155 p.
94. **Nadežda Aleksejeva.** Electrocatalytic reduction of oxygen on carbon nanotube-based nanocomposite materials. Tartu, 2010, 147 p.
95. **Marko Kullapere.** Electrochemical properties of glassy carbon, nickel and gold electrodes modified with aryl groups. Tartu, 2010, 233 p.
96. **Liis Siinor.** Adsorption kinetics of ions at Bi single crystal planes from aqueous electrolyte solutions and room-temperature ionic liquids. Tartu, 2010, 101 p.
97. **Angela Vaasa.** Development of fluorescence-based kinetic and binding assays for characterization of protein kinases and their inhibitors. Tartu 2010, 101 p.
98. **Indrek Tulp.** Multivariate analysis of chemical and biological properties. Tartu 2010, 105 p.
99. **Aare Selberg.** Evaluation of environmental quality in Northern Estonia by the analysis of leachate. Tartu 2010, 117 p.
100. **Darja Lavõgina.** Development of protein kinase inhibitors based on adenosine analogue-oligoarginine conjugates. Tartu 2010, 248 p.
101. **Laura Herm.** Biochemistry of dopamine D_2 receptors and its association with motivated behaviour. Tartu 2010, 156 p.

102. **Terje Raudsepp.** Influence of dopant anions on the electrochemical properties of polypyrrole films. Tartu 2010, 112 p.
103. **Margus Marandi.** Electroformation of Polypyrrole Films: *In-situ* AFM and STM Study. Tartu 2011, 116 p.
104. **Kairi Kivirand.** Diamine oxidase-based biosensors: construction and working principles. Tartu, 2011, 140 p.
105. **Anneli Kruve.** Matrix effects in liquid-chromatography electrospray mass-spectrometry. Tartu, 2011, 156 p.
106. **Gary Urb.** Assessment of environmental impact of oil shale fly ash from PF and CFB combustion. Tartu, 2011, 108 p.
107. **Nikita Oskolkov.** A novel strategy for peptide-mediated cellular delivery and induction of endosomal escape. Tartu, 2011, 106 p.
108. **Dana Martin.** The QSPR/QSAR approach for the prediction of properties of fullerene derivatives. Tartu, 2011, 98 p.
109. **Säde Viirlaid.** Novel glutathione analogues and their antioxidant activity. Tartu, 2011, 106 p.
110. **Ülis Sõukand.** Simultaneous adsorption of Cd^{2+}, Ni^{2+}, and Pb^{2+} on peat. Tartu, 2011, 124 p.
111. **Lauri Lipping.** The acidity of strong and superstrong Brønsted acids, an outreach for the "limits of growth": a quantum chemical study. Tartu, 2011, 124 p.
112. **Heisi Kurig.** Electrical double-layer capacitors based on ionic liquids as electrolytes. Tartu, 2011, 146 p.
113. **Marje Kasari.** Bisubstrate luminescent probes, optical sensors and affinity adsorbents for measurement of active protein kinases in biological samples. Tartu, 2012, 126 p.
114. **Kalev Takkis.** Virtual screening of chemical databases for bioactive molecules. Tartu, 2012, 122 p.
115. **Ksenija Kisseljova**. Synthesis of aza-β^3-amino acid containing peptides and kinetic study of their phosphorylation by protein kinase A. Tartu, 2012, 104 p.
116. **Riin Rebane.** Advanced method development strategy for derivatization LC/ESI/MS. Tartu, 2012, 184 p.
117. **Vladislav Ivaništšev.** Double layer structure and adsorption kinetics of ions at metal electrodes in room temperature ionic liquids. Tartu, 2012, 128 p.
118. **Irja Helm.** High accuracy gravimetric Winkler method for determination of dissolved oxygen. Tartu, 2012, 139 p.
119. **Karin Kipper.** Fluoroalcohols as Components of LC-ESI-MS Eluents: Usage and Applications. Tartu, 2012, 164 p.
120. **Arno Ratas.** Energy storage and transfer in dosimetric luminescent materials. Tartu, 2012, 163 p.
121. **Reet Reinart-Okugbeni**. Assay systems for characterisation of subtype-selective binding and functional activity of ligands on dopamine receptors. Tartu, 2012, 159 p.

122. **Lauri Sikk.** Computational study of the Sonogashira cross-coupling reaction. Tartu, 2012, 81 p.
123. **Karita Raudkivi.** Neurochemical studies on inter-individual differences in affect-related behaviour of the laboratory rat. Tartu, 2012, 161 p.
124. **Indrek Saar.** Design of GalR2 subtype specific ligands: their role in depression-like behavior and feeding regulation. Tartu, 2013, 126 p.
125. **Ann Laheäär.** Electrochemical characterization of alkali metal salt based non-aqueous electrolytes for supercapacitors. Tartu, 2013, 127 p.
126. **Kerli Tõnurist.** Influence of electrospun separator materials properties on electrochemical performance of electrical double-layer capacitors. Tartu, 2013, 147 p.
127. **Kaija Põhako-Esko.** Novel organic and inorganic ionogels: preparation and characterization. Tartu, 2013, 124 p.
128. **Ivar Kruusenberg.** Electroreduction of oxygen on carbon nanomaterial-based catalysts. Tartu, 2013, 191 p.
129. **Sander Piiskop.** Kinetic effects of ultrasound in aqueous acetonitrile solutions. Tartu, 2013, 95 p.
130. **Ilona Faustova**. Regulatory role of L-type pyruvate kinase N-terminal domain. Tartu, 2013, 109 p.
131. **Kadi Tamm.** Synthesis and characterization of the micro-mesoporous anode materials and testing of the medium temperature solid oxide fuel cell single cells. Tartu, 2013, 138 p.
132. **Iva Bozhidarova Stoyanova-Slavova.** Validation of QSAR/QSPR for regulatory purposes. Tartu, 2013, 109 p.
133. **Vitali Grozovski**. Adsorption of organic molecules at single crystal electrodes studied by *in situ* STM method. Tartu, 2014, 146 p.
134. **Santa Veikšina**. Development of assay systems for characterisation of ligand binding properties to melanocortin 4 receptors. Tartu, 2014, 151 p.
135. **Jüri Liiv.** PVDF (polyvinylidene difluoride) as material for active element of twisting-ball displays. Tartu, 2014, 111 p.
136. **Kersti Vaarmets.** Electrochemical and physical characterization of pristine and activated molybdenum carbide-derived carbon electrodes for the oxygen electroreduction reaction. Tartu, 2014, 131 p.
137. **Lauri Tõntson**. Regulation of G-protein subtypes by receptors, guanine nucleotides and Mn^{2+}. Tartu, 2014, 105 p.
138. **Aiko Adamson.** Properties of amine-boranes and phosphorus analogues in the gas phase. Tartu, 2014, 78 p.
139. **Elo Kibena**. Electrochemical grafting of glassy carbon, gold, highly oriented pyrolytic graphite and chemical vapour deposition-grown graphene electrodes by diazonium reduction method. Tartu, 2014, 184 p.
140. **Teemu Näykki.** Novel Tools for Water Quality Monitoring – From Field to Laboratory. Tartu, 2014, 202 p.
141. **Karl Kaupmees.** Acidity and basicity in non-aqueous media: importance of solvent properties and purity. Tartu, 2014, 128 p.

142. **Oleg Lebedev**. Hydrazine polyanions: different strategies in the synthesis of heterocycles. Tartu, 2015, 118 p.
143. **Geven Piir.** Environmental risk assessment of chemicals using QSAR methods. Tartu, 2015, 123 p.
144. **Olga Mazina.** Development and application of the biosensor assay for measurements of cyclic adenosine monophosphate in studies of G protein-coupled receptor signalinga. Tartu, 2015, 116 p.
145. **Sandip Ashokrao Kadam.** Anion receptors: synthesis and accurate binding measurements. Tartu, 2015, 116 p.
146. **Indrek Tallo.** Synthesis and characterization of new micro-mesoporous carbide derived carbon materials for high energy and power density electrical double layer capacitors. Tartu, 2015, 148 p.
147. **Heiki Erikson.** Electrochemical reduction of oxygen on nanostructured palladium and gold catalysts. Tartu, 2015, 204 p.
148. **Erik Anderson.** *In situ* Scanning Tunnelling Microscopy studies of the interfacial structure between Bi(111) electrode and a room temperature ionic liquid. Tartu, 2015, 118 p.
149. **Girinath G. Pillai.** Computational Modelling of Diverse Chemical, Biochemical and Biomedical Properties. Tartu, 2015, 140 p.
150. **Piret Pikma.** Interfacial structure and adsorption of organic compounds at Cd(0001) and Sb(111) electrodes from ionic liquid and aqueous electrolytes: an *in situ* STM study. Tartu, 2015, 126 p.
151. **Ganesh babu Manoharan.** Combining chemical and genetic approaches for photoluminescence assays of protein kinases. Tartu, 2016, 126 p.
152. **Carolin Siimenson**. Electrochemical characterization of halide ion adsorption from liquid mixtures at Bi(111) and pyrolytic graphite electrode surface. Tartu, 2016, 110 p.
153. **Asko Laaniste.** Comparison and optimisation of novel mass spectrometry ionisation sources. Tartu, 2016, 156 p.
154. **Hanno Evard.** Estimating limit of detection for mass spectrometric analysis methods. Tartu, 2016, 224 p.
155. **Kadri Ligi.** Characterization and application of protein kinase-responsive organic probes with triplet-singlet energy transfer. Tartu, 2016, 122 p.
156. **Margarita Kagan.** Biosensing penicillins' residues in milk flows. Tartu, 2016, 130 p.
157. **Marie Kriisa.** Development of protein kinase-responsive photoluminescent probes and cellular regulators of protein phosphorylation. Tartu, 2016, 106 p.
158. **Mihkel Vestli.** Ultrasonic spray pyrolysis deposited electrolyte layers for intermediate temperature solid oxide fuel cells. Tartu, 2016, 156 p.
159. **Silver Sepp**. Influence of porosity of the carbide-derived carbon on the properties of the composite electrocatalysts and characteristics of polymer electrolyte fuel cells. Tartu, 2016, 137 p.
160. **Kristjan Haav**. Quantitative relative equilibrium constant measurements in supramolecular chemistry. Tartu, 2017, 158 p.

161. **Anu Teearu**. Development of MALDI-FT-ICR-MS methodology for the analysis of resinous materials. Tartu, 2017, 205 p.
162. **Taavi Ivan**. Bifunctional inhibitors and photoluminescent probes for studies on protein complexes. Tartu, 2017, 140 p.
163. **Maarja-Liisa Oldekop**. Characterization of amino acid derivatization reagents for LC-MS analysis. Tartu, 2017, 147 p.
164. **Kristel Jukk**. Electrochemical reduction of oxygen on platinum- and palladium-based nanocatalysts. Tartu, 2017, 250 p.
165. **Siim Kukk**. Kinetic aspects of interaction between dopamine transporter and *N*-substituted nortropane derivatives. Tartu, 2017, 107 p.
166. **Birgit Viira**. Design and modelling in early drug development in targeting HIV-1 reverse transcriptase and Malaria. Tartu, 2017, 172 p.
167. **Rait Kivi**. Allostery in cAMP dependent protein kinase catalytic subunit. Tartu, 2017, 115 p.
168. **Agnes Heering**. Experimental realization and applications of the unified acidity scale. Tartu, 2017, 123 p.
169. **Delia Juronen**. Biosensing system for the rapid multiplex detection of mastitis-causing pathogens in milk. Tartu, 2018, 85 p.
170. **Hedi Rahnel.** ARC-inhibitors: from reliable biochemical assays to regulators of physiology of cells. Tartu, 2018, 176 p.
171. **Anton Ruzanov.** Computational investigation of the electrical double layer at metal–aqueous solution and metal–ionic liquid interfaces. Tartu, 2018, 129 p.
172. **Katrin Kestav.** Crystal Structure-Guided Development of Bisubstrate-Analogue Inhibitors of Mitotic Protein Kinase Haspin. Tartu, 2018, 166 p.
173. **Mihkel Ilisson.** Synthesis of novel heterocyclic hydrazine derivatives and their conjugates. Tartu, 2018, 101 p.
174. **Anni Allikalt.** Development of assay systems for studying ligand binding to dopamine receptors. Tartu, 2018, 160 p.
175. **Ove Oll.** Electrical double layer structure and energy storage characteristics of ionic liquid based capacitors. Tartu, 2018, 187 p.
176. **Rasmus Palm.** Carbon materials for energy storage applications. Tartu, 2018, 114 p.
177. **Jörgen Metsik.** Preparation and stability of poly(3,4-ethylenedioxythiophene) thin films for transparent electrode applications. Tartu, 2018, 111 p.
178. **Sofja Tšepelevitš.** Experimental studies and modeling of solute-solvent interactions. Tartu, 2018, 109 p.
179. **Märt Lõkov.** Basicity of some nitrogen, phosphorus and carbon bases in acetonitrile. Tartu, 2018, 104 p.
180. **Anton Mastitski**. Preparation of α-aza-amino acid precursors and related compounds by novel methods of reductive one-pot alkylation and direct alkylation. Tartu, 2018, 155 p.
181. **Jürgen Vahter**. Development of bisubstrate inhibitors for protein kinase CK2. Tartu, 2019, 186 p.

182. **Piia Liigand.** Expanding and improving methodology and applications of ionization efficiency measurements. Tartu, 2019, 189 p.
183. **Sigrid Selberg.** Synthesis and properties of lipophilic phosphazene-based indicator molecules. Tartu, 2019, 74 p.
184. **Jaanus Liigand.** Standard substance free quantification for LC/ESI/MS analysis based on the predicted ionization efficiencies. Tartu, 2019, 254 p.
185. **Marek Mooste.** Surface and electrochemical characterisation of aryl film and nanocomposite material modified carbon and metal-based electrodes. Tartu, 2019, 304 p.
186. **Mare Oja.** Experimental investigation and modelling of pH profiles for effective membrane permeability of drug substances. Tartu, 2019, 306 p.
187. **Sajid Hussain.** Electrochemical reduction of oxygen on supported Pt catalysts. Tartu, 2019, 220 p.
188. **Ronald Väli.** Glucose-derived hard carbon electrode materials for sodium-ion batteries. Tartu, 2019, 180 p.
189. **Ester Tee.** Analysis and development of selective synthesis methods of hierarchical micro- and mesoporous carbons. Tartu, 2019, 210 p.
190. **Martin Maide.** Influence of the microstructure and chemical composition of the fuel electrode on the electrochemical performance of reversible solid oxide fuel cell. Tartu, 2020, 144 p.
191. **Edith Viirlaid.** Biosensing Pesticides in Water Samples. Tartu, 2020, 102 p.
192. **Maike Käärik.** Nanoporous carbon: the controlled nanostructure, and structure-property relationships. Tartu, 2020, 162 p.
193. **Artur Gornischeff.** Study of ionization efficiencies for derivatized compounds in LC/ESI/MS and their application for targeted analysis. Tartu, 2020, 124 p.
194. **Reet Link.** Ligand binding, allosteric modulation and constitutive activity of melanocortin-4 receptors. Tartu, 2020, 108 p.
195. **Pilleriin Peets.** Development of instrumental methods for the analysis of textile fibres and dyes. Tartu, 2020, 150 p.
196. **Larisa Ivanova.** Design of active compounds against neurodegenerative diseases. Tartu, 2020, 152 p.
197. **Meelis Härmas.** Impact of activated carbon microstructure and porosity on electrochemical performance of electrical double-layer capacitors. Tartu, 2020, 122 p.
198. **Ruta Hecht.** Novel Eluent Additives for LC-MS Based Bioanalytical Methods. Tartu, 2020, 202 p.
199. **Max Hecht.** Advances in the Development of a Point-of-Care Mass Spectrometer Test. Tartu, 2020, 168 p.
200. **Ida Rahu.** Bromine formation in inorganic bromide/nitrate mixtures and its application for oxidative aromatic bromination. Tartu, 2020, 116 p.
201. **Sander Ratso**. Electrocatalysis of oxygen reduction on non-precious metal catalysts. Tartu, 2020, 371 p.
202. **Astrid Darnell.** Computational design of anion receptors and evaluation of host-guest binding. Tartu, 2021, 150 p.

203. **Ove Korjus.** The development of ceramic fuel electrode for solid oxide cells. Tartu, 2021, 150 p.
204. **Merit Oss.** Ionization efficiency in electrospray ionization source and its relations to compounds' physico-chemical properties. Tartu, 2021, 124 p.
205. **Madis Lüsi**. Electroreduction of oxygen on nanostructured palladium catalysts. Tartu, 2021, 180 p.
206. **Eliise Tammekivi.** Derivatization and quantitative gas-chromatographic analysis of oils. Tartu, 2021, 122 p.
207. **Simona Selberg.** Development of Small-Molecule Regulators of Epi-transcriptomic Processes. Tartu, 2021, 122 p.
208. **Olivier Etebe Nonga.** Inhibitors and photoluminescent probes for in vitro studies on protein kinases PKA and PIM. Tartu, 2021, 189 p.
209. **Riinu Härmas.** The structure and H2 diffusion in porous carbide-derived carbon particles. Tartu, 2022, 123 p.
210. **Maarja Paalo.** Synthesis and characterization of novel carbon electrodes for high power density electrochemical capacitors. Tartu, 2022, 144 p.
211. **Jinfeng Zhao.** Electrochemical characteristics of Bi(hkl) and micro-meso-porous carbon electrodes in ionic liquid based electrolytes. Tartu, 2022, 134 p.
212. **Alar Heinsaar.** Investigation of oxygen electrode materials for high-temperature solid oxide cells in natural conditions. Tartu, 2022, 120 p.
213. **Jaana Lilloja.** Transition metal and nitrogen doped nanocarbon cathode catalysts for anion exchange membrane fuel cells. Tartu, 2022, 202 p.
214. **Maris-Johanna Tahk.** Novel fluorescence-based methods for illuminating transmembrane signal transduction by G-protein coupled receptors. Tartu, 2022, 200 p.
215. **Eerik Jõgi.** Development and Applications of E. coli Immunosensor. Tartu, 2022, 103 p.
216. **Alo Rüütel.** Design principles of synthetic molecular receptors for anion-selective electrodes. Tartu, 2022, 109 p.
217. **Tanel Sõrmus.** Development of stimuli-responsive and covalent bisubstrate inhibitors of protein kinases. Tartu, 2022, 148 p.
218. **Oleg Artemchuk.** Autotrophic nitrogen removal processes for nutrient removal from sidestream and mainstream wastewater. Tartu, 2022, 115 p.
219. **Andre Leesment.** Quantitative studies of Brønsted acidity in biphasic systems and gas-phase. Tartu, 2023, 83 p.
220. **Meeli Arujõe-Sado.** Structural effects in aza-peptide bond formation reaction. Tartu, 2023, 83 p.
221. **Jonas Mart Linge.** Electrochemical reduction of oxygen on silver-based catalysts. Tartu, 2023, 269 p.
222. **Tõnis Laasfeld.** Integrating Image Analysis and Quantitative Modeling for a Holistic View of GPCR Ligand Binding Dynamics. Tartu, 2023, 226 p.
223. **Ernesto de Jesus Zapata Flores.** Derivatization Reagents used in negative mode electrospray LC-MS. Tartu, 2023, 107 p.

224. **Patrick Teppor.** Obtaining platinum-free oxygen reduction catalysts through biomass valorization: a case study of peat. Tartu, 2023, 161 p.
225. **Peeter Valk.** Methanol Oxidation on Platinum-Rare-Earth Metal Oxide Activated Catalysts. Tartu, 2023, 162 p.
226. **Shidong Chen.** Unravelling prehistoric plant exploitation in eastern Baltic: organic residue analysis of plant-based materials by multi-method approach. Tartu, 2023, 245 p.
227. **Yogesh Kumar.** M-N_4 macrocycle-based catalysts for electrocatalysis of oxygen reduction and oxygen evolution. Tartu, 2023, 224 p.
228. **Kerli Martin.** Recognition of carboxylates by synthetic receptors – from structure-affinity studies to solid-contact anion-selective electrode prototyping. Tartu, 2024, 130 p.
229. **Huy Quí Vinh Nguyen.** Development of Carbon Supported Pt–CeO_2 Catalysts for Proton Exchange Membrane Fuel Cells. Tartu, 2024, 198 p.
230. **Heigo Ers**. Adsorption and Structuring Processes at Single Crystal Electrode – Ionic Liquid Interface – Insights from Simulations and *in situ* Studies. Tartu, 2024, 137 p.
231. **Ritums Cepitis.** Modelling Structural and Geometrical Effects in Carbon Dioxide and Oxygen Electrocatalysis. Tartu, 2024, 99 p.
232. **Kaarel Kisand.** Resorcinol-derived carbon-based catalysts for polymer electrolyte fuel cell cathodes. Tartu, 2024, 205 p.
233. **Akmal Kosimov**. Template-assisted Mechanosynthesis (TAMS) for the production of bifunctional transition metal-based catalysts. Tartu, 2024, 123 p.
234. **Larissa Silva Macieli.** Derivatization-targeted LC-MS analysis of compounds containing amino group. Tartu, 2024, 157 p.
235. **Silvester Jürjo.** Separation of rare earth elements from Estonian phosphorite ore using liquid extraction followed by electrochemical reduction. Tartu, 2024, 99 p.
236. **Jan-Michael C. Cayme.** Organic-inorganic interactions in experimental and archaeological ceramics. Tartu, 2025, 156 p.
237. **Miriam Koppel.** The diffusion of H2 adsorbed in carbide-derived carbons: a quasi-elastic neutron scattering study. Tartu, 2025, 138 p.
238. **Kenneth Tuul.** Evaluating lithium-ion pouch cells and hydrogen storage materials under extreme conditions using advanced techniques. Tartu, 2025, 188 p.
239. **Marta-Lisette Pikma.** Exploring the basicity of phosphanes and related compounds. Tartu, 2025, 100 p.
240. **Indrek Saar.** Development of novel on-site chemical analysis tests – from alternative materials and technologies to functional prototypes. Tartu, 2025, 214 p.
241. **Gulnara Yusibova.** TAL MOF-Derived M-N-C Electrocatalysts for Oxygen Reduction and Evolution Reactions. Tartu, 2025, 120 p.

242. **Karl Marti Toots.** Cheminformatics Approaches for Analyzing and Modeling the Gas-Ionic Liquid Distribution of Organic Solutes. Tartu, 2025, 249 p.
243. **Freddy Kukk.** Electrochemical Characterization of Structurally and Chemically Modified Solid Oxide Cells Operated in Electrolysis Mode. Tartu, 2026, 142 p.
244. **Shrikant Shivaji Pawade.** Metrological Aspects of Sampling and Water/ Moisture Determination on the Example of Lignin. Tartu, 2026, 146 p.